Collisional Processes involving Icy Bodies in the Solar System

Thesis by

Sarah T. Stewart

In Partial Fulfillment of the Requirements

for the Degree of

Doctor of Philosophy

California Institute of Technology

Pasadena, California

2002

(Defended December 6, 2001)

Acknowledgements

I am grateful for the wisdom and guidance of my advisor, Tom Ahrens, who gave me remarkable freedom in his lab and invaluable career and life advice. I also thank Professors George Rossman, Mike Brown, Bruce Murray, Shri Kulkarni, Andy Ingersoll, Dave Stevenson and Peter Goldreich for their teaching, support, and direction during my graduate residence.

My experiments would not have been possible without the assistance of many people, including Mike Long and Papo Gelle, who make working in the lab truly enjoyable, and Vic Nenow, Carl McCaughey, Jose Nunez-Anzueto and Stan Cincera, who were always willing to put in a little extra time to help me. In particular, I thank Barclay Kamb for the generous use of his cold lab, and Hermann Engelhardt and Robin Bolsey for their help and accommodation.

The department's staff support is outstanding, and my work was made easier by the talents of Sue Yamada, Mike Black, Ken Ou, and Kimo Yap. I also thank Kimo for the bridge games, and Sue and Stan Yamada for their excellent cooking on group retreats.

I am thankful for the many great field trips possible in GPS. I'm grateful for George Rossman and Jason Saleeby's flexibility in the planning and execution of the Meteor Crater trip. I thank Mike Scott, for his generous sponsorship, and Kerry Sieh, for his great leadership, of the Division trip to Greece and Turkey. Jason Saleeby, Lee Silver, and John Eiler led an excellent (and memorable) 2001 Pahoehoe trip.

I owe a great deal to those who helped me in my post-graduate plans, especially Ed Stolper, Bruce Murray, Arden Albee, Andy Ingersoll, Gerry Wasserburg, and Tom Ahrens, and to those who supported (or suffered) me through my temporary job search obsession.

I thank the many friends I made in the department, who made graduate student life fun and, well, a life. I especially thank the reading group crowd: Emily Brodsky, Francis Nimmo, Magali Billen, Lesley Perg, Derrick Bass, Theresa Lynn, Jon Moore, Edwin Schauble, Liz Johnson, and Matt Pritchard.

I am thankful for the support of my parents and the exciting distractions caused by my brother. Finally, I thank my husband, Sujoy Mukhopadhyay, for everything, and I dedicate this thesis to him.

Abstract

1. The Shock Hugoniot of Solid Ice

We present a complete description of the solid ice Hugoniot based on new shock wave experiments conducted at an initial temperature of 100 K and previously published data obtained at 263 K. We identify five regions on the solid ice Hugoniot: (1) elastic shock waves, (2) ice Ih deformation shocks, transformation shocks to (3) ice VI, (4) ice VII, and (5) liquid water. In each region, data obtained at different initial temperatures are described by a single $U_S - \Delta u_p$ shock equation of state. The dynamic strength of ice Ih is strongly dependent on temperature. The Hugoniot Elastic Limit varies from 0.05 to 0.62 GPa, as a function of temperature and peak shock stress. We estimate the entropy and temperature along the 100 and 263 K Hugoniots and derive the critical pressures for shock-induced incipient (IM) and complete (CM) melting upon release. On the 100 K Hugoniot, the critical pressures are about 4.5 and between 5-6 GPa for IM and CM, respectively. On the 263 K Hugoniot, the critical pressures are 0.6 and 3.7 GPa for IM and CM, lower than previously suggested. Shock-induced melting of ice will be widespread in impact events.

2. Rampart Crater Formation on Mars

We present a model for the fluidization of Martian rampart crater ejecta blankets with liquid water based on the shock physics of cratering onto an ice-rich regolith. We conducted simulations of crater formation on Mars, explicitly accounting for the equations of state and shock-induced melting criteria for both the silicate and ice components and using strength models constrained by the observed transition diameter D_{Tr} from simple to complex craters on Mars, where $D_{Tr} = 8$ km corresponds to an effective yield strength of 10^7 Pa.

For the observed size range of rampart craters (diameters $D \lesssim 30$ km) and typical asteroidal impact conditions (silicate impactors, $D \lesssim 1$ km, at 10 km s^{-1}), we find that the hemispherical volume where subsurface ice is partially melted by the impact shock has a radius of about 15 projectile radii (r_p), much larger than previous predictions of about 6 r_p. The radius of the final crater is comparable to the radius of partial melting and more than half the ice within the excavated material is melted. Thus, the amount of shock-melted water incorporated into the continuous ejecta blanket is within a factor of two of the near-surface ground ice content.

We find that fluidized ejecta blankets may form in the current climate with mean surface temperatures of 200 K. Decreasing the effective yield strength of the modeled materials, e.g., by increasing the ice content or porosity, modifies the impact-induced flow in the excavated cavity, resulting in deeper projectile penetration, steeper ejection angles, higher crater rim uplift, and reduced final crater diameter. The volume fraction of shock-melted water in the ejecta blanket increases with distance from the crater rim. The horizontal flow velocities during emplacement of fluidized ejecta ($\sim 10 - 1000$ m s^{-1}) is nearly constant in the continuous ejecta blanket and within the range of large terrestrial landslides. Therefore, ground-hugging debris flow conditions are achieved. The ejecta blanket properties from impacts into a Martian regolith containing 20-40$\%_{vol}$ near-surface ice are consistent with the fraction of liquid water inferred from models of ejecta flow rheologies which produce rampart morphologies, about 10-30% liquid water by volume [Ivanov, B. A., *Solar System Research, 30*, 43-58, 1996].

We present a model for the formation of different rampart ejecta morphologies which may be used in conjunction with an ejecta blanket debris flow model to map the distribution of ground ice. In addition, we find that formation of single or multiple-rampart ejecta blankets does not require pre-existing liquid water in the Martian crust. We estimate the minimum water content in observed rampart ejecta blankets to be equivalent to a global layer of water 0.6 m thick. Based on the crater sampling efficiency, the implied global Martian ice content, within the upper 2 km of the crust, is equivalent to a global layer of water 100 m deep. This result is comparable to other estimates of H_2O content in the Martian crust.

Contents

Acknowledgements iii

Abstract iv

List of Tables viii

List of Figures ix

1 Introduction 1

Bibliography 5

2 The Solid Ice Hugoniot: Temperature-dependent Strength and Shock-induced Phase Transformations 7

2.1 Introduction 7

2.2 Experimental Procedures and Data Analysis 9

2.2.1 Target Assembly 11

2.2.2 Lagrangian Data Analysis 12

2.3 Results and Interpretation 24

2.3.1 The $U_S - \Delta u_p$ Shock Equation of State 24

2.3.2 The $P - V$ Hugoniot 28

2.4 Regions on the Solid Ice Hugoniot 31

2.4.1 Elastic Shock Precursors 31

2.4.2 Ice Ih Shocks 38

2.4.3 Ice VI 42

2.4.4 Ice VII 48

2.4.5 Liquid Water 50

2.5 Shock Temperatures 51

2.6 Release from Shock 53

2.7 Discussion 57

2.7.1 Impact-induced Melting of Ice on Planetary Surfaces 57

2.7.2 Formation of Metastable High-pressure Ice Polymorphs from Impact Events . . . 58
2.8 Conclusions . . . 59
Bibliography . . . 61

3 Rampart Crater Formation on Mars **66**
3.1 Introduction . . . 66
3.2 Simulations of Crater Formation on Mars . . . 68
3.3 Fluidization of Ejected Material . . . 75
3.3.1 Shock Melting of Subsurface Ice . . . 75
3.3.2 Projectile-crater Size Scaling . . . 79
3.4 Excavation and Rim Uplift . . . 87
3.5 Ejecta Properties and Topography . . . 95
3.6 Discussion . . . 103
3.6.1 Interpretation of Rampart Crater Morphologies . . . 103
3.6.2 Implications for the H_2O Budget on Mars . . . 110
3.7 Conclusions . . . 114
3.8 Acknowledgements . . . 115
Bibliography . . . 116

Appendix A: Details of Shock-Wave Experiments in Ice **121**

List of Tables

2.1 Summary of solid ice shock data. 9
2.2 Average Final Hugoniot States 20
2.3 New Ice Hugoniot Data 22
2.4 $U_S - \Delta u_p$ shock equation of state 27
2.5 Triple points of the stable phases of H_2O. 45
2.6 Selected properties of stable ice phases. 46

3.1 Strength models in Mars impact simulations. 74
3.2 Critical shock pressures for phase change on release. 75
3.3 Shock profile decay exponents. 77

List of Figures

1.1 H_2O phase diagram 2

2.1 H_2O phase diagram 8
2.2 Schematic of experimental procedures 17
2.3 Magnetic field map 17
2.4 Lagrangian analysis method 18
2.5 Hugoniot state averaging of Lagrangian analysis 19
2.6 Shock loading paths 21
2.7 Comparison between shock data at $T_0 = 100$ and 263 K 25
2.8 $U_S - \Delta u_p$ relations on the solid ice Hugoniot 26
2.9 Solid ice Hugoniots centered at $T_0 = 100$ and 263 K 29
2.10 Properties of elastic shock precursor waves 32
2.11 Elastic shock stress-temperature amplitude model 34
2.12 Elastic shock precursor amplitudes and $P - T$ phase diagram 36
2.13 Elastic precursor data and isothermal compression curves 37
2.14 Ice Ih region on the 100 K solid ice Hugoniot 40
2.15 Ice Hugoniots on pressure-entropy phase diagram 43
2.16 Ice VI region of solid ice Hugoniot 44
2.17 Ice VII region of solid ice Hugoniot 49
2.18 Liquid water region of solid ice Hugoniot 51
2.19 Ice $P - T$ phase diagram with shock Hugoniots 52
2.20 Shock release $P - V$ paths 54
2.21 Release wave velocities 56

3.1 Simulation mesh and tracer particle distribution 69
3.2 ANEOS H_2O and dunite Hugoniots 71
3.3 Shock pressure decay profiles 76
3.4 Crater excavation zones: strength effects 80
3.5 Crater excavation zones: ice effects 81
3.6 Crater excavation zones: 1PT vs. MMT 83

3.7 Crater excavation zones: MMP2 vs. MMT 84
3.8 Crater diameter scaling 85
3.9 Crater excavation zones: Y_{std} vs. Y_{weak} 88
3.10 Excavation streamtubes 90
3.11 Ejection velocities and angles 92
3.12 Rim uplift 94
3.13 Complex crater collapse 96
3.14 2.5 and 5 km diameter crater excavation model 99
3.15 10 and 20 km diameter crater excavation model: gravity scaling 100
3.16 10 and 20 km diameter crater excavation model: strength scaling 101
3.17 Ejecta model and MOLA comparison: $D_F = 9$ km 102
3.18 Ejecta model and MOLA comparison: $D_F = 20$ km 103
3.19 Formation models for rampart ejecta morphologies 105
3.20 Inferred crustal water content 112
A.1 Shot I44: Data record 122
A.2 Shot I44: Loading path 122
A.3 Shot I45: Data record 123
A.4 Shot I45: Loading path 123
A.5 Shot 1046: Data record 124
A.6 Shot 1046: Loading path 124
A.7 Shot 1047: Data record 125
A.8 Shot 1047: Loading path 125
A.9 Shot 1043: Data record 126
A.10 Shot 1043: Loading path 126
A.11 Shot 1045: Data record 127
A.12 Shot 1045: Loading path 127

Chapter 1 Introduction

Impact events are an ubiquitous surface modification and evolutionary process in the solar system. The ages of planetary surfaces are frequently inferred from the crater density, as collisions occur over a wide range of planetary scales throughout the history of the solar system. The physics of impact cratering is studied to determine the dependence of crater dimensions on impactor properties and velocity, and to quantify the occurrence and amount of impact-induced metamorphism, melting and vaporization.

Knowledge of the material properties of the constituent materials is necessary to predict the outcome of individual impact events, such as cratering vs. catastrophic disruption, and the history of collisionally evolved systems, including the asteroid and Kuiper belts. H_2O, in particular, is of fundamental importance in the study of collisions, as ice is a major rock-forming mineral in the outer solar system, water covers most of the Earth's surface, and the history of H_2O on Mars may be illuminated by impact events.

Although there have been several studies measuring the shock properties of H_2O ice, interpretation of the data has been difficult [*Gaffney*, 1985]. The presence of different shock-induced phase changes to high-pressure ice polymorphs and liquid water has been inferred, but the details of the conditions under which a particular phase is created have not been explained. Complicating the data analysis, different studies show inconsistent results, in part because of experimental difficulties in accurately measuring shocks in ice, but also because a consistent framework for comparison between datasets had not been developed. In addition, previous work has focused on impacts under terrestrial conditions, and inspection of the H_2O phase diagram, Figure 1.1, emphasizes the need for shock data at a range of initial temperatures.

As a general theory for the response of ice subject to a shock has remained elusive, much of the previous work on collisional processes in ice has focused on experimental derivation of empirical relationships. In particular, there have been exploratory studies of impact crater size scaling relationships [*Lange and Ahrens*, 1987; *Iijima et al.*, 1995; *Kato et al.*, 1995], the velocity and size distribution of ejected or catastrophically fragmented material [e.g., *Lange and Ahrens*, 1981; *Arakawa et al.*, 1995], and the dynamic strength of solid ice [*Lange and Ahrens*, 1983; *Stewart and Ahrens*, 1999; *Arakawa et al.*, 2000]. Scaling the laboratory

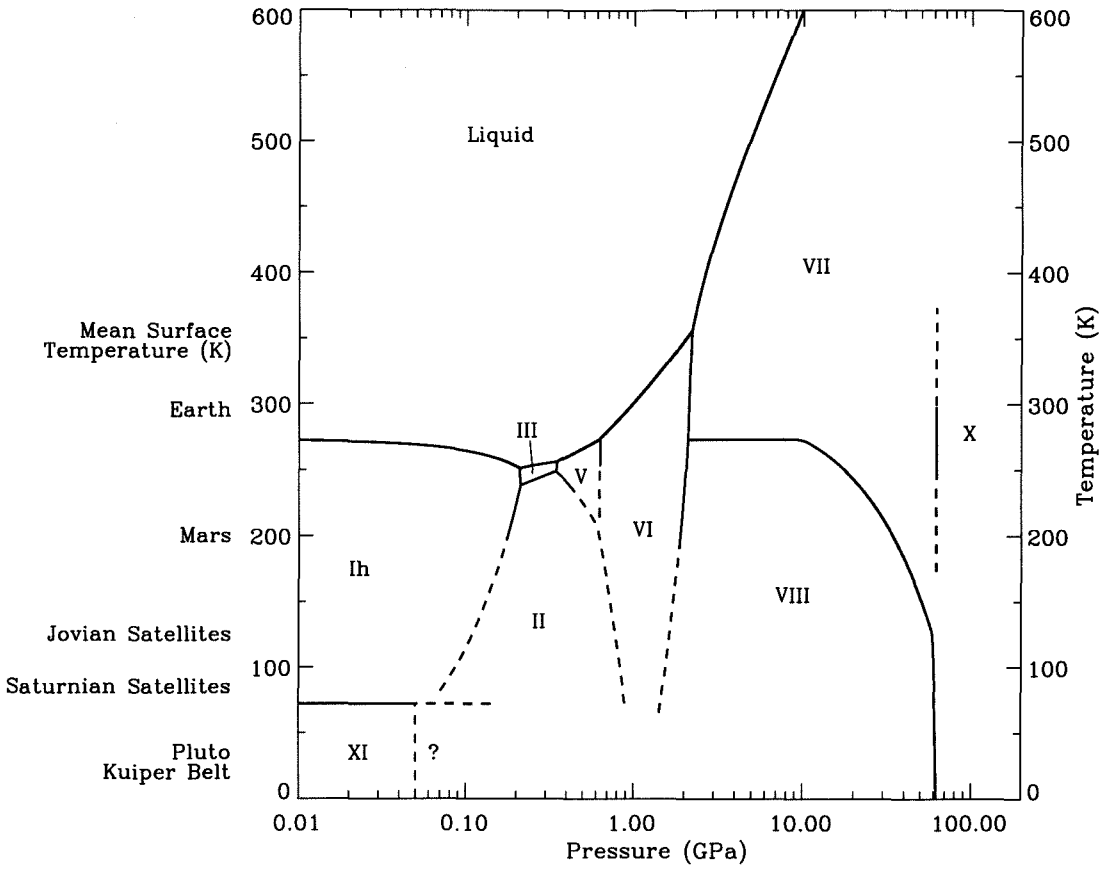

Figure 1.1: H_2O phase diagram showing stable phases with logarithmic pressure axis. Mean surface temperatures of solar system objects are noted. Previous ice shock data at $T_0 = 263$ K are only applicable to Earth conditions. Phase diagram constructed from *Sotin et al.* [1998], *Petrenko and Whitworth* [1999], and *Dorsey* [1940], with extrapolated phase boundaries (dashed lines).

results to planetary-scale problems requires development of a general shock equation of state of ice.

Gaffney and Matson [1980], recognizing that high-pressure ice polymorphs formed under static conditions are recoverable at low pressure if maintained at low temperatures, suggested that ice polymorphs formed under shock processes may persist upon release to ambient conditions in the outer solar system. They hypothesized that the icy surfaces of outer solar system satellites might be a mixture of ice Ih and high-pressure polymorphs. The likelihood of this hypothesis has not been readdressed.

Furthermore, many of the implications of shock-induced phase changes on planetary surfaces and collisionally evolved bodies, such as cometesimals in the Kuiper belt, remain

to be explored. In particular, the amount of impact-induced melting may place important constraints on the physical properties of the surfaces of icy bodies in the solar system and comet nuclei. For example, *Turtle and Pierazzo* [2001] have used the amount of melt produced in an impact event to constrain the thickness of the brittle ice layer on Europa. From observations of the size range of Europan craters with central peaks and simulations of melt production during an impact onto a solid ice layer over a liquid water layer, they conclude that the solid ice layer must be more than 3-4 km thick.

In Chapter 2, we present the first study of the shock Hugoniot of ice at low temperatures, $\sim$ 100 K. In combination with the previous temperate data at about 263 K, we develop a general formulation of the solid ice Hugoniot, including the temperature-dependent response of ice Ih and the occurrence of shock-induced phase changes. The outcome of impact events is dependent on the details of release from the shocked state, and we determine the conditions under which high-pressure ice phases may remain metastable after an impact event.

We focus on the criteria for shock-induced melting of ice, where liquid water will be the thermodynamically favored state upon release from the shock. The production of shock melt is of interest in a wide range of collision phenomena, including the study of the bulk properties of planetary surfaces. In Chapter 3, we focus on the conditions under which shock-induced melting of ice may occur on Mars.

The presence of large quantities of water on Mars has been inferred from geomorphic features, most notably valley networks and catastrophic outflow channels [*Carr*, 1996]. In addition, many Martian impact craters are surrounded by ejecta blankets with the appearance of fluidized ground-hugging flow and terminated by one or more continuous ramparts [*Barlow and Bradley*, 1990]. The prevalent hypothesis for the formation of rampart ejecta morphologies is excavation and entrainment of subsurface ice or water into the ejecta blanket and subsequent long runout fluidized flow, forming a distal scarp when loss of fluidization occurs [*Carr et al.*, 1977; *Mouginis-Mark*, 1981; *Wohletz and Sheridan*, 1983]. While rampart craters have long held the promise of revealing information about the water content of the Martian regolith, the lack of a comprehensive physical model for the formation of fluidized ejecta has prevented quantifiable conclusions to be drawn about water on Mars. If ejecta fluidization can be related to ground ice, the occurrence and morphology of rampart ejecta could be used to map the distribution and amount of subsurface water, and rampart

craters would be a powerful probe of the history of H_2O on Mars.

Although several phenomenological models have been suggested to explain the formation of rampart ejecta features [e.g., *Mouginis-Mark*, 1981; *Barlow and Bradley*, 1990], no previous study has focused on a modeling effort to explain the ejecta fluidization by ground ice or water and the formation of different rampart morphologies. The shock properties of H_2O ice, detailed in Chapter 2, are now understood well enough to be explicitly considered in models of cratering under Martian conditions. We present simulations of impact events onto an ice-rich regolith, quantifying the differences in the excavation process compared to cratering on pure rock surfaces. From the simulation results and the criteria for shock-induced melting, we derive the physical properties of the ejected material. We present a model for the formation of different rampart crater morphologies and estimate the H_2O content of the Martian regolith.

Bibliography

Arakawa, M., N. Maeno, M. Higa, Y. Iijima, and M. Kato, Ejection velocity of ice impact fragments, *Icarus*, *118*, 341–354, 1995.

Arakawa, M., K. Shirai, and M. Kato, Shock wave and fracture propagation in water ice by high velocity impact, *Geophys. Res. Lett.*, *27*, 305–308, 2000.

Barlow, N. G., and T. L. Bradley, Martian impact craters: Correlations of the ejecta and interior morphologies with diameter, attitude, and terrain, *Icarus*, *87*, 156–179, 1990.

Carr, M. H., *Water on Mars*, Oxford UP, 1996.

Carr, M. H., L. S. Crumpler, J. A. Cutts, R. Greeley, J. E. Guest, and H. Masursky, Martian impact craters and emplacement of the ejecta by surface flow, *J. Geophys. Res.*, *82*, 4055–4065, 1977.

Dorsey, N. E. (Ed.), *Properties of Ordinary Water-Substance*, Reinhold Pub. Corp., New York, 1940.

Gaffney, E. S., Hugoniot of water ice, in *Ices in the Solar System*, edited by J. Klinger, D. Benest, A. Dollfus, and R. Smoluchowski, NATO ASI Series, pp. 119–148, D. Reidel, Nice, France, 1985.

Gaffney, E. S., and D. L. Matson, Water ice polymorphs and their significance on planetary surfaces, *Icarus*, *44*, 511–519, 1980.

Iijima, Y., M. Kato, M. Arakawa, N. Maeno, A. Fujimura, and H. Mizutani, Cratering experiments on ice - dependence of crater formation on projectile materials and scaling parameter, *Geophys. Res. Lett.*, *22*, 2005–2008, 1995.

Kato, M., Y. Iijima, M. Arakawa, Y. Okimura, A. Fujimura, N. Maeno, and H. Mizutani, Ice-on-ice impact experiments, *Icarus*, *113*, 423–441, 1995.

Lange, M. A., and T. J. Ahrens, Fragmentation of ice by low velocity impact, *Proc. Lunar Planet. Sci. Conf.*, *12B*, 1667–1687, 1981.

Lange, M. A., and T. J. Ahrens, The dynamic tensile strength of ice and ice-silicate mixtures, *J. Geophys. Res.*, *88*, 1197–1208, 1983.

Lange, M. A., and T. J. Ahrens, Impact experiments in low-temperature ice, *Icarus*, *69*, 506–518, 1987.

Mouginis-Mark, P., Ejecta emplacement and modes of formation of Martian fluidized ejecta

craters, *Icarus*, *45*, 60–76, 1981.

Petrenko, V. F., and R. W. Whitworth, *Physics of Ice*, chap. The Other Phases of Ice, pp. 253–286, Oxford University Press, New York, 1999.

Sotin, C., O. Grasset, and S. Beauchesne, Thermodynamic properties of high pressure ices: Implications for the dynamics and internal structure of large icy satellites, in *Solar System Ices*, edited by B. Schmitt, C. de Bergh, and M. Festou, vol. 227 of *Astrophysics and Space Science Library*, pp. 79–96, Kluwer Academic Publishers, 1998.

Stewart, S. T., and T. J. Ahrens, Correction to the dynamic tensile strength of ice and ice-silicate mixtures (Lange & Ahrens 1983), in *Proc. Lunar Planet. Sci. Conf.*, vol. 30, Abs. 2037, 1999.

Turtle, E. P., and E. Pierazzo, Thickness of a Europan ice shell from impact crater simulations, *Science*, *294*, 1326–1328, 2001.

Wohletz, K. H., and M. F. Sheridan, Martian rampart craters ejecta: Experiments and analysis of melt-water interaction, *Icarus*, *56*, 15–37, 1983.

Chapter 2 The Solid Ice Hugoniot: Temperature-dependent Strength and Shock-induced Phase Transformations

Sarah T. Stewart and Thomas J. Ahrens

2.1 Introduction

Knowledge of the dynamic properties of planetary materials is necessary to describe collisional processes in the solar system. The shock properties and dynamic strength of the constituent materials must be known to model and interpret mutual collisions and impact cratering phenomena. The outcome of such collisions are important for a wide range of planetary studies, including mass transfer from collisions (accretion, erosion, or catastrophic disruption), the relationship of crater dimensions to impactor properties and velocity, and the quantitative description of impact-metamorphism, melting and vaporization. This study of the dynamic properties of H_2O is motivated by its great abundance and importance.

Shock wave measurements yield information about the equation of state, the dynamic strength, and the existence and properties of high-pressure phases. H_2O has ten known stable phases, including liquid water, shown in Figure 2.1. Previous work on the shock properties of solid ice have focused on terrestrial applications, with limited scope investigations at initial temperatures just below freezing, Table 2.1.

Although the high-pressure region of the solid ice Hugoniot (> 8 GPa) has been well characterized, the solid-solid phase transformations, producing multiple shock wave structures, have been difficult to interpret [*Gaffney*, 1985]. Observations of shock-induced phase transformations under terrestrial conditions have also raised the question of the likelihood and significance of production of high-pressure ice polymorphs by impact processes [*Gaffney and Matson*, 1980]. Furthermore, the surface temperatures of Mars and the icy satellites in the outer solar system are well below the range of existing data, and inspection of the H_2O phase diagram emphasizes the crucial need for shock data for H_2O at lower temperatures.

We present the results from an experimental study of shock compression of solid H_2O at an initial temperature of 100 K. In combination with previously published shock and static data, we derive a complete shock Hugoniot for H_2O for initial temperatures ≥ 100 K. We

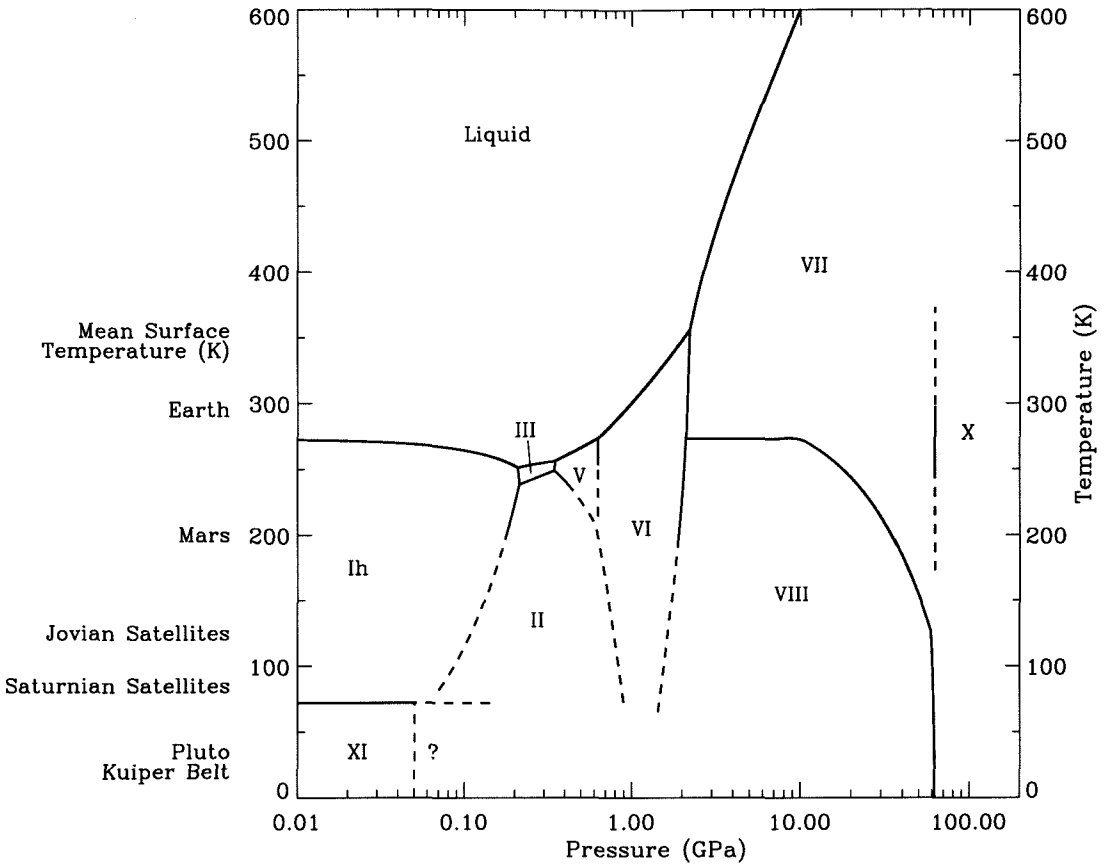

Figure 2.1: H_2O phase diagram showing stable phases with logarithmic pressure axis. Mean surface temperatures of solar system objects are noted. Previous ice shock data at $T_0 = 263$ K are only applicable to Earth conditions. Phase diagram constructed from *Sotin et al.* [1998], *Petrenko and Whitworth* [1999], and *Dorsey* [1940], with extrapolated phase boundaries (dashed lines).

investigate the dynamic strength, phase transformations, and shock temperatures on the Hugoniot. Finally, we discuss the implications of this work for impact cratering processes in the solar system, including the criteria for shock-induced melting of H_2O.

Table 2.1. Summary of solid ice shock data.

Symbol	Source	Stress/Pressure Range (GPa)⊛	Temp. (K)	No. Data Points Included*	Notes†
		Solid Ice Elastic Shock Waves			
■	this work	0.35 – 0.62	92-102	16	P
◊	*Larson* [1984]‡	0.15 – 0.30	263 ± 2	8	P
△	*Larson* [1984]‡	0.16 – 0.19	263 ± 2	5	S
▷	*Gaffney and Smith* [1994]	0.05 – 0.11	263-266	3	P
◁	*Davies and Smith* [1994]	0.05 – 0.23	263-266	1	P
		Solid Ice Deformation Shock Waves			
★	this work	0.37 – 5.32	92-102	12	P
▽	*Anderson* [1968]	3.55 – 30.10	263	5	P
◎	*Anderson* [1968]	18.00 – 27.40	263	2	S
⊠	*Gaffney* [1973]	0.46 – 0.85	263 ± .1	0	P
□	*Bakanova et al.* [1976]	3.43 – 50.30	258	7	P
⊗	*Gaffney and Ahrens* [1980]	1.91	263 ± .5	0	P
♦	*Larson* [1984]‡	0.42 – 3.56	263 ± 2	6	P
▲	*Larson* [1984]‡	0.26 – 0.31	263 ± 2	0	S
▶	*Gaffney and Smith* [1994]	0.68 – 2.92	263-266	1	P
◀	*Davies and Smith* [1994]	0.36 – 4.45	263-266	1	P

⊛Elastic shock amplitudes are principal stress; deformation shock amplitudes are pressure.

*In multiple wave region, 0.2-6 GPa, only steady wave measurements with jump conditions reported for each wave are included in this analysis. Above 6 GPa, all published data are included.

†P-polycrystalline ice sample, S-single crystal ice sample.

‡Includes revised analysis of data from *Larson et al.* [1973].

2.2 Experimental Procedures and Data Analysis

We utilized the embedded electromagnetic particle velocity gauge technique [*Dremin and Shvedov*, 1964; *Dremin and Adadurov*, 1964; *Petersen et al.*, 1970] to measure shock velocities and wave profiles in ice. The technique is illustrated in Figure 2.2. *Larson et al.* [1973] and *Larson* [1984] used the same technique. In this work, we use the vaporization of liquid N_2 in air as a cooling system and conduct our experiments at lower initial temperatures.

The gauges are embedded between ice discs, and the target is hung in the presence of a magnetic field which is perpendicular to the long axis of the gun. The particle velocity gauges used in this study are composed of a loop of 0.5 mil (12.7 μm) thick copper film

between two 1 mil layers of polyimide (Kapton). The copper film's active area is 9×4 mm, with leads that are 0.5 mm wide. The gauges were custom made by Dynasen, Inc. (Goleta, CA). The gauges are oriented such that the 9 mm element is perpendicular to the field lines and aligned so that the motion of the shock wave, under uniaxial strain conditions, induces motion which is also perpendicular to the magnetic field.

When subject to an impact, the particle velocity associated with the shock wave induces a voltage, E, across the gauges, which is given by

$$E(t) = HLu_p(t), \tag{2.1}$$

where H is the magnetic field strength in Tesla, L is the length of the element in the gauge which is perpendicular to the field lines, in this case 0.009 m, and $u_p(t)$ is the particle velocity of the gauge as a function of time, in m s^{-1}. The voltage across each gauge is recorded by an oscilloscope, terminated in 50 Ω, via 50 Ω BNC coaxial cables.

The major benefits of this technique are the minimal thickness of the gauges and the direct Lagrangian measurement. The 2.5 mil (63.5 μm) thick gauges equilibrate with the surrounding ice within about 20 ns (the longitudinal sound speed in polyimide is 2.72 km s^{-1}, *Marsh*, 1980). Present digital oscilloscopes (HP 54540A, Gould Classic 6500) have a time resolution of 2 ns. Thus, the resolution of the shock profile is inherently limited by the gauge thickness. The polyimide has only a slightly greater shock impedance than ice, and the rise time of the shocks in this study ($\leq$ 5.2 GPa) are greater than 20 ns. Hence, the present gauges react minimally with the ice shock, unlike previous experimental difficulties related to impedance mismatch between the gauge and ice [e.g., *Gaffney*, 1973; *Gaffney and Smith*, 1994; *Davies and Smith*, 1994].

The use of multiple Lagrangian gauges permitted measuring the shock velocity from the travel time between gauges. Lagrangian analysis of the gauge profiles, described below, yields the shock loading (and unloading) stress-volume paths when the conditions of uniaxial strain are satisfied.

The primary drawback of the electromagnetic particle velocity gauge technique is the requirement that the science sample, target assembly, and projectile contain no moving electrically conducting materials that would disrupt the static magnetic field. This restriction inherently limits the shock pressure range that may be studied. These experiments

were conducted on the 40 mm single stage propellant gun in the Lindhurst Laboratory of Experimental Geophysics, which has a maximum projectile velocity of about 2.6 km s^{-1}. The impact velocity is measured by the time interval (recorded with RACAL-DANA #1991 universal counters) between extinction of three He-Ne laser beams in the projectile path and from a double X-ray exposure of the projectile at a measured time separation [c.f., *Miller et al.*, 1991].

2.2.1 Target Assembly

The target is comprised of multiple ice discs. Solid ice discs, with 50 mm diameters, were cored from a large block of transparent, bubble-free commercial carving ice (Carving Ice, Anaheim, CA). The ice samples were polycrystalline with a preferential crystal orientation. Solid ice experiments were aligned so that the shock propagates along an axis perpendicular to the ice Ih *c*-axis. The solid ice discs were polished (400-600 grade sandpaper, parallel within 0.1 mm) in the N. Mudd Ice Laboratory and the thickness measured 1-3 days prior to shock loading.

The gauges are centered between the ice discs and held together in a polycarbonate target assembly, shown in Figure 2.2B (inset). No glues were used to keep the gauges in contact with the ice discs. As the targets were stored in air at $-8°C$, the ambient humidity caused the discs of ice to sinter together around the gauges. Each target contained 3 or 4 gauges, usually with one gauge at the impactor-target interface. In most experiments, a 0.7 mm-thick polycarbonate disc was placed in front of the first gauge to provide good gauge-ice contact. Two thermocouples (Omega Chromega-Alomega(TM) #CHAL-020, K-type) were placed in each target assembly to monitor the temperature of the ice.

The target was hung on axis with the gun between two stacks, each of two permanent magnets ($2 \times 2 \times 1/2''$, 0.122 Tesla NdFeB, Magnet Sales & Mfg., Inc., Culver City, CA). The two magnet stacks are positioned in a U-shaped steel mount set perpendicular to the gun axis, Figure 2.2. A nearly uniform static field is generated over an area of about 2×2 cm between the two sets of magnets (see next section). The target is hung so that the particle velocity gauges occupy the most uniform part of the field, although the data analysis includes a correction for the field edge profile. The target is aligned using a barrel-aligned laser. The light is reflected from a mirror, placed on the target face during alignment, back to the laser source, over a one-way path of about 10 m, aligning the target face to

the barrel within 1 mrad. The magnets are aligned within 10 mrad using the barrel laser. The tilt of the projectile is not measured directly. The X-ray images used to measure the projectile velocity also provide a confirmation of the orientation of the projectile at about 10 cm prior to impact. Non-parallel faces in individual ice discs is the largest contributor to the non-planarity in the experiments, up to several mrad.

The target is transported to the shock wave in a cooler over a liquid nitrogen (lN_2) bath, at about $-20°C$. The target is cooled by spraying lN_2 ($\sim$ 77 K), onto the target under ambient pressure (#32885K11 full cone brass spray nozzles, $\sim$ 0.2 gpm at 30 psi lN_2 tank pressure, McMaster-Carr, Los Angeles, CA). The target is surrounded by a foam cooling box (PVC, 0.5" thick, McMaster-Carr) which is interior to the magnets. Figure 2.2B shows the configuration of the target, magnets, cooling spray, and cooling box in front of the gun muzzle. The front of the cooling box has a hole cut out to allow the projectile to pass through unimpeded. The hole is covered with transparent 10 μm plastic wrap (Johnson Handi-wrap) to seal the cooling box while contributing minimal interference to the projectile flight path. Once the ice is cooled to initial temperatures of about 90 K, the target tank is evacuated to pressures of $\sim 200 - 400$ mtorr prior to impact.

2.2.2 Lagrangian Data Analysis

The voltage record is converted to particle velocity by using Eq. 2.1 and the map of the magnetic field. Before every shot, the magnetic field is mapped, using a transverse Hall probe (Magnetic Instrumentation Inc., Indianapolis, IN, #7300-039R and Thomas & Skinner 8315 Gaussmeter), along and both 5 mm above and below the gun axis, over the same volume occupied by the 9-mm long gauges, Figure 2.3. The scatter in the field measurement, typically < 0.5 mT, results in less than a 1% uncertainty in particle velocity.

The axial stress-volume loading paths are calculated using a Lagrangian analysis of the wave profiles from each gauge [*Cowperthwaite and Williams*, 1971]. Based on conservation of mass and linear momentum,

$$\left(\frac{\partial V}{\partial u_p}\right)_h = -\frac{V_0}{C_{u_p}}, \tag{2.2a}$$

$$\left(\frac{\partial \sigma}{\partial u_p}\right)_h = \frac{C_\sigma}{V_0}, \tag{2.2b}$$

where V is the specific volume, V_0 is the initial specific volume, h is the Lagrangian

coordinate corresponding to the initial position of the gauge, and σ is the axial stress for one-dimensional strain. The phase velocities, C_{u_p} and C_σ [*Fowles and Williams*, 1970], are defined by

$$C_{u_p} = (\partial h/\partial t)_{u_p}, \tag{2.3a}$$

$$C_\sigma = (\partial h/\partial t)_\sigma. \tag{2.3b}$$

In a steady shock wave, the phase velocities are equal [*Cowperthwaite and Williams*, 1971]. Because shock waves in ice exhibit multiple-wave structure, phase velocities are not independent of stress [*Larson*, 1984].

The discontinuity between the initial state, $_0$, and shock state, $_i$, is described by the Rankine-Hugoniot (RH) mass, momentum and energy conservation equations,

$$u_{p,i} - u_{p,0} = U_S \left(1 - \frac{V_i}{V_0}\right) \tag{2.4a}$$

$$P_i - P_0 = \frac{U_S}{V_0} (u_{p,i} - u_{p,0}) \tag{2.4b}$$

$$E_i - E_0 = \frac{1}{2} (P_i - P_0) (V_0 - V_i) \tag{2.4c}$$

where u_p is the particle velocity, U_S is the shock velocity, and E is the specific internal energy.

In the shock front, pressure and particle velocity are directly related through conservation of momentum, Eq. 2.4b; therefore, the phase velocity $C(u_p) = C_\sigma(u_p) = C_{u_p}(u_p)$ can be calculated as a function of particle velocity. The travel time associated with a particle velocity and gauge (gauges 2-4), $\Delta t(u_p)_g$, is calculated using the wave profile at the impact plane (gauge 1). The rise time of the wave at the impact plane is non-zero, so the travel time is calculated at every u_p using the Lagrangian distance, h_g, from the impact plane to each gauge, $_g$. The phase velocity is

$$C(u_p)_g = h_g/\Delta t(u_p)_g. \tag{2.5}$$

Now Eqs. 2.2a and 2.2b may be integrated to calculate the stress and specific volume as a function of time for each gauge after the impact plane gauge, as shown in Figure 2.4. The initial specific volume, V_0, is taken from the published crystal density of ice [*Hobbs*, 1974],

corrected for the initial temperature. The initial pressure is assumed to be zero.

Finally, the phase velocity at the wave arrival is equal to the Lagrangian shock velocity, U_S^L. The Eulerian shock velocity, U_S, is related to the Lagrangian shock velocity by

$$U_S = (V_i/V_0)U_S^L. \tag{2.6}$$

The Lagrangian wave velocity is larger than the Eulerian wave velocity in wave feature $_i$ by the particle velocity from the previous wave feature, $_{i-1}$:

$$U_{S,i}^L = U_{S,i} + u_{p,i-1} \tag{2.7}$$

The tabulated Eulerian shock wave velocity, U_S, is a material property and independent of the motion of the material.

Three Hugoniot states for each shock wave were obtained from the Lagrangian analysis of particle velocity traces from four gauges. For each shock front, we identify the time interval corresponding to the flat-topped region of each wave, as a grey-colored region in Figure 2.5. The particle velocity, pressure, and specific volume are averaged over this interval to determine the shock state. The tabulated error associated with each measurement is the larger of either the scatter in the top of the wave or the formal error propagated throughout the Lagrangian analysis [*Bevington*, 1969]. The associated shock velocity is uniquely determined from the RH equations. Note that a small amplitude < 0.1 GPa wave seems to precede the 0.5 GPa elastic limit precursor in Figures 2.4A and 2.5. Split elastic precursor waves have been previously reported in iron [*Bancroft et al.*, 1956]. A few gauge profiles in the high-pressure experiments suggest that this may occur in ice, but it is difficult to distinguish this apparent wave arrival from that inherent upon slight tilt ($\sim 1°$) of the impactor.

We used polycarbonate (Lexan) projectiles (average $\rho_0 = 1.19$ g cm^{-3}) with cylindrical dimensions of diameter 40 mm and length 64 mm. The polycarbonate Hugoniot has been well measured at particle velocities between about 0.5-5.0 km s^{-1} [*Marsh*, 1980]. The impedance match shock state based on the polycarbonate Hugoniot and impact velocity is in extremely good agreement with the peak shock state derived in the Lagrangian analysis, given in Table 2.2. The temperature difference between the projectile (room temperature) and the 0.7 mm polycarbonate plate at the front of the ice discs has a negligible effect on the density and peak shock state. Using the new shock wave data in ice obtained from the

Lagrangian analysis, in the particle velocity range from 100-600 m s^{-1}, and the shock states compiled in *Marsh* [1980], we are able to refine the very low particle velocity region of the polycarbonate Hugoniot, given as a multi-part function:

$$U_S = \begin{cases} 2039^{(\pm 78)} + 2.01^{(\pm 0.16)} u_p, & u_p \leq 768 \\ 2402^{(\pm 46)} + 1.542^{(\pm .028)} u_p, & 764 < u_p \leq 2644 \\ 5350^{(\pm 260)} + 0.428^{(\pm .084)} u_p, & 2644 < u_p \leq 3427 \\ 1910^{(\pm 320)} + 1.431^{*\pm .076)} u_p, & u_p > 3427, \end{cases} \tag{2.8}$$

where U_S and u_p are given in m s^{-1} and the 1σ error for each parameter are given in parentheses. Our experiments are in the region of the two lowest velocity segments. Note that the first term (intercept) agrees closely with the bulk sound speed in polycarbonate, 1940 m s^{-1} [*Marsh*, 1980].

The final Hugoniot state from each experiment, Table 2.2, is an average of the measurements from each gauge beyond the impact plane. Notes and wave profiles are included in the supplemental information. The individual shock states from each gauge are listed in Table 2.3 and the $\sigma - V$ loading profiles are shown in Figure 2.6. Note that the measured $\sigma - V$ loading paths between each shock state are very close to ideal straight Rayleigh lines.

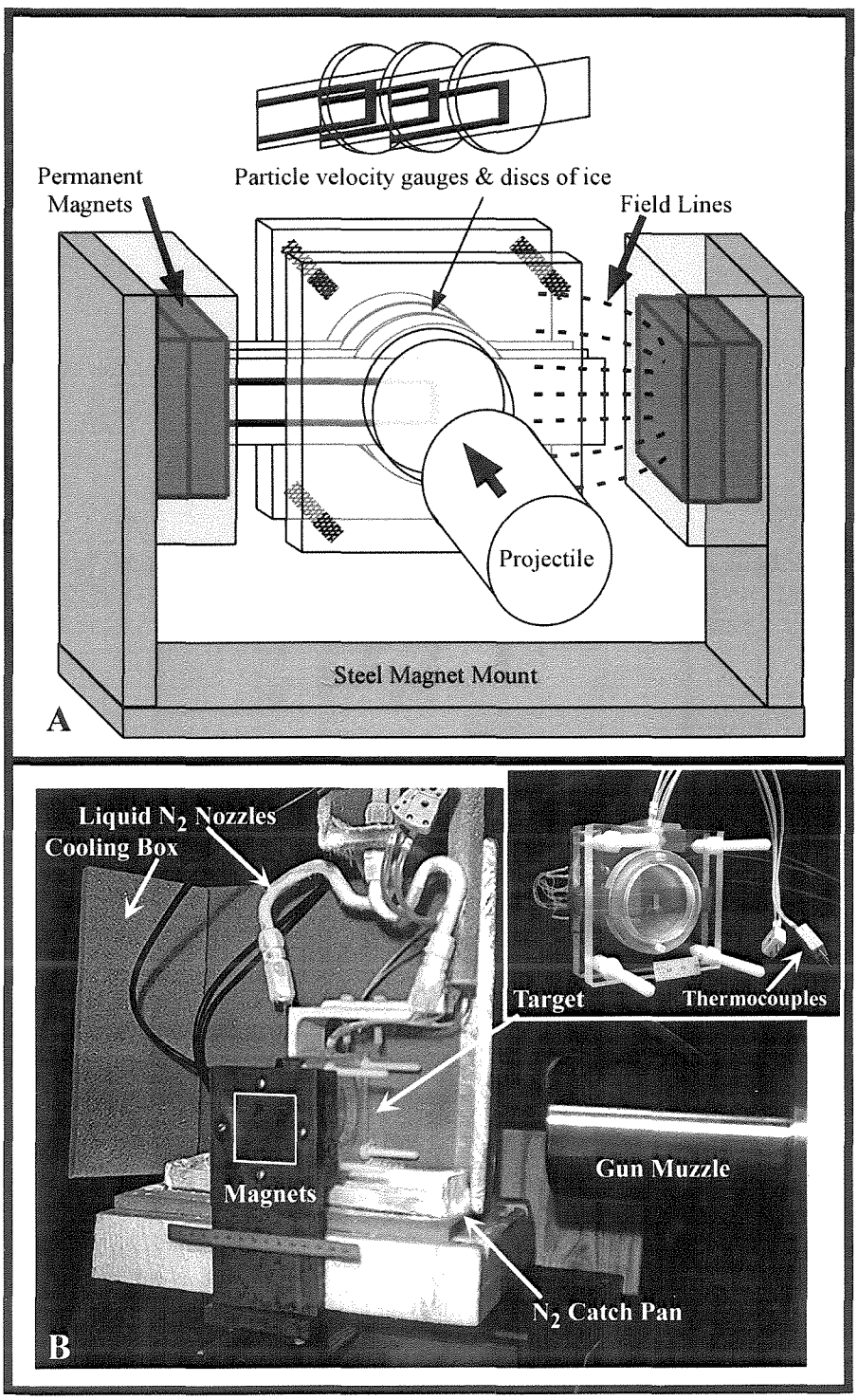
Permanent Magnets
Particle velocity gauges & discs of ice
Field Lines
Projectile
Steel Magnet Mount
A
Liquid N_2 Nozzles
Cooling Box
Target
Thermocouples
Magnets
Gun Muzzle
N_2 Catch Pan
B

Figure 2.2: A. Composite schematic sketch and photographs of experimental arrangement for particle velocity gauge technique. Electromagnetic particle velocity gauges are embedded between ice discs and mounted on gun axis, perpendicular to projectile path. Motion due to impact is perpendicular to magnetic field lines. **B.** Target is cooled with liquid nitrogen spray in a foam cooling box prior to impact. A hole is cut in cooling box along projectile path (not visible).

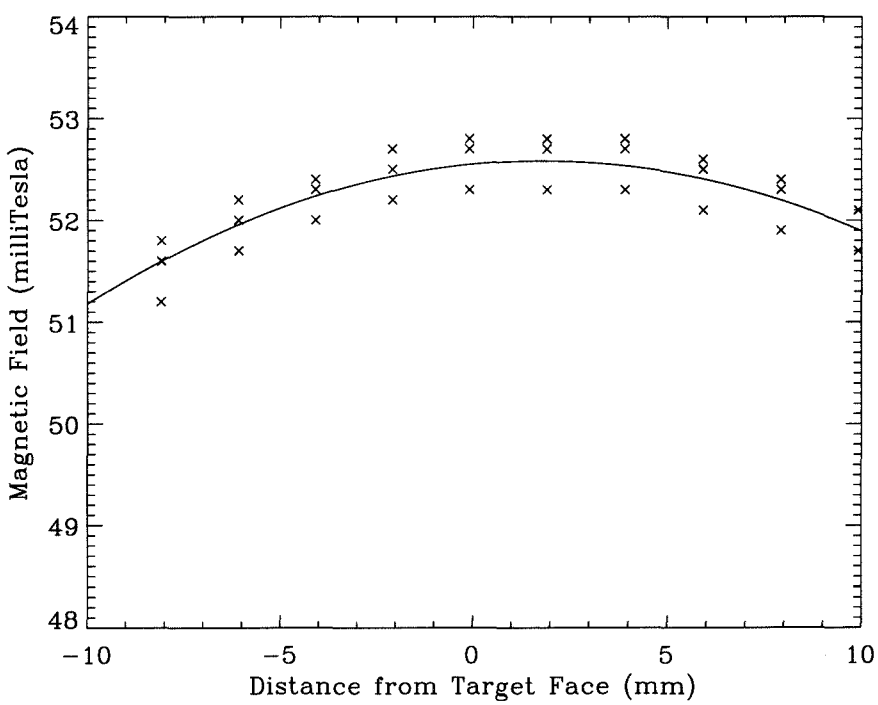

Figure 2.3: Magnetic field generated by permanent magnets (Fig. 2.2) is measured prior to each shot with transverse Hall probe. × indicate measurements along and both 5 mm above and below gun axis. The curved fit is used to reduce data. (Data from shot #1040.)

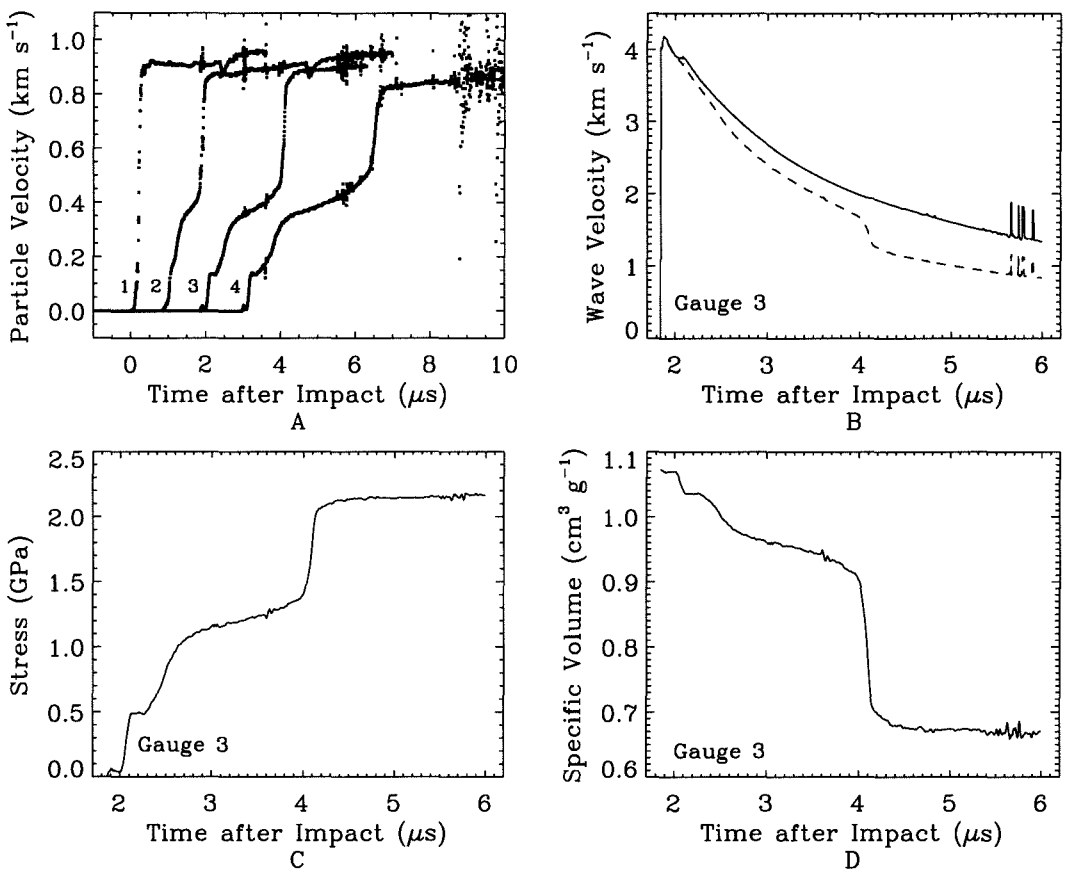

Figure 2.4: Example of Lagrangian analysis method. **A**. Particle velocity traces for all 4 gauges in shot #1043. **B**. Lagrangian wave velocity (solid line) and Eulerian wave velocity (dashed line) vs. time between gauges 1 and 3 (located at $h = 7.50$ mm). **C**. Stress vs. time from Eq. 2.2b. **D**. Volume vs. time from Eq. 2.2a.

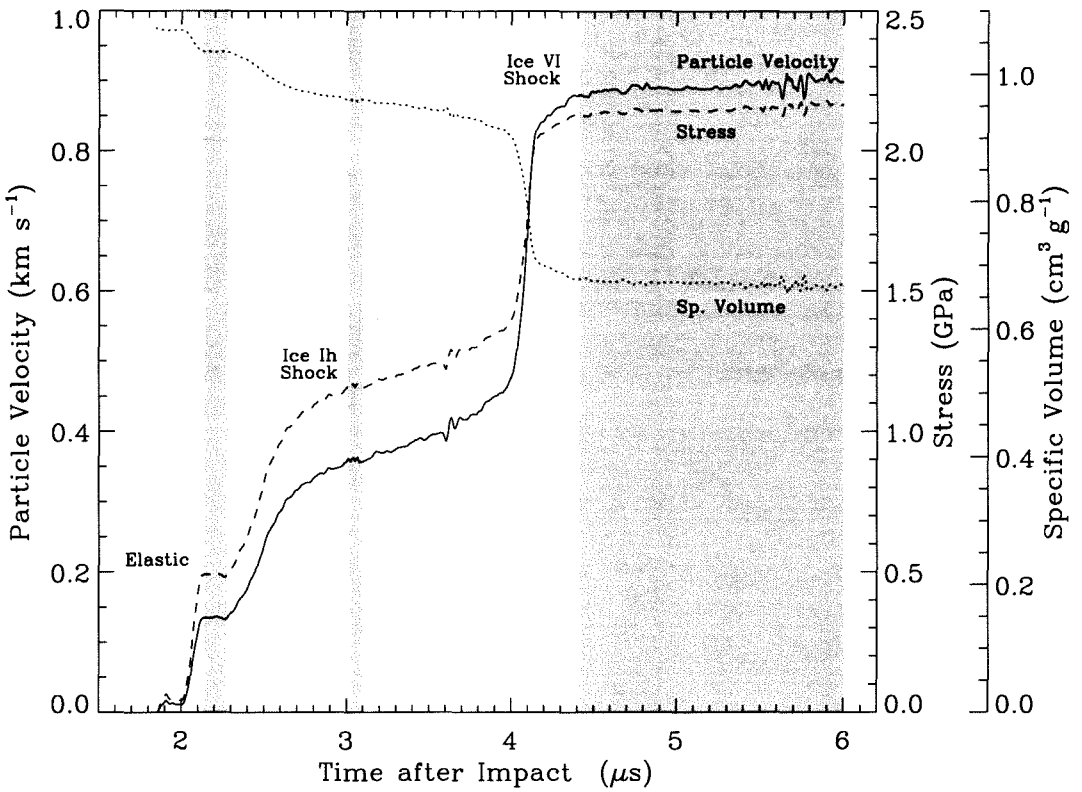

Figure 2.5: Hugoniot state averaging of the Lagrangian analysis, shown is shot #1043 gauge 3 record, with measured particle velocity (solid curve), calculated stress (dashed curve), and calculated specific volume (dotted curve). Hugoniot stress and volume values are averaged over shaded region time window, defined by flat-topped region of particle velocity profile. Corresponding Eulerian shock velocity is determined by Rankine-Hugoniot equations.

Table 2.2. Average final Hugoniot states.

	Initial Conditions			Peak Ice Shock State[d]		Impedance Match[e]	
Exp. #	T_0[a] (K)	ρ_0[b] (kg m^{-3})	V_i[c] (m s^{-1})	u_p (m s^{-1})	P (GPa) (MPa)	u_p (m s^{-1})	P (GPa)
I44	69	932.8	273	125 (3.3)	0.401 (54.5)	129	0.41
I45	92	932.5	315	151 (3.2)	0.453 (7.4)	154	0.46
1046[f]	95	932.4	687	366 (2.6)	···	409	1.03
1047	98	932.4	1111	696 (8.6)	1.554 (128.4)	667	1.42
1043	102	932.3	1473	883 (4.2)	2.131 (47.5)	910	2.27
1045[f]	92	932.5	2618	1597 (11.)	5.178 (93.0)	1571	4.99

[a]Uncertainty of T_0 is usually a few degrees. See supplemental information.

[b]Uncertainty (1σ) of solid ice density is ± 0.7 kg m^{-3} [*Hobbs*, 1974].

[c]Uncertainty ($\pm 3\sigma$) of impact velocity $\leq 2\%$.

[d]Final Hugoniot state is highest pressure state derived from Lagrangian analysis. When peak pressure cannot be determined, only peak particle velocity is reported. See supplemental information.

[e]Impedance match solution is calculated shock state in polycarbonate projectile from impact velocity and particle velocity and pressure in ice.

[f]See Appendix A.

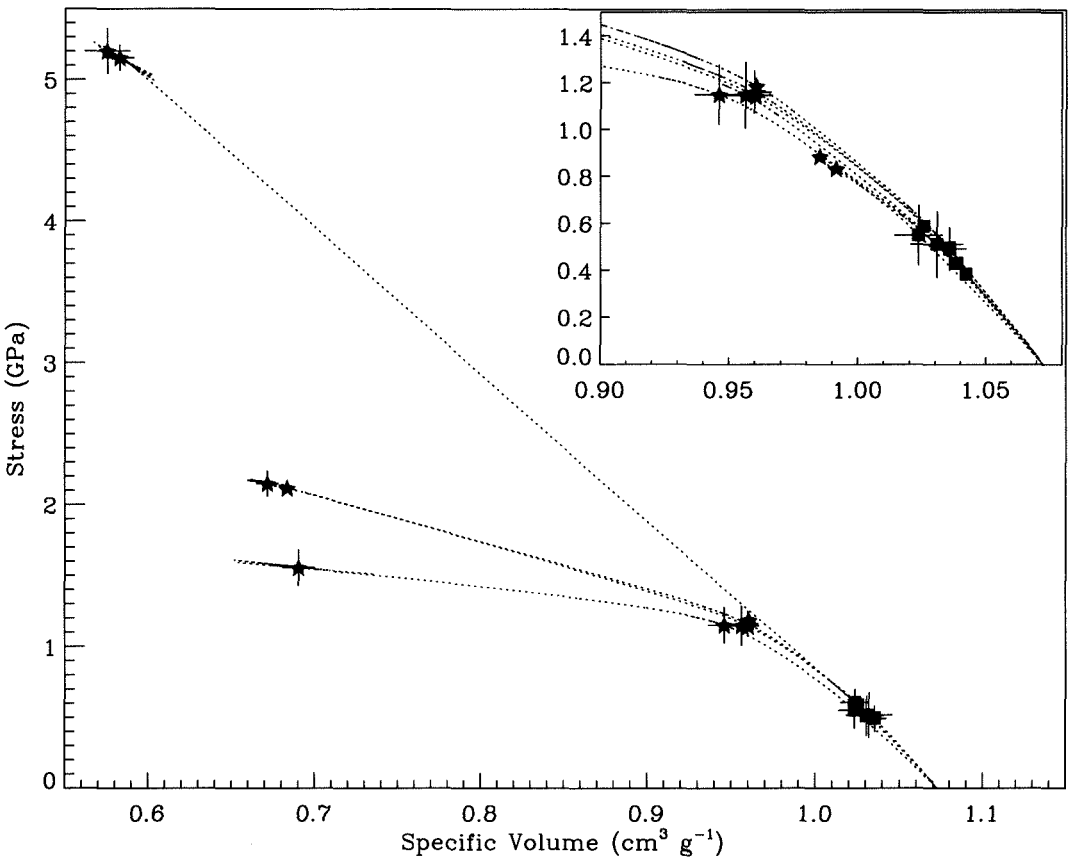

Figure 2.6: Shock loading paths (dotted lines), Hugoniot states (★), and HEL precursor states (■) in ice derived from Lagrangian analysis. Loading paths are noticably curved overall and straight between shock states (values in Table 2.3).

Table 2.3. New ice Hugoniot data.

Exp. #	Feature[‡] G-Wave #	u_p (m s^{-1})	U_s (m s^{-1})	ρ (kg m^{-3})	P (GPa) (MPa)
I44	Impact Plane	127.6 (5.7)	...	...	...
	Avg., wave 1	100.7 (0.6)	3868 (29)	958 (1.0)	0.357 (28)
	G 2, wave 1	105.2 (0.9)	3767 (48)	960 (1.8)	0.367 (55)
	G 2, wave 2*	124.8 (3.3)	2369 (20)	970 (3.7)	0.401 (55)
	G 3, wave 1	96.3 (0.9)	3969 (32)	956 (0.9)	0.347 (11)
	G 3, wave 2*	118.5 (2.9)	2920 (24)	965 (1.6)	0.401 (11)
	G 4, wave 1*	78.2 (0.9)	4146 (38)	951 (0.9)	0.289 (11)
	G 4, wave 2*	102.5 (1.6)	3125 (25)	959 (0.9)	0.359 (11)
I45	Impact Plane	154.9 (5.0)	...	...	...
	Avg., wave 1	115.3 (1.4)	3408 (25)	963 (1.0)	0.380 (7)
	G 2, wave 1	115.3 (1.4)	3408 (25)	963 (1.0)	0.380 (7)
	G 2, wave 2*	151.3 (3.2)	2098 (60)	981 (1.4)	0.453 (7)
	G 3, wave 1*	75.8 (0.7)	3591 (29)	952 (6.2)	0.255 (72)
	G 3, wave 2*	135.7 (0.7)	2580 (240)	974 (6.5)	0.407 (72)
	G 4, wave 1*	91.9 (1.4)	3230 (23)	959 (2.0)	0.276 (20)
	G 4, wave 2*	131.5 (0.9)	2477 (76)	975 (2.1)	0.369 (20)
1046	Impact Plane	365.8 (2.6)	...	...	...
	Avg., wave 1	114.4 (1.7)	3828 (21)	961 (0.7)	0.408 (7)
	Avg., wave 2	267.4 (1.0)	2991 (17)	1011 (0.8)	0.860 (7)
	G 2, wave 1	120.9 (2.3)	3827 (30)	962 (1.0)	0.431 (9)
	G 2, wave 2	276.2 (1.6)	3014 (24)	1015 (1.1)	0.886 (9)
	G 3, wave 1	107.9 (2.5)	3830 (30)	959 (1.0)	0.384 (10)
	G 3, wave 2	258.5 (1.2)	2968 (23)	1008 (1.1)	0.834 (11)
1047	Impact Plane	701.0 (2.7)	...	...	...
	Avg., wave 1	155.1 (1.9)	3653 (30)	973 (6.6)	0.530 (96)
	Avg., wave 2	370.9 (2.0)	3219 (30)	1051 (7.7)	1.148 (96)
	Avg., wave 3	695.9 (8.6)	1196 (22)	1449 (20.0)	1.550 (130)
	G 2, wave 1	164.2 (2.7)	3597 (43)	977 (9.0)	0.550 (130)
	G 2, wave 2	378.7 (2.7)	3188 (39)	1057 (11.0)	1.150 (130)
	G 2, wave 3	695.9 (8.6)	1196 (22)	1449 (20.0)	1.550 (130)
	G 3, wave 1	146.1 (2.7)	3708 (42)	969 (9.4)	0.510 (140)
	G 3, wave 2	363.2 (3.0)	3251 (46)	1046 (11.0)	1.150 (140)
1043	Impact Plane	911.2 (4.8)	...	...	...
	Avg., wave 1	145.6 (2.2)	3855 (17)	968 (2.2)	0.525 (32)
	Avg., wave 2	359.4 (1.9)	3361 (15)	1041 (2.5)	1.163 (32)
	Avg., wave 3	882.7 (4.2)	1757 (10)	1475 (7.8)	2.131 (48)
	G 2, wave 1	166.5 (4.8)	3754 (29)	975 (1.7)	0.589 (23)
	G 2, wave 2	356.1 (3.3)	3330 (26)	1041 (2.0)	1.142 (23)
	G 2, wave 3	873.6 (4.5)	1811 (14)	1462 (6.4)	2.114 (23)
	G 3, wave 1	134.6 (3.3)	3900 (30)	965 (6.2)	0.491 (92)
	G 3, wave 2	359.4 (3.3)	3361 (27)	1041 (7.2)	1.160 (92)
	G 3, wave 3	891.9 (7.1)	1703 (15)	1489 (15.0)	2.148 (92)

Table 2.3. (continued)

Exp. #	Feature‡ G-Wave #	u_p (m s^{-1})	U_s (m s^{-1})	ρ (kg m^{-3})	P (GPa) (MPa)
	G 4, wave 1	135.6 (3.3)	3911 (29)	965 (1.6)	0.496 (20)
	G 4, wave 2	362.7 (3.3)	3391 (26)	1041 (1.8)	1.186 (20)
	G 4, wave 3*	833.0 (11.0)	1604 (12)	1422 (14.0)	2.051 (20)
1045	Impact Plane	1606.0 (16.0)	...	...	...
	Avg., wave 1	157.9 (4.8)	3700 (46)	972 (7.6)	0.560 (93)
	Avg., wave 2	1597.0 (11.0)	3275 (34)	1727 (24.0)	5.178 (93)
	G 2, wave 1*	112.2 (7.8)	3500 (1000)	960 (300.0)	0.400 (3000)
	G 2, wave 2*	1581.0 (6.9)	3130 (950)	1690 (920.0)	5.100 (3000)
	G 3, wave 1	171.7 (6.8)	3619 (35)	976 (8.1)	0.605 (92)
	G 3, wave 2	1588.0 (18.0)	3235 (50)	1716 (25.0)	5.154 (92)
	G 4, wave 1	144.0 (6.8)	3781 (85)	969 (13.0)	0.520 (160)
	G 4, wave 2	1607.0 (13.0)	3315 (46)	1739 (42.0)	5.200 (160)

‡Impact plane entry records peak particle velocity at ice-polycarbonate buffer interface. G # denotes gauge, numbered 1, 2, etc., from the impact plane. Average values recommended for denoted wave feature by combining all the gauge records.

*Indicates that this data point has a problem and should be considered unreliable. The most common problem is a partially released wave. Refer to the experimental details in Appendix A for each individual case.

2.3 Results and Interpretation

2.3.1 The $U_S - \Delta u_p$ Shock Equation of State

The dynamic response of ice Ih is temperature dependent, and multiple-wave shock fronts, which include phase transformation shocks, develop when the peak pressure is less than 6 GPa. To separate the effects of temperature and phase transformations, we consider each shock wave jump independently. Figure 2.7 compares two idealized multiple-wave shock profiles and their corresponding stress-volume loading paths, based on this work and *Larson* [1984], at different initial temperatures with peak shock stress near 1.6 GPa. In this example, the final wave in both shock fronts is a transformation shock to the ice VI structure (see section 2.4.3). The amplitude of first wave (σ_E), the elastic precursor, is much larger at $T_0 = 100$ K, with $\sigma_E = 0.55$ GPa, than at 263 K, when $\sigma_E = 0.17$ GPa. In addition, a steady 3-wave shock front develops at 100 K, with an intermediate shock in the ice Ih structure. Notably, *Larson* [1984] reported a 2-wave shock front in all experiments at 263 K, with peak shock stress spanning 0.26-3.56 GPa. In the wave profile from *Larson* [1984] at $T_0 = 263$ K, the shock jump associated with the transformation to ice VI has $\Delta u_p = 700$ m s^{-1}, corresponding to $\Delta\sigma = 1.4$ GPa. In comparison, the ice VI shock in the 100 K profile has an amplitude of $\Delta u_p = 540$ m s^{-1} and $\Delta\sigma = 0.4$ GPa. Although the final particle velocity and stress are similar in these two experiments, the loading path and shock front depend significantly on the initial temperature.

Previous studies (Table 2.1) have fit $U_S - \Sigma u_p$ data [e.g., *Gaffney*, 1985], but the temperature-dependent response of ice Ih complicates direct comparison of Σu_p between datasets, as shown in Figure 2.7. We find that a rigorous comparison is made by considering the variables U_S, the Eulerian shock velocity, and Δu_p for each wave feature. In this case, each $U_S - \Delta u_p$ pair is described by the RH equations centered in the previous state. In the Figure 2.7 example at $T_0 = 100$ K, the ice VI transformation shock is centered in the ice Ih shock state, corresponding to state $_0$ in Eq. 2.4.

Different $U_S - \Delta u_p$ curves describe each shock process, e.g., elastic shock, ice Ih shock, and ice VI transformation shock. With this approach, the $P - V$ Hugoniot is assembled in segments, where the $P - V$ center for each segment is temperature dependent. Previous studies measuring multiple-wave shock fronts report $U_S - \Sigma u_p$ curves which describe the Hugoniot by a single application of the RH equations from the initial, zero-pressure state.

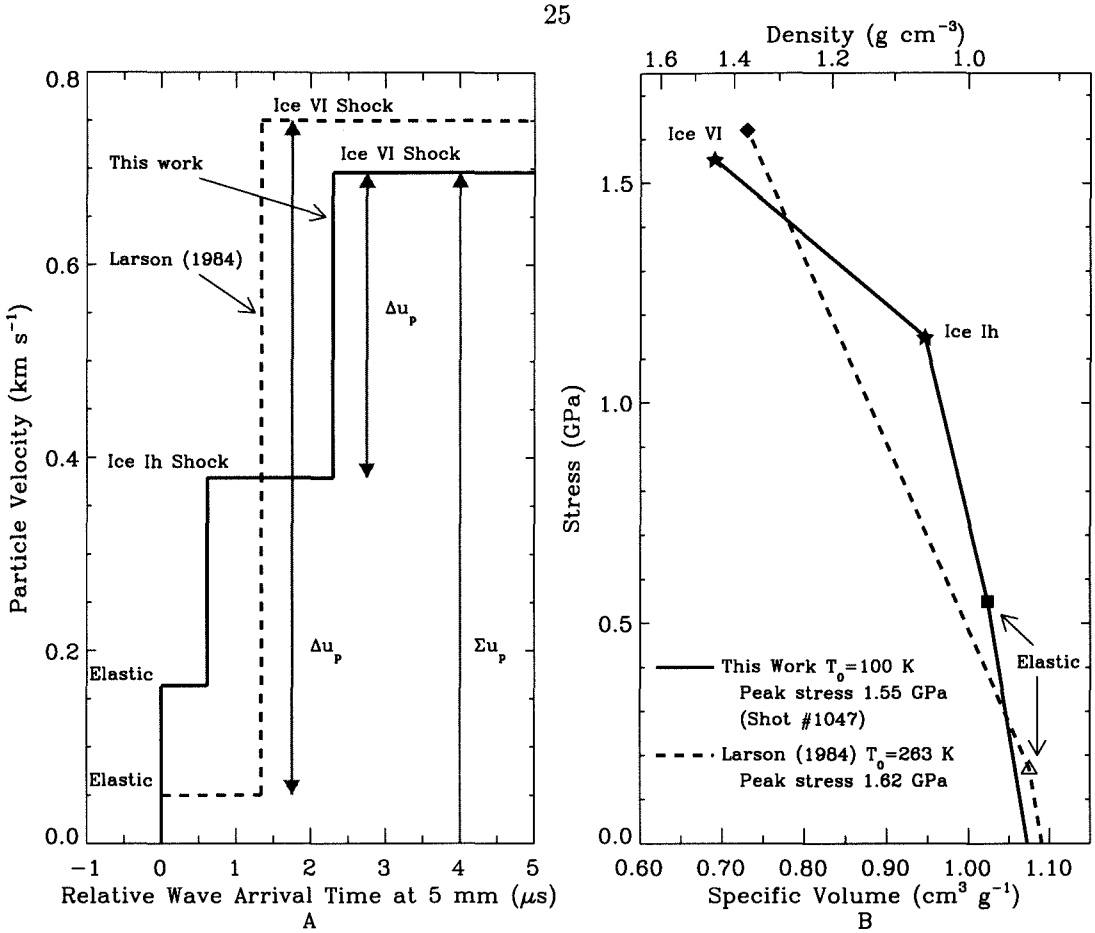

Figure 2.7: Idealized $\sim$ 1.6 GPa shock profiles in solid ice comparing this work (T_0 = 100 K, solid lines) to *Larson* [1984] (T_0 = 263 K, dashed lines). **A.** Multiple-wave shock front profiles 5 mm from impact plane. Full compression is achieved by two or three discrete shock jumps. **B.** Compression curves corresponding to shock profiles in A.

Although simpler in application, centering all the RH jump relations at zero pressure results in loss of the information describing individual waves in the shock front.

$U_s - \Delta u_p$ data for each shock jump from this work and previous studies with multiple-wave shock front information are compiled. We fit different $U_S - \Delta u_p$ segments grouped by shock process, as shown in Figure 2.8, where the symbols correspond to the data source listed in Table 2.1. We find 5 clear regions on the solid ice Hugoniot: (1) elastic shock precursors, (2) deformation shocks in the initial ice Ih structure, and transformation shocks to (3) ice VI, (4) ice VII and (5) liquid water. The coefficients for the least squares linear fits to each segment are given in Table 2.4, and the corresponding initial state (and its dependence on temperature) is discussed in section 2.3.2. Linear $U_S - \Delta u_p$ fits are justified by the negligible effect of the second derivative of the bulk modulus over this pressure range

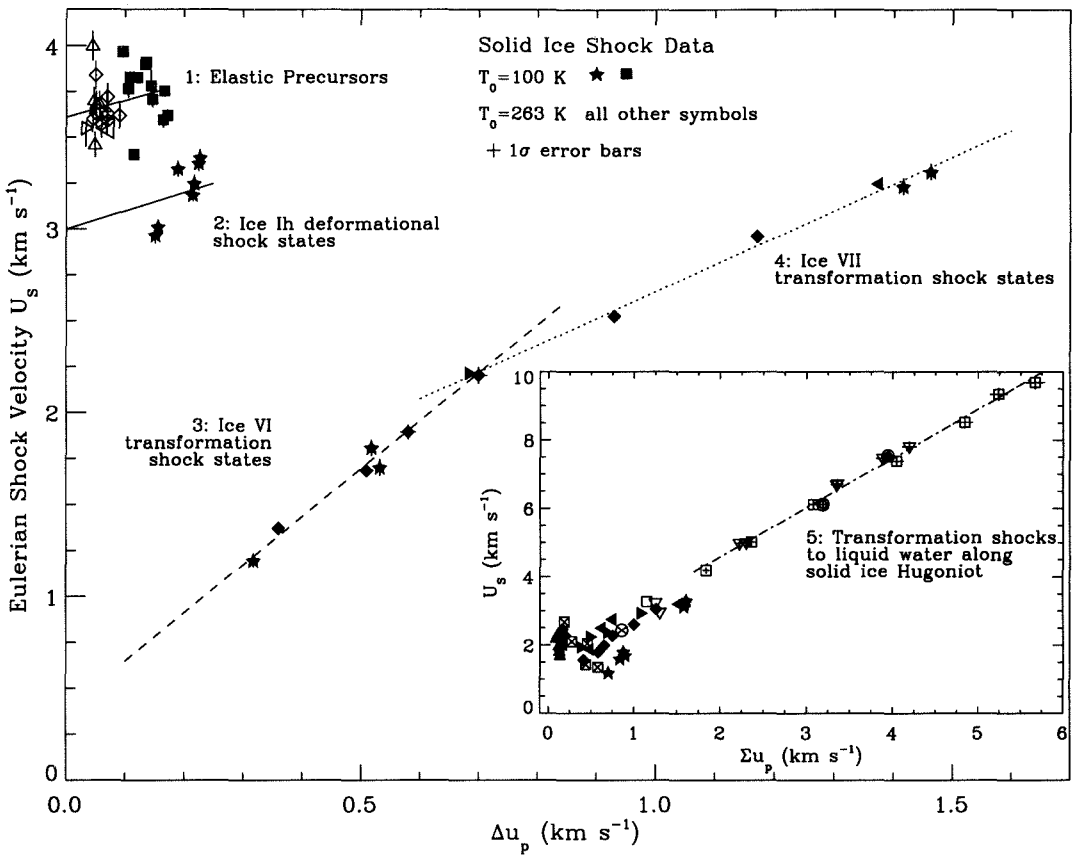

Figure 2.8: $U_S - \Delta u_p$ solid ice shock states fall into five groups: (1) elastic shock precursors with average wave velocity of longitudinal sound speed ($\sim$ 3.7 km s^{-1}), (2) deformation shocks in ice Ih with intercept at bulk sound speed ($\sim$ 2.9 km s^{-1}), and transformation shocks to (3) ice VI, (4) ice VII, and (5) liquid water. Available literature data (Table 2.1) and uncertainties (1σ) are included. All previously published data (inset) are plotted with previously used Σu_p abscissa.

[*Ruoff*, 1967; *Jeanloz*, 1979]. The limiting Δu_p values for each region is discussed below. We shall refer to linear fits in Table 2.4 as the $U_S - \Delta u_p$ equation of state (EOS), since these lines may be used with the RH equations to derive the pressure-volume shock Hugoniot.

Table 2.4. $U_S - \Delta u_p$ shock equation of state, $U_S = c + s\Delta u_p$, used to calculate solid ice Hugoniot.

Hugoniot Region	c (m s^{-1})	s ...	Δu_p range (m s^{-1}) min	max
1. Elastic	3610 (±61)	0.92 (±.63)	0	175
2. Ice Ih†	3000 (±100)	1.00 (±.80)	0	230
3. Ice VI	388 (±78)	2.61 (±.14)	100	850
4. Ice VII	1200 (±140)	1.46 (±.11)	600	1540
5. Liquid	1700 (±130)	1.440 (±.035)	1590	...

1σ uncertainties given in parentheses.

†Steady shock waves do not develop unless overdriven at low temperatures. Fixed bulk sound speed for ice Ih.

We find that the amplitude of elastic shock precursor waves is very sensitive to the initial temperature. In Figure 2.8, note the offset in the mean value of Δu_p between the low-temperature (T_0 = 100 K, ■) and temperate (T_0 = 263 K, open symbols) elastic precursor data (region 1). As a result, the transition point between the ice Ih elastic shock region to the ice Ih deformation shock region occurs at a different pressure along Hugoniots centered at different initial temperature.

We find that impacts in both low-temperature and temperate ice, reaching peak shock stress just above the elastic limit, do not form steady ice Ih deformation shock waves (refer to section 2.4.2). In low-temperature ice, steady ice Ih deformation shocks develop only as an intermediate state in the shock front between the elastic precursor wave and the transformation wave to ice VI (★ points in region 2, Figure 2.8). Note that no temperate ice data have been included in fitting region 2.

The $U_S - \Delta u_p$ EOS for shock-induced phase transformations (regions 3-5), however, appear to be independent of initial temperature over the range 100-263 K. There is excellent agreement between the low-temperature and temperate datasets in the ice VI and VII regions (3 and 4, Figure 2.8). By considering Δu_p instead of Σu_p, the temperature-dependent response of ice Ih is removed, and a shock-induced phase transformation is described by a $U_S - \Delta u_p$ EOS that is independent of the initial temperature.

At pressures above 6 GPa ($\Sigma u_p \geq 1590$ m s^{-1}, region 5), the shock velocities are greater than the longitudinal wave speed. In this case, the elastic precursor is overdriven, a single shock front develops, and $\Delta u_p = \Sigma u_p$. Therefore, Hugoniot data at pressures $\geq$ 6 GPa

are free from the ambiguities discussed above for shocks with peak stress < 6 GPa, which produce two- or three-wave shock fronts, depending on the temperature regime. The high-pressure ice Hugoniot data and $U_S - \Delta u_p$ EOS are shown in the inset in Figure 2.8 with all previously published data with $P < 6$ GPa, where U_S is plotted against Σu_p.

Note the considerable scatter in the low-pressure data, $\Sigma u_p < 1590$ m s^{-1} (regions 2-4), compared to the high-pressure data (region 5). For $\Sigma u_p < 150$ m s^{-1}, the scatter is attributed to the inclusion of ice Ih plastic waves in Hugoniot datasets. In the range $150 < \Sigma u_p < 2000$ m s^{-1} (Hugoniot regions 3 and 4), the low-temperature data lie at systematically lower U_S, where the plotted U_S corresponds to the Eulerian velocity of the final wave in the shock front. Because the low-temperature data have higher amplitude elastic precursors compared to the temperate shock data and intermediate ice Ih shocks (e.g., Figure 2.7), the amplitude of the final wave in the shock front is smaller and the shock velocity correspondingly slower compared to the temperate ice data. The scatter in the temperate shock data includes differences in the amplitude of the elastic precursor, data reduction problems, and experimental difficulties, such as the impedance mismatch between embedded gauges and ice described in section 2.2.

We note that our fit of the liquid water region on the ice Hugoniot (Table 2.4) agrees well with the high-pressure region of the temperate ice Hugoniot published by *Gaffney* [1985]. Gaffney fit $U_S = 1790 + 1.42 u_p$ for $P > 8$ GPa centered at $P = 0$ GPa and $\rho_0 = 918$ kg m^{-3}, but he could not reconcile the scatter in the data at pressures below 8 GPa.

2.3.2 The $P - V$ Hugoniot

Solid ice $P - V$ Hugoniots centered at $T_0 = 100$ (solid line) and 263 K (dashed line), calculated via application of $U_S - \Delta u_p$ segments, are shown in Figure 2.9 with the data that include multiple-wave shock front information.

The Hugoniots are centered at the 1 bar density of ice Ih at the specific volume corresponding to the initial temperature, where $V_0 = 1.089$ and 1.072 cm^3 g^{-1} at 263 and 100 K, respectively [*Hobbs*, 1974; *Röttger et al.*, 1994]. The first region on the Hugoniot is the locus of elastic shocks, centered on the initial state (V_0, σ_0), where $\sigma = 0$ GPa and the difference between the 1 bar and zero-pressure specific volume is ignored. The RH equations (Eq. 2.4) are applied with the elastic precursor $U_S - \Delta u_p$ EOS (Table 2.4) using (V_0, σ_0) as the initial state.

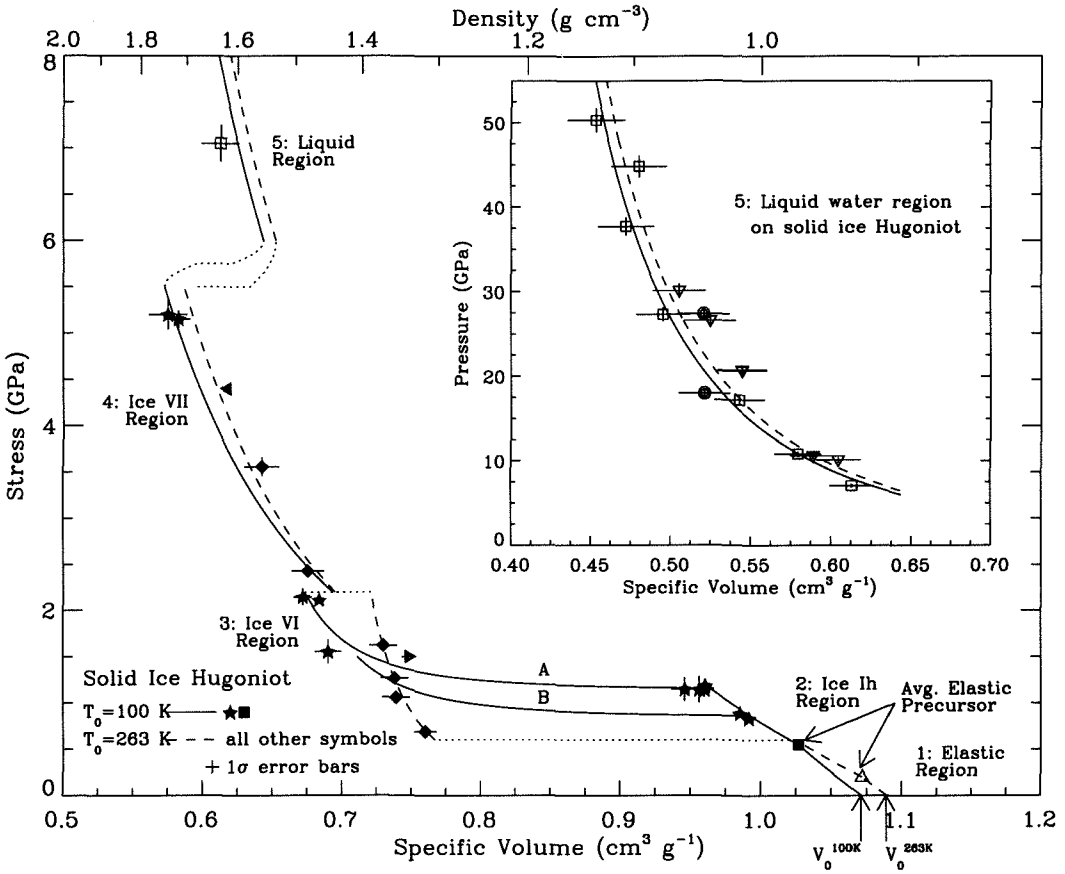

Figure 2.9: Solid ice Hugoniots centered at $T_0 = 100$ (solid lines) and 263 K (dashed lines). Hugoniot segments (1-5) derived from $U_S - \Delta u_p$ EOS given in Fig. 2.8 and Table 2.4. Available literature data (Table 2.1) and uncertainties (1σ) are included. Transition pressure between ice Ih and ice VI on 100 K Hugoniot is dependent on peak shock stress, e.g., paths A and B, refer to section 2.4.3.

The next region on the Hugoniot is the ice Ih deformation shock. The Hugoniot curve is obtained by application of the ice Ih $U_S - \Delta u_p$ EOS (Table 2.4) using the elastic precursor shock as the initial state, subscript $_{i-1}$. Then, the locus of $\sigma - V$ states is derived by

$$\sigma_i = \sigma_{i-1} + \frac{U_S \Delta u_p}{V_{i-1}} \tag{2.9a}$$

$$V_i = V_{i-1}\left(1 - \frac{\Delta u_p}{U_S}\right) \tag{2.9b}$$

where $\Delta u_p = u_{p,i} - u_{p,i-1}$. In the plotted ice Ih region, the initial state (V_{i-1}, σ_{i-1}) is the average elastic wave precursor state, where $\triangle = (1.07, 0.20)$ and $\blacksquare = (1.03, 0.55)$ in cm^3 g^{-1} and GPa at $T_0 = 263$ and 100 K, respectively (see section 2.4.1). We found that,

at low temperatures, supported ice Ih deformation shocks develop only as part of three-wave shock fronts. The ice Ih deformation shock data (★) shown in this region are intermediate waves in the shock front. At both initial temperatures, impacts resulting in peak stresses below 0.6 GPa drives a shock that separates into a two-wave profile, composed of the elastic precursor and a decaying plastic wave (not plotted in Figure 2.9, see section 2.4.2). Note that the ice Ih region on the 263 K Hugoniot in Figure 2.9 has no data points.

On the 263 K Hugoniot, the ice VI region begins at 0.6 GPa and the ice VII region begins are 2.2 GPa. Both the segments use the average 263 K elastic precursor (△) as the initial state for application of the $U_S - \Delta u_p$ EOS, as *Larson* [1984] reported two-wave shock profiles in these regions, composed of the elastic precursor and transformation shock (⧫).

On the 100 K Hugoniot, impact stresses reaching the ice VI region produce three-wave shock fronts, composed of the elastic precursor, an ice Ih deformation shock, and transformation shock to ice VI (e.g., Figure 2.7). In our experiments, the amplitude of the intermediate ice Ih shock varies with the peak shock stress. When the peak stress is greater than about 1.2 GPa, the ice Ih shock has an amplitude of 1.157 ± 0.017 GPa and specific volume of 0.9566 ± 0.0061 cm^3 g^{-1} (Exp. # 1043, 1047, Table 2.2), forming a cusp that defines the maximum stress on the ice Ih region of the Hugoniot. On the ice VI region of the 100 K Hugoniot, above 1.15 GPa, the initial state used in Eq. 2.9 is the ice Ih cusp, forming the base of the locus of shock states labeled A in Figure 2.9.

In one experiment (#1046), with a peak shock stress of 1.03 GPa, the intermediate ice Ih shock amplitude was 0.86 GPa, the base of the locus of shock states labeled B in Figure 2.9. We suggest that for final shock stresses greater than 0.6 GPa, ice VI will form on the low-temperature Hugoniot with an intermediate ice Ih shock with an amplitude that scales with the final shock stress, but limited by the 1.16-GPa cusp. Intermediate ice Ih shocks have been observed in some experiments at $T_0 = 263$ K [*Gaffney and Smith*, 1994; *Davies and Smith*, 1994], but the intermediate state was not a steady wave in any of the temperate experiments.

Note that the same $U_S - \Delta u_p$ EOS (Table 2.4) is used to calculated the ice VI region on both Hugoniots in Figure 2.9. The offset in specific volume between the 100 and 263 K Hugoniots in this region arises from the different initial state used in application of Eq. 2.9. At low temperatures, the initial state is an ice Ih shock, but under temperate conditions, the initial state is the elastic wave precursor.

The average low-temperature elastic precursor (■) is the initial state for the ice VII segment of the 100 K Hugoniot. On both the low-temperature and temperate Hugoniots, shocks to the liquid water region ($\geq$ 6 GPa) overdrive the elastic precursor. This region on the Hugoniot (Figure 2.9, inset) is calculated with the liquid water $U_S - \Delta u_p$ EOS in Table 2.4 using the zero-pressure volume as the initial state. Note that the zero-pressure specific volume is off scale in the inset. The experimental technique used in this study does not reach shock pressures above 6 GPa, and no other low-temperature data in this pressure range are available. The T_0 = 100 K Hugoniot is derived assuming that the liquid region $U_S - \Delta u_p$ EOS (Table 2.4) is independent of initial temperature, as is the case in the ice VI and VII segments of the Hugoniot. Each segment of the Hugoniot is discussed in detail below.

2.4 Regions on the Solid Ice Hugoniot

2.4.1 Elastic Shock Precursors

The amplitude of the elastic shock precursor wave in solid ice at $T_0 \sim 263$ K falls between 0.05-0.30 GPa (Table 2.1). The elastic shock amplitudes measured at T_0 = 100 K are larger, reaching 0.35-0.62 GPa. Although commonly referred to as the Hugoniot Elastic Limit (HEL), implying a single value, the amplitude of the elastic precursor in solid ice varies over an order of magnitude. As noted by *Larson* [1984], the elastic precursor amplitude is correlated with the peak shock pressure. A similar peak shock pressure correlation is observed in SiO_2, where the elastic precursor amplitude is also dependent on the crystal orientation [*Fowles*, 1967]. However, *Larson* [1984] did not observe any dependence of the elastic precursor or final shock state on the crystal axis in temperate ice experiments.

Although *Larson* [1984] suggested that the amplitude of elastic shocks was controlled by the onset of (partial) melting, more recent work has shown that brittle failure is more likely. *Gaffney* [1985] argued that the energy deposited in elastic shocks is insufficient to initialize melting (see his Figure 9), and *Arakawa et al.* [2000] directly imaged a brittle failure wave generated by a decaying shock wave in a solid ice block at 263 K, with an initial peak pressure of about 10 GPa decaying to 0.03 GPa. *Arakawa et al.* [2000] also recovered an ice sample shocked to just above the HEL (0.3 GPa) and observed dense shear cracks spaced at 100's μm.

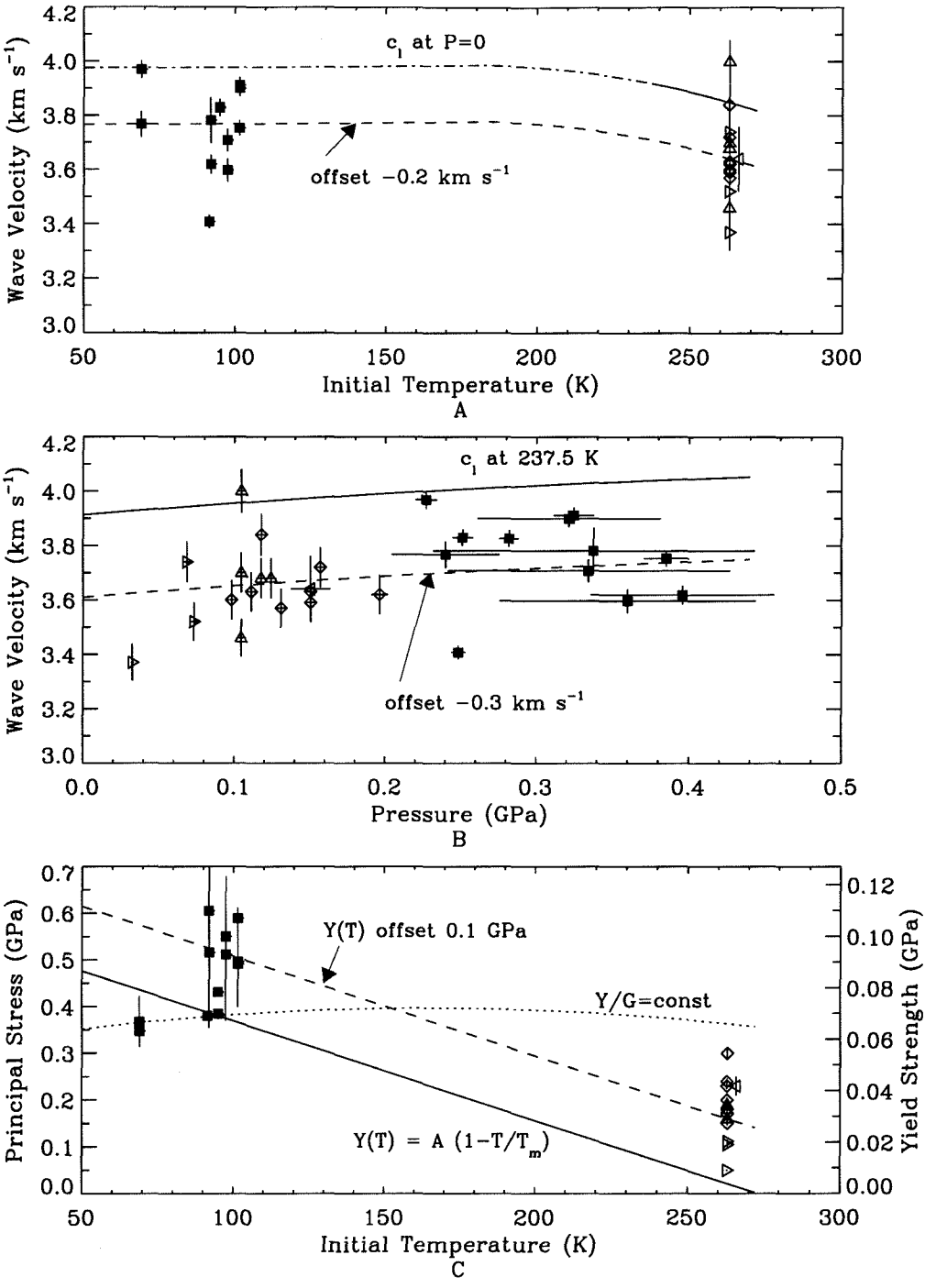

Figure 2.10: Properties of elastic shock precursor waves in solid ice with longitudinal sound velocity (c_l) in isotropic ice Ih. **A, B.** Ideal c_l dependence on temperature and pressure overestimates measurements by a constant offset in velocity. **C.** Two constitutive models for yield strength (Y), Y/G =constant (G is shear modulus) and Y proportional to homologous temperature. Symbols, shown with 1σ uncertainties, correspond to the data source (Table 2.1).

Figure 2.10 displays the properties of the elastic precursor waves. The scatter in the wave velocity is large in both the low-temperature and temperate ice (Figure 2.10A,B). Ideally, the elastic shock wave velocity is equal to the longitudinal sound speed, c_l. As *Larson* [1984] did not see an effect on crystal orientation, we use isotropic values for the elastic moduli. The temperature (at zero pressure) and pressure dependence (at 237.5 K) of the elastic constants were measured by *Gagnon et al.* [1988] and averaged for isotropic ice [*Voigt*, 1928; *Simmons and Wang*, 1971]. The temperature dependence observed by *Gagnon et al.* [1988] has been extrapolated below 237.5 K (dot-dashed line). The polynomial fits to the elastic constants presented by *Gagnon et al.* [1988] do not extrapolate well to low-temperatures (resulting in decreasing c_l with decreasing temperature), and we assume that the value of c_l asymptotically approaches a maximum, here given as the maximum in the extrapolated polynomial, at 3.97 km s^{-1}. The principal stress measurements of the elastic precursor σ_1 have been reduced to pressure P by

$$P = \frac{(\sigma_1 + 2\sigma_2)}{3} = \frac{1}{3}\left(\frac{1+\nu}{1-\nu}\right)\sigma_1, \tag{2.10}$$

where the perpendicular stresses $\sigma_2 = \sigma_3 = \nu\sigma_1/(1-\nu)$ under uniaxial strain, and $\nu = 0.325$ is the Poisson's ratio in ice Ih [*Petrenko and Whitworth*, 1999] (the small dependence of ν on temperature is neglected).

The elastic precursor wave velocities are systematically lower than ideal isotropic ice by 0.2-0.3 km s^{-1}. We speculate that the offset may be a result of imperfections in the ice samples, such as trace porosity. The elastic precursor wave velocities measured in samples prepared within a given study have a wide range of scatter, corresponding to the difficulty in making identical ice samples.

The amplitude of the elastic precursor, however, is strongly dependent on the initial temperature, as shown in Figure 2.10C. A similar temperature dependence has been observed in molybdenum (Mo) [*Duffy and Ahrens*, 1994]. In brittle materials, the Hugoniot Elastic Limit, σ_{HEL} has been related to the compressive yield strength, Y_0, by the Griffith yield criterion [*Rosenberg*, 1993], where

$$\sigma_{\mathrm{HEL}} = \frac{1-\nu}{(1-2\nu)^2} Y_0. \tag{2.11}$$

Duffy and Ahrens [1994] found that the temperature dependence of the yield strength in Mo

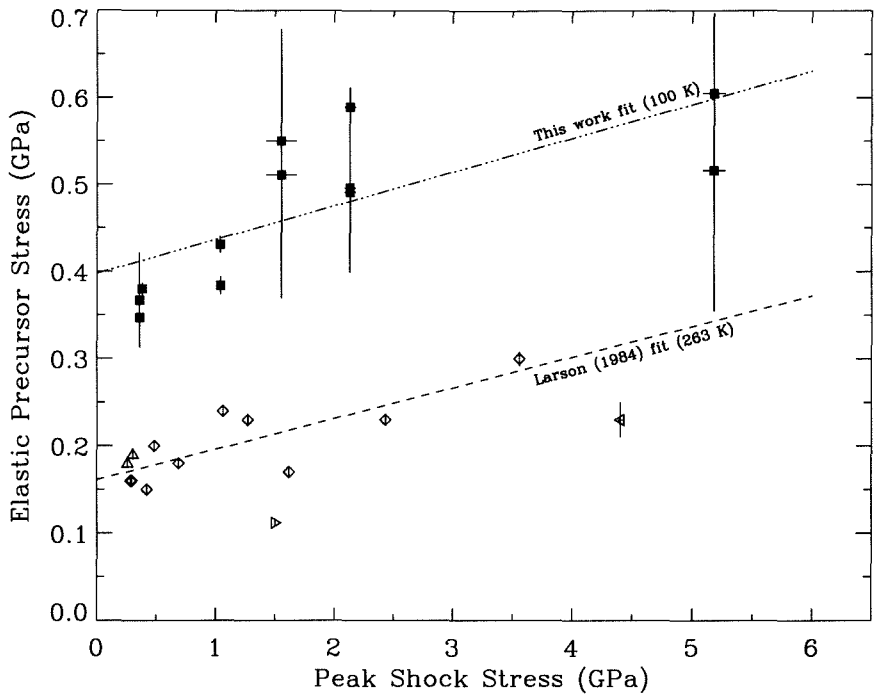

Figure 2.11: Model for peak shock stress-temperature dependence of the amplitude of the elastic shock precursor. Data from this work (■) obtained at initial temperatures $T_0 \sim 100$ K, and data with open symbols obtained at $T_0 \geq 263$ K.

lies between two constitutive models, one where the ratio Y/G is constant where G is the shear modulus, and one where the yield strength is a function of homologous temperature T/T_m,

$$Y_0 = A(1 - T/T_m) \tag{2.12}$$

where T_m is the melting temperature (in K) at zero pressure and A is a constant fit to the data. In ice, there is an additional dependence on the peak shock pressure (see below), which was not observed in Mo [*Duffy and Ahrens*, 1994].

If the yield strength is constrained to zero at the melting temperature and the lowest yield value at 100 K and 0.38 GPa, then $A = 0.1$ and Eq. 2.12 systematically underestimates the yield strength dependence on temperature (solid line in Figure 2.10C) by about 0.1 GPa. However, the slope of the fit agrees well with the data's dependence on initial temperature. The constant Y/G model (dotted line), fixed at the same point at 100 K and 0.38 GPa, does not have the correct slope to fit the data, where G is calculated from *Gagnon et al.* [1988].

Solid ice appears to have some dynamic strength at temperatures very close to melting. In addition, the amplitude of the elastic shock precursors is not single-valued at a given initial temperature, but also shows a dependence on the peak shock stress, shown in Figure 2.11. Linear fits of the dependence of the elastic precursor amplitude σ_E on the peak shock stress σ_S are given by

$$\sigma_E = \begin{cases} 0.398\ (\pm 0.029) + 0.039\ (\pm 0.012)\sigma_S, & \text{at } T \sim 100\ K \\ 0.161\ (\pm 0.010) + 0.035\ (\pm 0.007)\sigma_S, & \text{at } T \sim 263\ K. \end{cases} \tag{2.13}$$

These lines provide a good approximation of the peak shock stress dependence, although there is some indication, especially in the low-pressure data, that the amplitude of the elastic precursor approaches a limit, of about 0.55 GPa for $T_0 = 100$ K, and about 0.25 GPa when $T_0 = 263$ K. σ_E at intermediate temperatures may be estimated by interpolating between the existing data and using Eq. 2.12 with a 0.1 GPa constant offset (Figure 2.10C) and the Griffith yield criterion (Eq. 2.11).

The dynamic strength of ice falls significantly outside its static equilibrium stability field, shown in Figure 2.12. The elastic precursor data, where the principal stress measurements have been converted to pressure (Eq. 2.10), are plotted against the initial temperature because the elastic shock compression is essentially isothermal (see below). Increase in compressive and tensile strength in ice with strain rate is well established [*Hawkes and Mellor*, 1972; *Lange and Ahrens*, 1983; *Stewart and Ahrens*, 1999]. Given the strong temperature and strain rate dependence on the static strength of ice [also see, *Durham et al.*, 1998; *Durham and Stern*, 2001], it is not surprising that the dynamic strength of ice shows dependence on both the temperature and peak shock stress (a proxy for strain rate [*Swegle and Grady*, 1985]).

The comparison of the elastic precursor data with the static phase diagram led *Larson* [1984] to infer that the amplitude of the elastic precursor was limited by melting, but more recent work indicates that ice undergoes brittle failure (described above). The mechanism for brittle failure in a shock may be related to a phenomena called transformational faulting. *Durham et al.* [1983, 1998] found that, under confined conditions at 77 K, ice Ih fails from "stress interaction of ice II microinclusions under high shear stress." The maximum differential stress at failure becomes constant with increasing confining pressure at a value of about 0.165 GPa. Laboratory shock wave experiments, in uniaxial strain, support shear

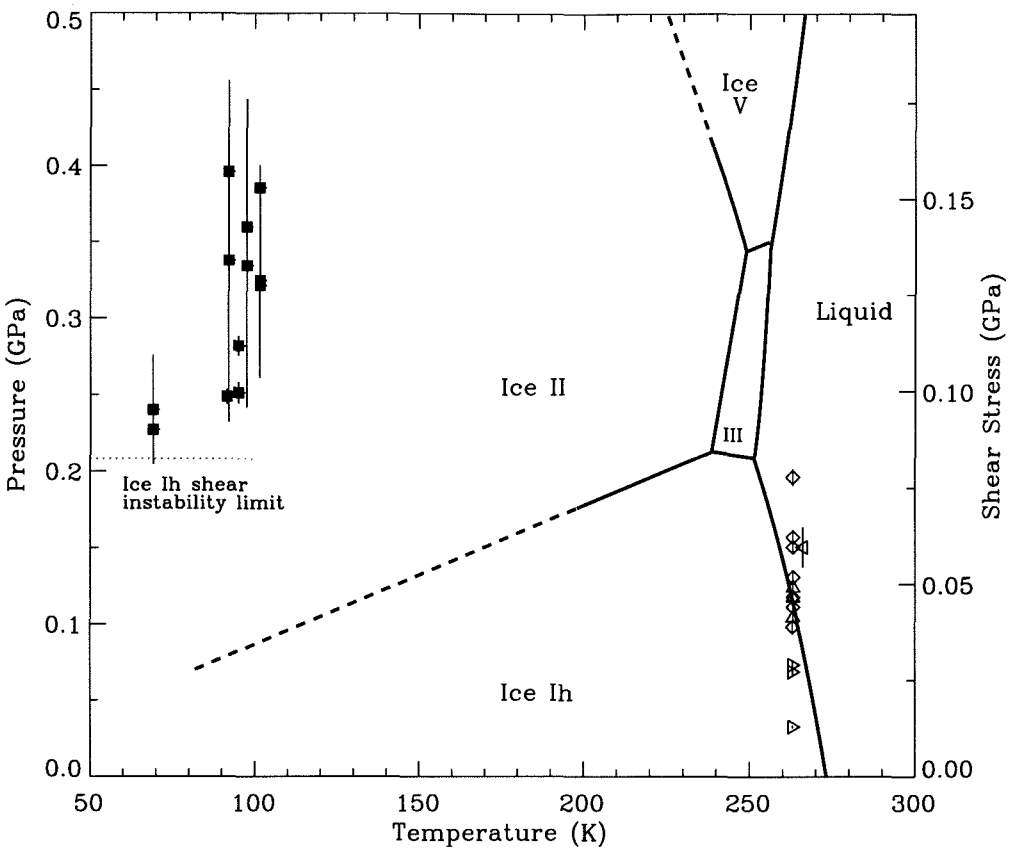

Figure 2.12: Elastic shock precursor data (with principal stress reduced to pressure) and ice $P-T$ phase diagram with shear stress under uniaxial strain on right vertical axis. Static compressive strength at 77 K limited to shear stresses of 0.08 GPa by transformational faulting where ice II nucleates in shear stress concentrations [*Durham et al.*, 1998]. Dynamic strength may also be limited by transformational faulting to ice II (for $\leq$ 100 K) and liquid water (at $T \sim 263$ K).

stress until material failure. The shear stress, τ, is given by

$$\tau = (\sigma_1 - \sigma_2)/2, \tag{2.14}$$

where $\tau = 0.26\sigma_1$ in ice under uniaxial strain. The elastic precursor amplitude appears to approach a limiting value with increasing shock stress (Figure 2.11), and the limiting mechanism could also be transformational faulting. The strain rates in a shock, with $10^3 - 10^4$ s^{-1}, are much higher than the static experiments, with $10^{-7} - 10^{-4}$ s^{-1}, and a larger limiting shear stress is likely because of the dependence of strength on strain rate [c.f., *Lange and Ahrens*, 1983; *Stewart and Ahrens*, 1999]. The brittle failure mechanism at

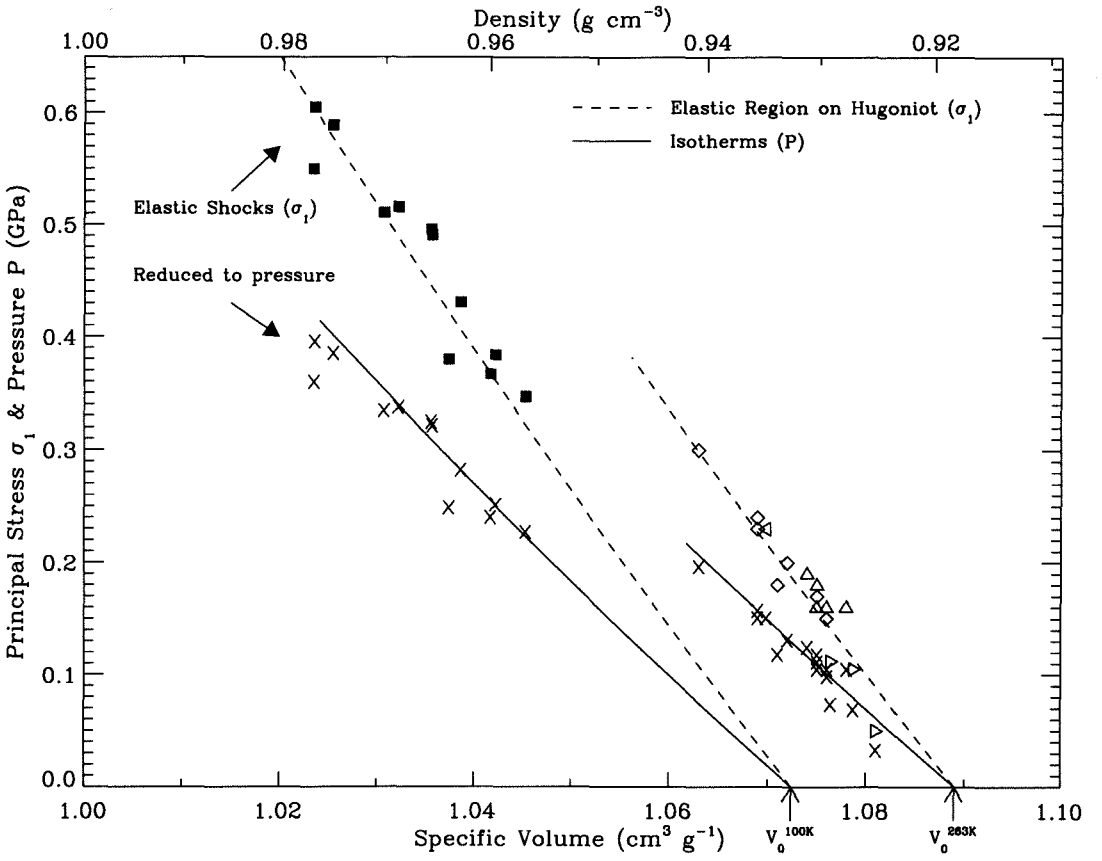

Figure 2.13: Elastic precursor data (σ_1) and elastic region on 100 and 263 K solid ice Hugoniots (dashed lines). Elastic precursor data, reduced to pressure (Eq. 2.10), agrees well with isothermal compression curves.

263 K may also be transformational faulting, although the microinclusions in the shear zones would be consistent with liquid water. Examination of the shear failure bands after a shock experiment, where the samples are recovered and maintained at liquid nitrogen temperatures, may help determine whether transformational faulting is the shock failure mechanism in ice.

The elastic region on the 100 and 263 K Hugoniots (dashed lines in Figure 2.13) are derived from the $U_S - \Delta u_p$ EOS (Table 2.4) and the RH equations. The elastic precursor principal stress data is reduced to pressure ($\times$) using Eq. 2.10 and compared 100 and 263 K isotherms (solid lines), which are derived below.

Using the $U_S - \Delta u_p$ fits in Table 2.4, the intercept of the elastic segment defines the mean longitudinal wave speed in the ice shock data, $c_l = 3610$ m s^{-1}, and the intercept of

the ice Ih deformation shock segment defines the mean bulk wave speed, $c_b = 3000$ m s^{-1}. The inferred bulk modulus is 8.4 and 8.3 GPa at 100 and 263 K, respectively.

Assuming that the second derivative of the bulk modulus is negligible over this pressure range, the $U_S - \Delta u_p$ fit for the ice Ih deformation shocks is used to constrain the first derivative of the isothermal bulk modulus K_T' [e.g., *Ruoff*, 1967; *Jeanloz*, 1989]. The slope, s, of the linear $U_S - \Delta u_p$ fit is related to K_T' by

$$K_T' = 4s - 1, \tag{2.15}$$

where $K_T' = 3.0^{+3.2}_{-3.0}$ for $s = 1.00 \pm 0.8$ (Table 2.4). We use the Murnaghan equation for isothermal compression [*Murnaghan*, 1944; *Jeanloz*, 1989], given by

$$P_T = \frac{K_{T0}}{K_T'} \left[\left(\frac{V_0}{V} \right)^{K_T'} - 1 \right]. \tag{2.16}$$

Because the shock data in the ice Ih phase covers a small range of pressures, isothermal compression curves which agree with the data are not very sensitive to the values of K_{T0} and K_T'. The inferred values for K_{T0} and K_T', derived here under uniaxial strain conditions, are in good agreement with bulk static values [*Hobbs*, 1974; *Petrenko and Whitworth*, 1999].

From the agreement between the elastic shock pressure ($\times$, Figure 2.13) and the hydrostatic isotherms, we conclude that the temperature increase in the elastic shock precursor is negligible.

2.4.2 Ice Ih Shocks

The present low-temperature ice shock experiments record the first steady deformation shock waves in the ice Ih structure. The steady ice Ih shocks are observed as the second wave in a three-wave shock front, composed of an elastic shock precursor, deformation shock in the ice Ih structure, and transformation shock to ice VI (refer to Appendix A, shots #1043, 1046, 1047, also see Figure 2.7). The amplitude of the intermediate ice Ih shock appears to be dependent on the peak shock stress up to a limiting pressure of 1.16 GPa. At this point a cusp forms on the ice Hugoniot, similar to the 13 GPa cusp observed on the iron Hugoniot, derived from three-wave shock profiles corresponding to the HEL, α deformation shock, and $\alpha \rightarrow \epsilon$ transformation shock [*Minshall*, 1955; *Bancroft et al.*, 1956; *Loree et al.*,

1965]. Also, a cusp at 19.4 GPa on the aluminum nitride (AlN) Hugoniot corresponds to the B4-B1 transformation, and similar three-wave shock profiles are observed [*Mashimo et al.*, 1999]. Recent work on the SiO_2 Hugoniot indicate that a similar cusp may exist near 23 GPa, between the α-quartz to stishovite phase transformation [*Zhugin*, 1995; *Zhugin et al.*, 1994].

In our experiments with peak stresses in the range 0.4-0.5 GPa, a steady ice Ih shock wave does not develop. The elastic precursor is followed by a decaying ice Ih deformation wave. Previously published ice data at $T_0 = 263$ K also show decaying ice Ih shock waves; for example refer to Figure 4 in *Larson* [1984] with peak stress of 0.295 GPa. The decaying shock data have been reported, erroneously, as Hugoniot states. Larson's deformation shock data with peak stress < 0.6 GPa have not been considered in the derivation of the solid ice Hugoniot presented here.

In addition, the studies by *Gaffney and Smith* [1994] and *Davies and Smith* [1994] at 263 K do not yield information on the ice Ih deformation shock region of the ice Hugoniot, although some three-wave shock profiles were recorded. These experiments used embedded stress gauges and suffered from difficulties related to the impedance mismatch between the gauges and ice. As steady wave profiles were not generated, the data cannot be used to determine Hugoniot states. Hence, previous researchers were unable to identify the intermediate shock as a deformation shock in the ice Ih structure.

Therefore, the only steady ice Ih deformation shock Hugoniot measurements have been obtained at $T_0 = 100$ K and only in cases when the wave is supported by a subsequent transformation wave to ice VI. These data (★) are shown in Figure 2.14 with the elastic and ice Ih deformation shock regions on the 100 K ice Hugoniot (dashed lines). The ice Ih deformation shock region on the $T_0 = 100$ K solid ice Hugoniot is bound by the mean elastic precursor, about 0.5 GPa, and the ice Ih deformation shock cusp at 1.16 GPa. On the 263 K Hugoniot, the ice Ih deformation shock region is bound by the average elastic precursor stress of 0.2 GPa and the onset of transformation to ice VI at stresses above 0.6 GPa (dashed line, Figure 2.9).

Ideally, after brittle failure upon passage of the elastic shock precursor wave, the ice will respond hydrodynamically. The elastic shock precursor supports shear stress, and the measured principal stress must be corrected to pressure (Eq. 2.10, Figure 2.13). The principal stress measured in the ice Ih deformation shock states, however, approach the

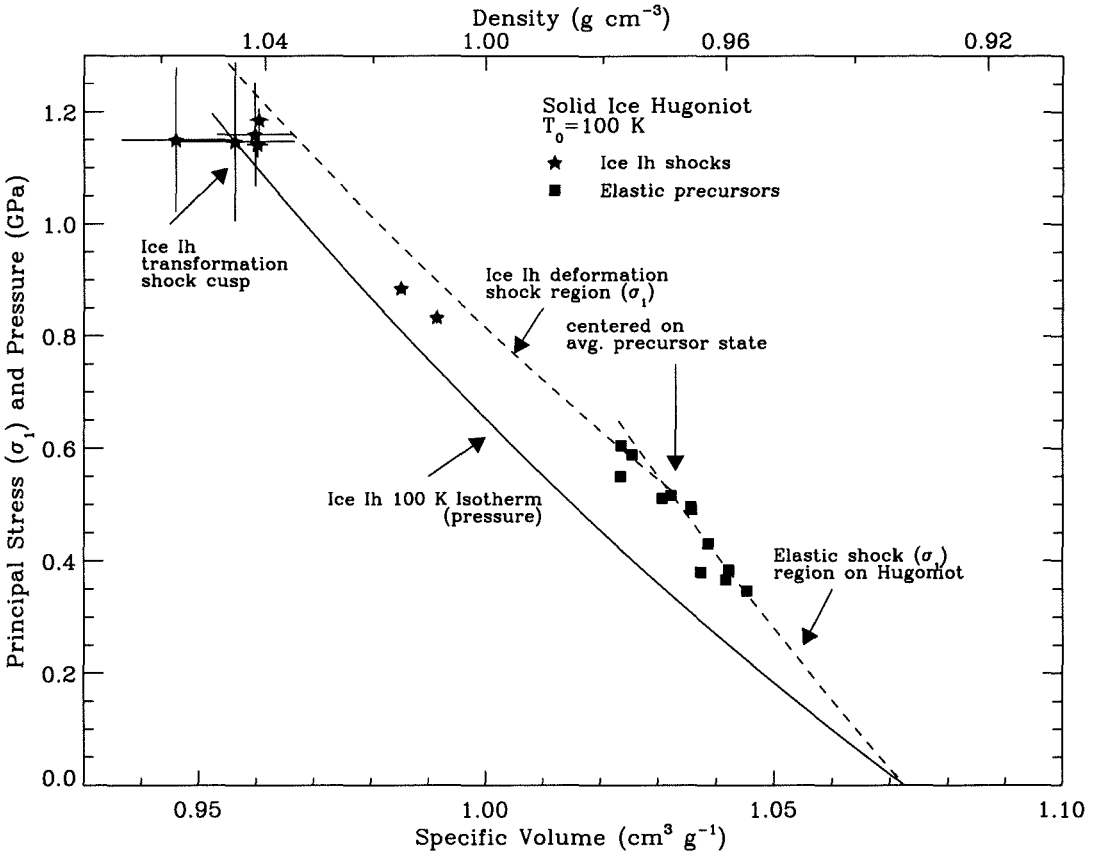

Figure 2.14: Elastic and Ice Ih deformation shock regions on 100 K solid ice Hugoniot (dashed lines). Ice Ih deformation shocks (★) have a limiting value of 1.2 GPa, forming a cusp on the Hugoniot. Principal stress on the Hugoniot approaches isothermal compression curve (solid line) indicating loss of strength on the Hugoniot and little shock heating.

hydrodynamic isotherm (solid line in Figure 2.14, derived in previous section). Thus, we infer that loss of shear strength is complete in shock states with principal stresses $\geq$ 1.16 GPa (also see section 2.6). Similar convergence of the Hugoniot and isotherm at pressures just above the elastic limit is observed in other materials, including SiO_2 [*Fowles*, 1967] and AlN [*Rosenberg et al.*, 1991]. In the phase transformation regions of the Hugoniot (2-5), we infer that the ice behaves hydrodynamically and may use principal stress and pressure interchangeably.

The difficulty in development of a steady ice Ih deformation shock may be related to the failure mechanism in the elastic precursor. At shock pressures just above the elastic limit, the decaying shock wave propagates with an initial velocity less than the bulk sound speed in ice. All ice Ih deformation shocks, steady and non-steady, have thick shock fronts,

rather than a sharp discontinuity (see Figure 2.4, Appendix A). The same phenomena is observed in AlN, where just above the HEL, the shock velocity is slower than the bulk sound speed and the wave profile is described as plastic [*Mashimo et al.*, 1999; *Rosenberg et al.*, 1991]. *Mashimo et al.* [1999] note that slip systems along macroscopic cracks may control brittle failure in AlN. If the failure mode increases heterogeneity in the material, e.g., by transformation faulting in shear bands (described in previous section), the low-amplitude planar shock wave following the elastic precursor may encounter a highly scattering material, which results in thickening of the shock front and decay in amplitude with propagation.

All the ice Ih deformation shocks, steady and non-steady, fall well outside the equilibrium phase boundary. The deformation shock follows an elastic shock wave with amplitude comparable to or larger than the pressure along the equilibrium phase boundary (Figure 2.12). The close agreement between the steady ice Ih deformation shocks observed in this study and the 100 K isotherm, which is nearly isentropic over this small pressure range, indicates that the entropy increase in the shock is not large enough to initiate melting of ice Ih.

The 100 and 263 K ice Hugoniots are shown in pressure-entropy ($P - S$) space, as solid and dashed lines in Figure 2.15, respectively, with a partial phase diagram of H_2O, including the H_2O phases observed in shock processes. The zero-pressure entropy, S_0, of ice Ih is about 890 and 2100 J kg^{-1} K^{-1} at 100 and 263 K, calculated from the specific heat capacity at constant pressure [*Giauque and Stout*, 1936] and the zero point entropy of ice Ih [*Petrenko and Whitworth*, 1999]. The critical entropies for incipient (IM) and complete (CM) melting at the triple point are 2290 and 3510 J kg^{-1} K^{-1} [*Petrenko and Whitworth*, 1999]. The phase boundaries are constructed from latent heat and volume change measurements [Bridgman's data compiled in *Dorsey*, 1940] and the equations of state for ices VI and VII presented below. The shock-induced phase transformation regions (3-5) on the Hugoniot are described below.

The quasi-isentropic compression in the elastic shock and ice Ih deformation shock segments (regions 1 and 2) on the 100 K Hugoniot is shown as the vertical segment with $P < 1.2$ GPa based at $S_0^{100\ K}$. In the $P - S$ diagram, it is obvious that, at 100 K, the failure mode in the elastic precursor does not involve liquid water. On the sub-microsecond time scales of a shock, the ice Ih structure may be driven far outside of its static stability field by a steady deformation shock before shock-induced transformation to ice VI. For $T_0 = 263$ K, however, Hugoniot regions 1 and 2 ($P < 0.6$ GPa) enter the mixed solid-liquid

phase boundary (also see Figure 2.12), and steady ice Ih deformation shock waves are not observed. We also note that under quasi-isentropic compression, the 263 K Hugoniot, plotted in $P-T$ space, cannot enter the liquid water stability field at pressures just above the elastic limit as suggested by *Larson* [1984] in his Figure 8 (also see section 2.5).

2.4.3 Ice VI

The shock-induced phase transformation to ice VI has been previously identified by *Larson* [1984] from the large volume compression on the Hugoniot, $> 30\%$, at pressures above 0.6 GPa (Figure 2.9). On the 263 K Hugoniot, the transition to the ice VI region is clearly associated with the equilibrium phase boundary of ice VI near 0.63 GPa (Figures 2.9 and 2.1).

An unusual feature of the $T_0 = 100$ K Hugoniot is that the volume on the Hugoniot over the pressure range 0.6-1.2 GPa is not single valued. This pressure range corresponds to the regions of ice Ih deformation shocks and ice VI transformation shocks on the Hugoniot. The degenerate Hugoniot region is illustrated by the two possible locus of shock states, labeled A and B in Figure 2.9. The A locus corresponds to peak shock states > 1.16 GPa which pass through the ice Ih shock cusp. The B locus is centered at the ice Ih shock state observed in shot #1046, 0.85 GPa, where the peak shock stress was 1.03 GPa (see Appendix A).

This kind of degeneracy of peak shock stress is not seen in other materials. The cause of this complicated shock response in ice seems to be related to the strain rate in the shock front. As described in the previous sections, the amplitude of the elastic precursor and the ice Ih deformation shock seems to be dependent on the final shock stress. The strain rate in the shock front is proportional to the peak stress [*Swegle and Grady*, 1985]. Strong shocks drive larger amplitude elastic precursors and ice Ih deformation shocks before the final transformation shock to ice VI. Peak shock stresses just above the phase boundary, ~ 6 GPa, drive lower-amplitude precursor shock waves. The observed steady ice Ih transformation shocks are not strictly a member of the possible end states described by a Hugoniot, as they are only observed as intermediate waves in multiple-wave shock fronts. We include these states on the Hugoniot because they are necessary to accurately describe the shock front in ice.

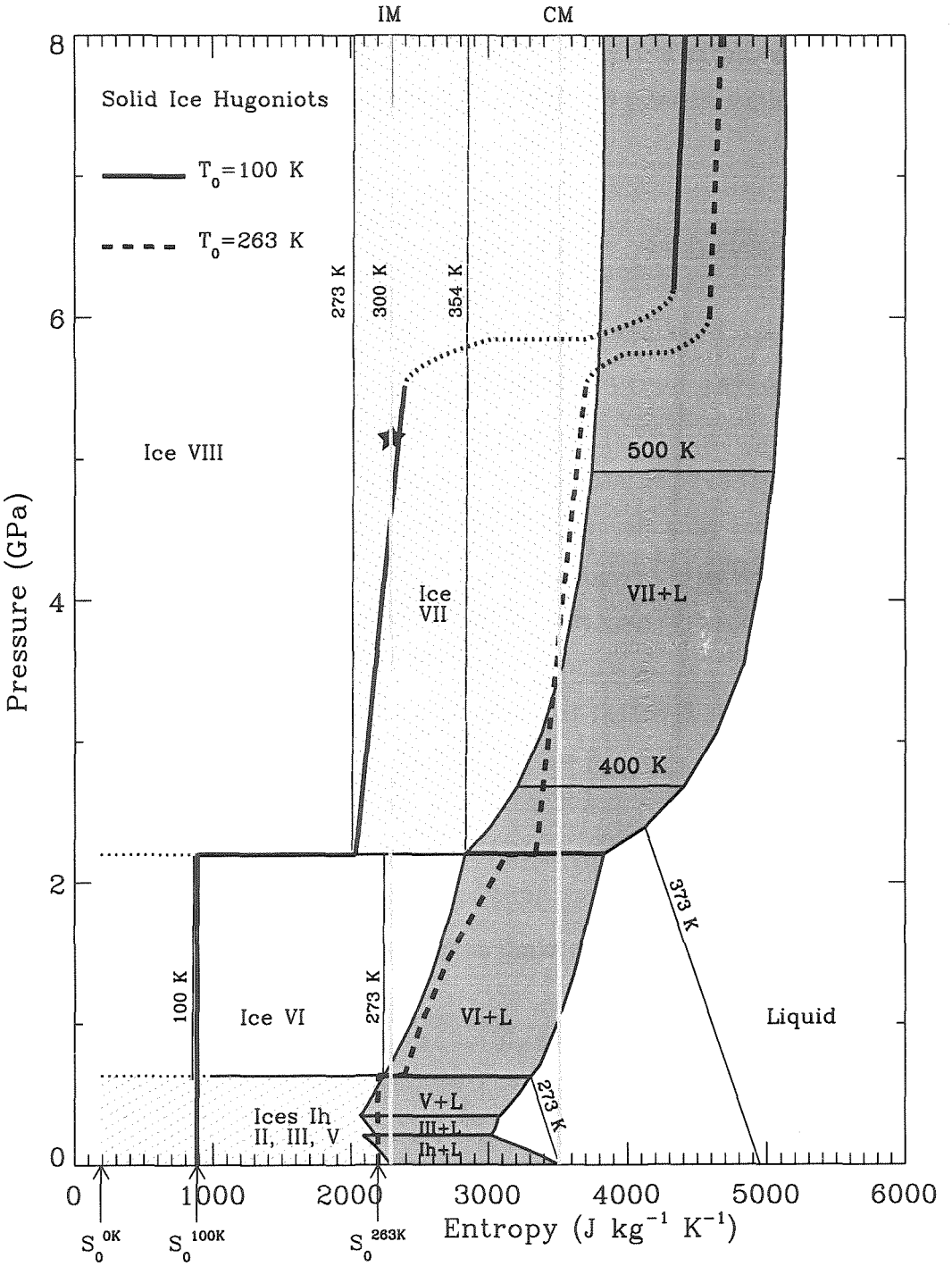

Figure 2.15: 100 and 263 K Ice Hugoniots and partial H_2O phase diagram in pressure-entropy space. IM and CM denote critical entropies for incipient and complete melting upon release to zero pressure.

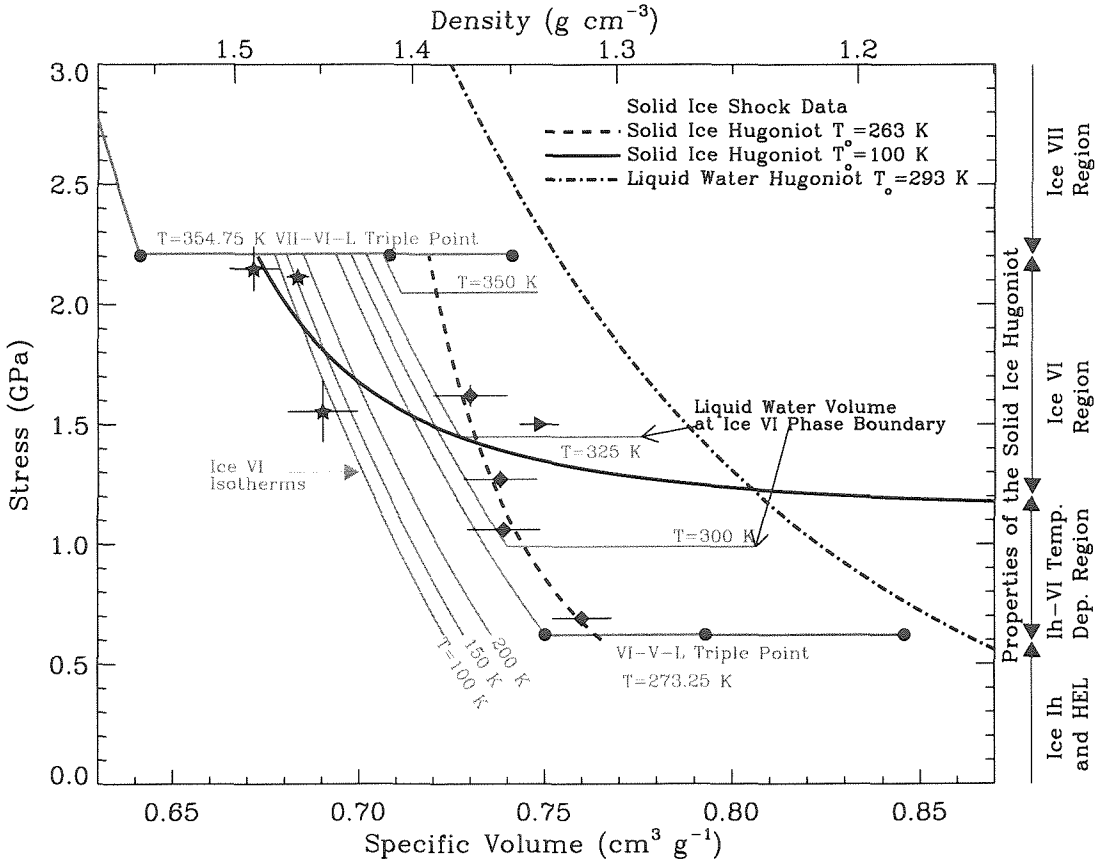

Figure 2.16: Ice VI region of solid ice Hugoniot (Fig. 2.9) and ice VI isotherms with ice VII, liquid water, and ice V equilibrium phase boundaries. VII-VI-L and VI-V-L triple points (●) indicate volume differences between phases. Ice VI isotherms extend to liquid water phase boundary volume (horizontal segments). For $T_0 = 263$ K, incomplete transformation to ice VI occurs along Hugoniot (dashed line, ◆ ▶) that lies in liquid water-ice VI co-existence region. For $T_0 = 100$ K, data (★) are consistent with pure ice VI.

Table 2.5. Triple points of stable H_2O ice phases.

Triple Points†	P (GPa)	T (°C)
L-Ih-III	0.209	-22.3
L-III-V	0.350	-17.5
L-V-VI	0.632	0.1
L-VI-VII	2.210	81.6
Ih-II-III	0.213	-34.7
II-III-V	0.344	-24.3
VI-VII-VIII	2.100	~ 0
Ih-XI-vap.	0	-201

†From *Petrenko and Whitworth* [1999]. Ice II-V-VI not measured.

Table 2.6. Selected properties of stable ice phases.

Phase	ρ_0 (g cm^{-3})	K_{T0} (GPa)	$K' = \mathrm{d}K_T/\mathrm{d}P$	T_0 (K)
Ih*	0.93	8.4	1.0	100
II	1.18	14.6	...	238
III	1.15	9.7	...	246
V	1.24	13.9	...	238
VI‡	1.30	13.08	6.8	238
VII†	1.47	23.9	4.2	300
VIII	1.56	...	...	...
X	2.51	...	...	...

Parameters used in constructing reference isotherms. If no reference given, properties from *Sotin et al.* [1998].

*K_{T0}, K' derived from shock data, see text.

‡K_{T0}, K' from *Tulk et al.* [1997].

†K_{T0}, K' from *Fei et al.* [1993].

The shock data are shown together with ice VI isotherms and the ice VI-liquid water phase boundary in Figure 2.16. The triple points, VI-V-L and VII-VI-L, are horizontal lines in $P - V$ space where the ● denotes the volume for each phase (also see Table 2.5). The ice II and VIII phase boundaries are not shown.

Isotherms are constructed using the formulation presented by *Fei et al.* [1993]. From a reference isotherm (T_{ref}) and model for the volume thermal expansion coefficient, α. An isotherm at T is given by

$$V(P,T) = V(P,T_{ref}) \left[\exp \left(\int_{T_{ref}}^{T} \alpha(P,T) \mathrm{d}T \right) \right]_P . \tag{2.17}$$

We use the 230 K isotherm for ice VI as the reference (Table 2.6). The thermal expansion coefficient has been measured at 1.054 GPa between 0-200 K by *Mishima et al.* [1979], showing a nearly constant value of $\alpha = 10^{-5}$ between 140-200 K. Without measurements at different pressures, we estimate α for ice VI with the same formulation as *Fei et al.* [1993] for ice VII:

$$\alpha(P,T) = \alpha_0(T) \left(1 + \frac{K'_{T0}}{K_{T0}} P \right)^{-\eta} , \text{ where} \tag{2.18}$$

$$\alpha_0(T) = a_0 + a_1 T. \tag{2.19}$$

$\alpha_0(T)$ is the zero-pressure thermal expansion coefficient. The variables derived by *Fei et al.* [1993] for ice VII agree well with the limited ice VI data and the phase boundary volumes are consistent with measurements reported in *Dorsey* [1940]. The thermal expansion values used for both ice VI and VII are $a_0 = -3.9 \times 10^{-4}$, $a_1 = 1.5 \times 10^{-6}$ K^{-1}, and $\eta = 0.9$.

In Figure 2.16, the volume differences at the ice VI-liquid water phase boundary and triple points are taken from dV measurements reported in *Dorsey* [1940]. The shock measurements with $T_0 = 263$ K (◆ ▶) do not fall in the ice VI stability field, but lie within the ice VI-liquid water phase boundary, indicating incomplete transformation to ice VI on the Hugoniot (dashed line). Thus, the ice VI region along the $T_0 = 263$ K Hugoniot is composed of a mixture of liquid water and ice VI.

This result, derived from the phase diagram in $P - V$ space, is consistent with the $P - S$ diagram (Figure 2.15). At the same temperature, the entropy (S) difference between ice Ih and VI is small. Note that entropy along the 100 and 273 K isotherms in the ice VI field extrapolate to zero pressure at values very close to the ice Ih entropies at the same temperature.

Shock-induced phase transformations do irreversible work on the ice, and entropy must increase along the Hugoniot. At $T_0 = 263$ K, the zero-pressure entropy ($S_0^{263\ \mathrm{K}} = 2100$ J kg^{-1} K^{-1}) is near incipient melting at the base of the ice VI field (0.63 GPa). Therefore, the entropy along the Hugoniot enters the entropy gap between the ice VI and liquid water stability fields (Figure 2.15).

We infer from the $P - V$ diagram that the shock does not increase in entropy enough to complete the transformation to liquid water (Figure 2.16). The entropy along the ice VI region of the 263 K Hugoniot, shown in Figure 2.15, is estimated by the mass fraction of liquid and ice VI derived from the volume of the shocked state. The temperature along the Hugoniot will follow the equilibrium phase boundary, as the temperature increase from the shock will be buffered by partial melting (also see section 2.5).

In Figure 2.16, the volume of the $T_0 = 100$ K data (★) are consistent with pure ice VI in the shock state. In addition, the data lie between the 100-150 K ice VI isotherms. If the shock state is in thermal equilibrium, we infer that the temperature increase along the 100 K Hugoniot is less than 50 K in this pressure range.

The Hugoniot derived from the ice VI $U_s - \Delta u_p$ EOS (solid line A in Figure 2.9), however, crosses the ice VI isotherms with negative dT/dP which is not consistent with a pure phase

transformation, as entropy and temperature should increase along the Hugoniot. But this region on the 100 K Hugoniot is multi-valued, and the final shock states in the ice VI region are reached through intermediate ice Ih shocks of different amplitude (e.g., solid lines A and B in Figure 2.9). The limited data in this region indicate that the end states will not violate $dT/dP > 0$. Therefore, our interpretation of a pure ice VI phase along the 100 K Hugoniot is consistent with the data. In $P - S$ space, the 100 K Hugoniot is approximated by following the 100 K isotherm in the ice VI field.

Larson [1984] described the ice VI region of the 263 K Hugoniot as a pure ice VI state by comparing the Hugoniot compression to a 263 K isotherm (see his Figure 8). We have shown that this region must be a mixture of ice VI and liquid water. At lower initial temperatures, however, it is possible to form pure ice VI in a shock.

2.4.4 Ice VII

Above 2.2 GPa, in the ice VII region, the Hugoniot is more compressible compared to the ice VI region (Figure 2.9), and the $U_s - \Delta u_p$ EOS have different slopes (see Tables 2.4 and 2.6). The shock data between 2.2-20 GPa are shown together with ice VII isotherms and the ice VII-liquid water phase boundary in Figure 2.17. The ice VIII phase boundaries are not shown, and ice VII isotherms have been extrapolated out of the equilibrium field to lower temperatures (see Figure 2.1, and discussion below).

The $P-V-T$ equation of state for ice VII has been well defined in our region of interest by *Fei et al.* [1993]. We use the reference isotherm at $T_{ref} = 300$ K, refer to Table 2.6, and the thermal expansion model presented in the previous section. In Figure 2.17, the volume difference at the liquid water phase boundary is taken from *Dorsey* [1940] and linearly extrapolated outside the measured range.

Between 2.2-5.5 GPa, in the region described by the ice VII $U_S - \Delta u_p$ EOS, the $T_0 =$ 263 K shock data (◆ ◀) lie in or near the ice VII and liquid water phase boundary, indicating that this region on the Hugoniot is also composed of a mixture of phases. The ★ data lie well within the ice VII stability field, consistent with pure ice VII on the 100 K Hugoniot. Both the 100 K and 263 K Hugoniots have slightly negative dT/dP between 2.2 and 5.5 GPa, indicating that there may be incomplete transformation to ice VII.

Along the 263 K Hugoniot, the shock data appear to cross from a mixture of ice VII and liquid water to pure ice VII. Examination of the $P-S$ diagram indicates that this is possible

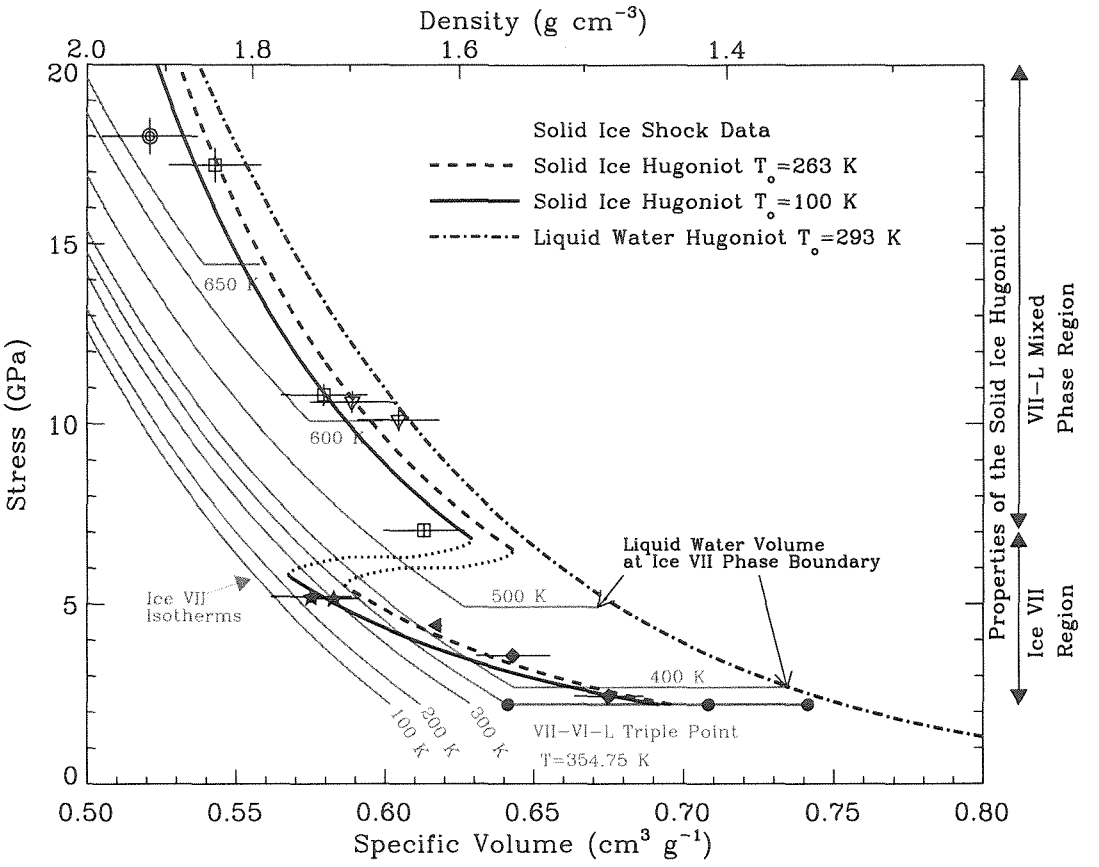

Figure 2.17: Ice VII region of the solid ice Hugoniot (Fig. 2.9) and ice VII isotherms with ice VI and liquid water equilibrium phase boundaries. VII-VI-L triple point (●) indicates volume differences between phases and ice VII isotherms extend to liquid water phase boundary volume (horizontal segments). ★ data from $T_0 = 100$ K; all other symbols from $T_0 = 263$ K.

with a small entropy increase along the Hugoniot, less than about 350 J kg^{-1} K^{-1} between 2.2 and 5.5 GPa (dashed line). On the 263 K Hugoniot, the entropy increase from 0 to 2.2 GPa is about 1100 J kg^{-1} K^{-1}, where the entropy at 2.2 GPa is constrained by the approximate 50-50% mixture of ice VII and liquid water implied by the volume along the Hugoniot (Figure 2.16). The $P - S$ Hugoniot is shown as a straight line in this region, although it is probably slightly concave down, as in the ice VI region.

For both $T_0 = 100$ and 263 K, shock-induced transformation to ice VII involves two-wave shock fronts, an elastic precursor and the transformation wave. The entropy deposited by ice VII transformation shocks from 100 K should be nearly the same as from 263 K, as the amount of irreversible work deposited by the shock is similar (Figure 2.9). Slight

differences include the initial and final volumes and the higher amplitude elastic precursor at low temperatures, slightly decreasing the entropy deposited by the transformation shock. The 100 K Hugoniot is shown in the $P - S$ diagram (Figure 2.15) with the same entropy increase at the base of the ice VII region, 1100 J kg^{-1} K^{-1}, and the same slope as on the 263 K Hugoniot. This construction of the ice VII region of the 100 K Hugoniot is in excellent agreement with the only data point at 5.2 GPa (★). The ★ data lie on the 300 K isotherm in Figure 2.17, which, assuming thermal equilibrium, constrains the entropy at this point. More data at low temperatures are necessary to constrain the $\mathrm{d}S/\mathrm{d}P$ along the Hugoniot.

The discontinuity (dotted lines, Figures 2.15 and 2.17) along the Hugoniot between 5.5-6 GPa corresponds to shock waves traveling near the longitudinal wave speed, which have previously been confused with the elastic precursor. Below the discontinuity, the Hugoniot is described by the ice VII $U_S - \Delta u_p$ EOS and, above it, the liquid water $U_S - \Delta u_p$ EOS given in Table 2.4.

2.4.5 Liquid Water

At shock pressures above 6 GPa (Figure 2.9), the elastic precursor is overdriven and the data follow a single $U_S - \Delta u_p$ EOS (Figure 2.8, Table 2.4). Figure 2.18 presents the ice shock data above 6 GPa together with ice VII isotherms up to 800 K and the ice VII-liquid water phase boundary. The liquid water Hugoniot centered at $T_0 = 298$ K is also shown (dot-dash line). Along the liquid water region of the ice Hugoniot, the offset between $T_0 = 100$ and 263 K is dominated by the difference in initial volume. The data between 6-20 GPa are consistent with a mixture of ice VII and liquid water along the Hugoniot. Shock-induced transformation to pure liquid water is complete above 20 GPa.

Therefore, in $P - S$ phase diagram, the liquid water region of both the 100 and 263 K Hugoniots fall within the entropy gap between ice VII and liquid water. The Hugoniots will cross into the liquid water stability field above about 20 GPa.

Between 25-35 GPa, both ice Hugoniots cross the liquid water Hugoniot. The larger initial volume of ice Ih results in more irreversible work upon dynamic compression of ice compared to liquid water. The larger internal energy deposited from the irreversible work on ice results in higher shock temperatures compared to liquid water.

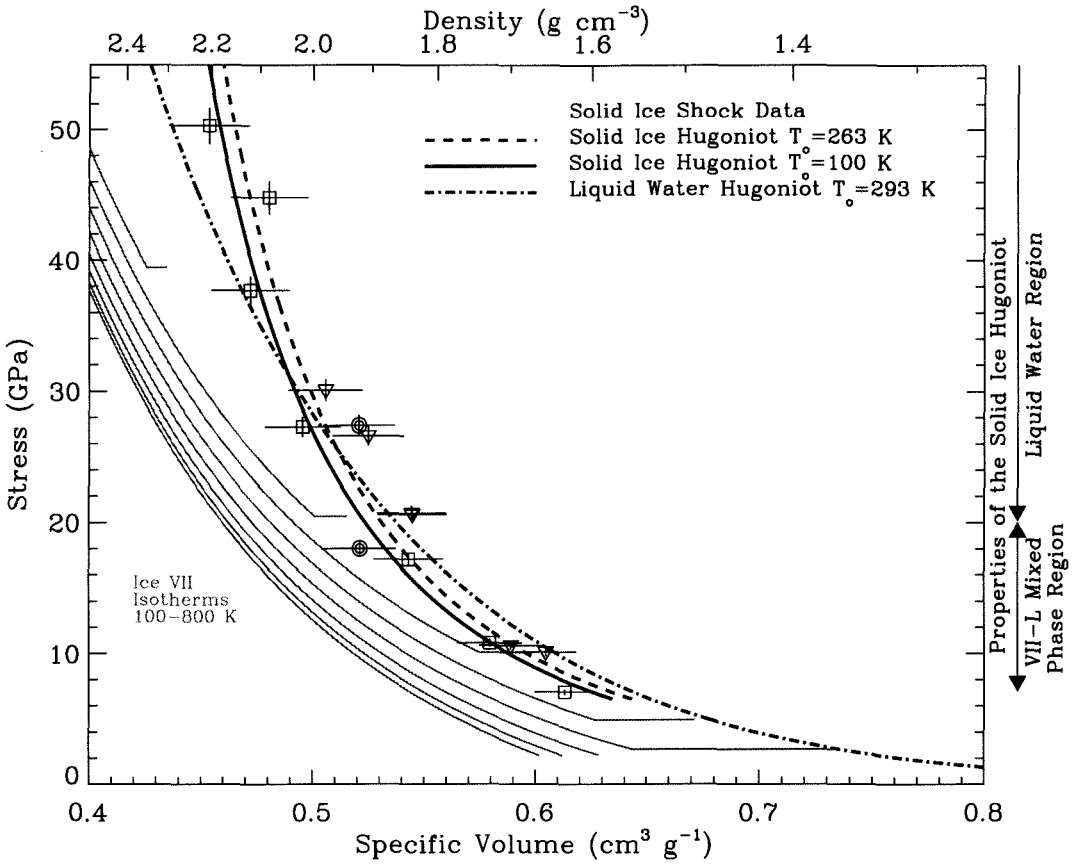

Figure 2.18: Liquid water region of solid ice Hugoniot (Fig. 2.9) and ice VII isotherms extended to liquid water phase boundary volume (horizontal segments). All shock data obtained from $T_0 = 263$ K.

2.5 Shock Temperatures

Based on our analysis of the regions of the solid ice Hugoniot, theoretical temperatures achieved along the Hugoniot are shown in the $P - T$ phase diagram (Figure 2.19). The different $U_s - \Delta u_p$ EOS regions on the Hugoniot are shown as hatched and dotted areas. The room temperature liquid water Hugoniot temperatures are derived from published data [*Rice and Walsh*, 1957; *Walsh and Rice*, 1957; *Kormer*, 1968; *Lyzenga et al.*, 1982]. As mentioned in *Rice and Walsh* [1957], the water Hugoniot intersects the ice VII phase boundary near 3-4 GPa, which is also seen in the $P - V$ phase diagram in Figure 2.17. The strength effects and phase transformations make a theoretical derivation of the shock temperatures on the solid ice Hugoniot difficult, and methods developed for hydrodynamic materials [e.g., *Rice and Walsh*, 1957] are not directly applicable.

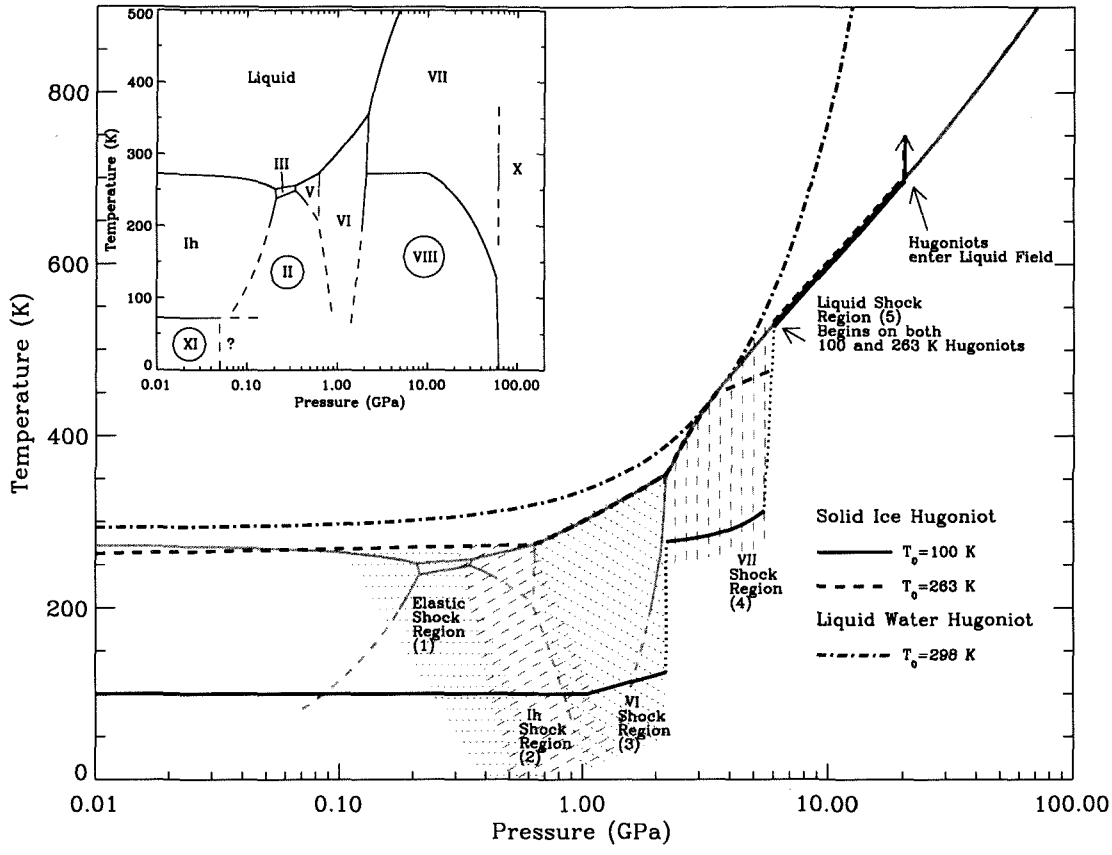

Figure 2.19: H_2O phase diagram with solid ice (100 and 263 K) and liquid water (298 K) Hugoniots. Note pressure scale is logarithmic for detail in low-pressure phases. Different regions (Table 2.4) on solid ice Hugoniot are noted by the dotted and dashed areas. Inset displays expanded phase diagram with circled proton-ordered ice phases.

As described in sections 2.4.1 and 2.4.2, the compression by elastic shocks and ice Ih deformation shocks is nearly isothermal on both the 100 and 263 K Hugoniots. In Figure 2.19, the $T_0 = 263$ K Hugoniot extends nearly isothermally into the liquid water stability field. Although there may be partial melting, the entropy along the Hugoniot indicates that the shocked ice will remain primarily in the ice Ih phase.

From 263 K, the pressures and volumes along the ice VI region of the Hugoniot indicate a mixture of ice VI and liquid water; therefore, the Hugoniot follows the temperatures along the phase boundary. The composition along the ice VII region of the Hugoniot is more complicated, and, based on the pressure-volume and pressure-entropy phase diagram analyses, the Hugoniot initially follows the ice VII-liquid water phase boundary before entering the ice VII stability field. There is a discontinuity on the Hugoniot near 6 GPa,

corresponding to the point where the shock velocity will overdrive the elastic precursor wave. Above 6 GPa, the Hugoniot lies along the ice VII-liquid water phase boundary and enters the liquid water stability field above about 20 GPa. The temperature on the 263 K Hugoniot will cross the 298 K liquid water Hugoniot (dot-dashed line) near 25 GPa (Figure 2.18).

From 100 K, comparison between the shock data and ice VI isothermal compression curves indicates that the temperature along the ice VI region of the Hugoniot is $\lesssim$ 50 K. Note that the inferred temperature increase in the ice VI region along the 100 K Hugoniot ($\lesssim$ 50 K) is less than along the 263 K Hugoniot (about 100 K, Figure 2.16). The smaller temperature increase arises from the three-wave shock fronts that are observed in this pressure range. The multiple shocks result in quasi-isentropic compression (see Figures 2.15 and 2.7).

The shock temperatures in the ice VII region are constrained by the estimated entropy increase, based on the 263 K Hugoniot, and a single data point at 5.2 GPa and 300 K, where the temperature is inferred by comparison with ice VII isotherms (Figure 2.17). The increase in entropy upon shock compression above 2.2 GPa (with a two-wave shock front) is consistent with the temperature discontinuity shown at 2.2 GPa.

Above 6 GPa, the T_0 = 100 K Hugoniot should follow the ice VII-liquid water phase boundary up to about 20 GPa, when the Hugoniot enters the liquid stability field. The T_0 = 100 K Hugoniot should cross the liquid water Hugoniot above about 35 GPa (Figure 2.18). Previous studies have used the liquid water Hugoniot as a reference to derive solid and porous ice Hugoniots and estimate shock temperatures [e.g., *Bakanova et al.*, 1976; *Ahrens and O'Keefe*, 1985]. On the solid ice Hugoniot, liquid water is a good reference state only in the region where the ice Hugoniot lies above the liquid water Hugoniot, above 35 GPa. Similarly, derivation of the thermodynamic properties of liquid water from the solid ice Hugoniot [e.g., *Bakanova et al.*, 1976] is only valid above 35 GPa.

2.6 Release from Shock

Shocked materials, that either retain or lose strength, are released to ambient pressure by a spreading rarefaction wave propagating with a maximum velocity corresponding to the longitudinal or bulk sound velocity in the shocked state, respectively (the so-called sound velocity along the Hugoniot). The release path, if controlled by a spreading rarefaction wave,

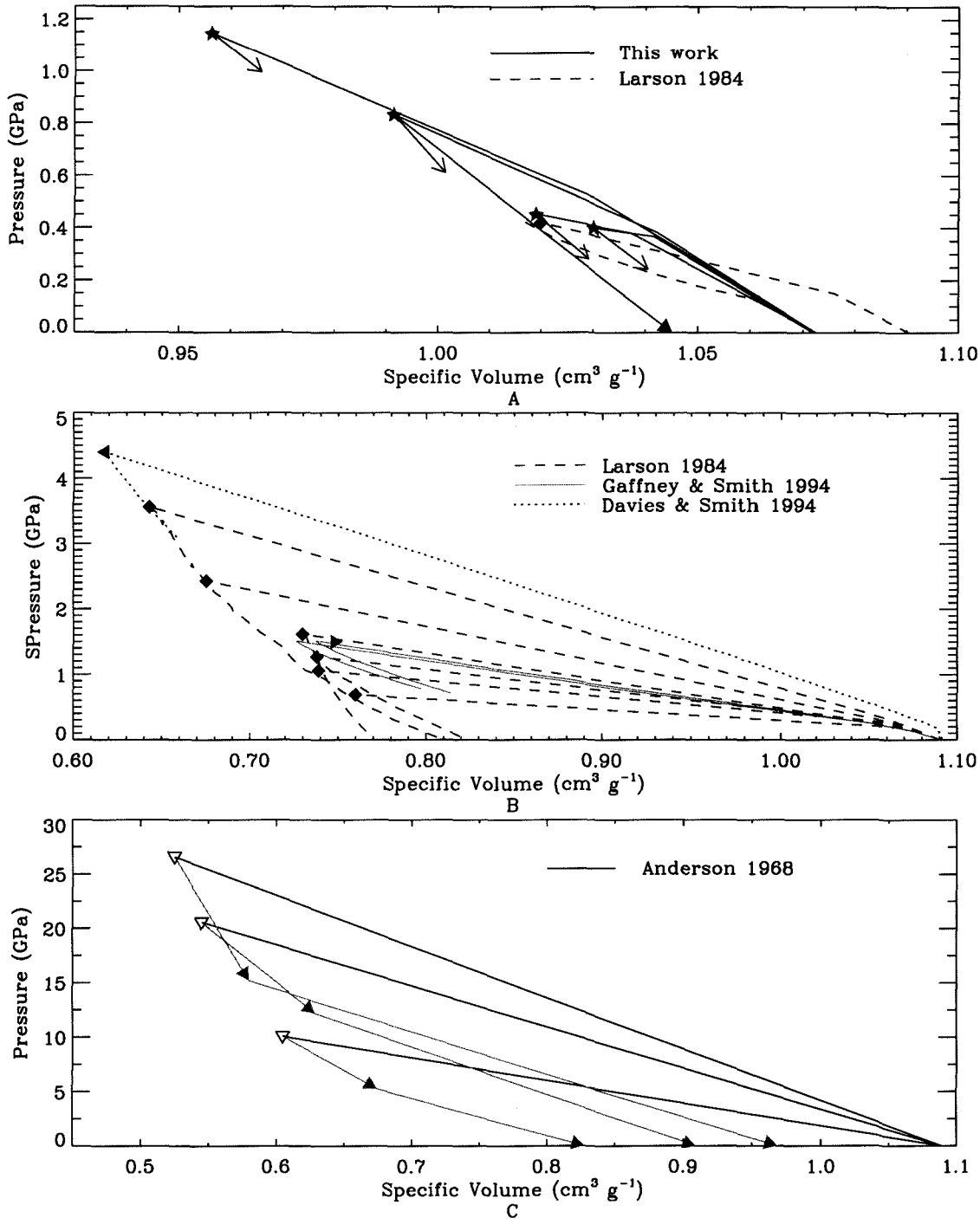

Figure 2.20: Shock loading and release paths shown with Hugoniot data. **A.** Release paths from ice Ih region lie below Hugoniot. **B.** Release paths from ice VI and VII regions follow Hugoniot. **C.** Release paths from liquid water region lie above Hugoniot.

is assumed to be isentropic [e.g., *Ahrens*, 1987]. However, if the sound velocity increases as the pressure decreases, a rarefaction shock will occur and entropy will be gained upon decompression.

The release path is necessary to derive the total irreversible work on the ice from the dynamic compression, and release wave velocities have been used to infer phase transformations along the Hugoniot. On the solid ice Hugoniot, shock release profiles fall into three regimes, shown in Figure 2.20: A. Shocks to the Ice Ih region follow stress-volume release paths below the Hugoniot. B. After shock transformation to ice VI or VII (0.6-5.5 GPa), ice unloads along the ice VI and VII regions of the Hugoniot. C. Release paths after shock transformation to liquid water (> 6 GPa) lie above the Hugoniot.

Solid ice release path information has been obtained using three methods: (1). Two or more embedded gauges resolve the release wave profile, and the $\sigma - V$ path is derived from a Lagrangian analysis [*Larson*, 1984; *Gaffney and Smith*, 1994; *Davies and Smith*, 1994, where the $\sigma - V$ paths have been reproduced from published figures]. These paths have no arrows in Figure 2.20. (2). Release wave arrival times (this work) define the sound speed c_r on the Hugoniot and the initial slope of the isentropic release path off the Hugoniot by

$$c_r = V\sqrt{-\left(\frac{\mathrm{d}P}{\mathrm{d}V}\right)_S}. \tag{2.20}$$

The initial release slopes are indicated with V-shaped arrowheads in Figure 2.20. (3). The particle velocity is measured at a known pressure on the release path and the release volume is derived using the Riemann integral [c.f., *Ahrens et al.*, 1969] assuming a straight line path in $u_p - P$ space between the volume on the Hugoniot, V_H, and the volume on the release path, V_R:

$$V_R = V_H + \int_{u_p,R}^{u_p,H} \left(\frac{\mathrm{d}u_p}{\mathrm{d}P}\right)_S \mathrm{d}u_p. \tag{2.21}$$

These release points are indicated with solid arrowheads in Figure 2.20 [*Anderson*, 1968, and this work]. Note that the volume derived with this method usually underestimates the true volume in the completely release state but is useful for deriving the trend in the release path (below, along, or above the Hugoniot).

The measured or derived sound velocities on the Hugoniot are given in Figure 2.21. In the ice Ih shock region, the release paths lie below the Hugoniot (Figure 2.20A). The temperature increase is negligible in this region (Figure 2.14). The sound velocity on the

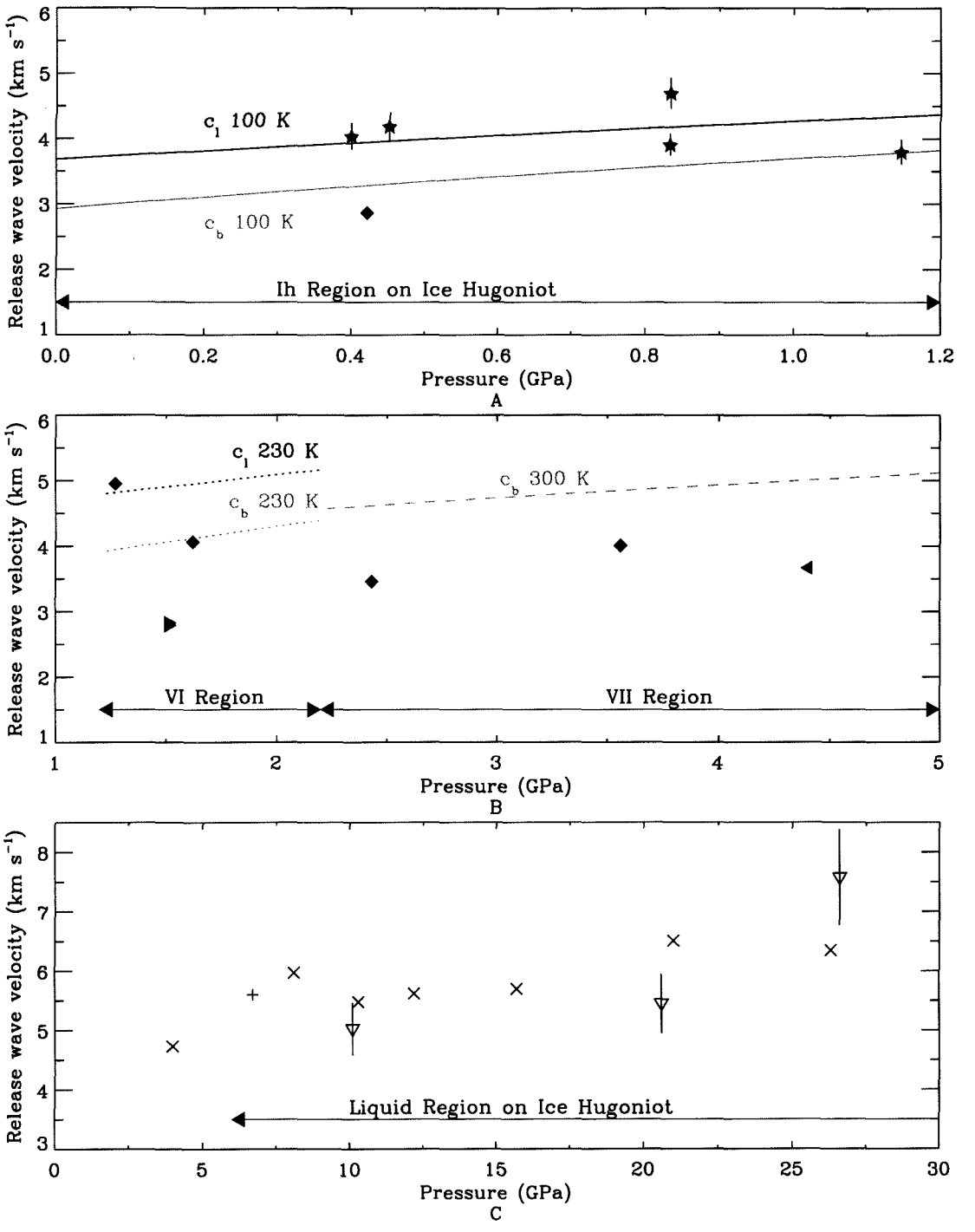

Figure 2.21: Release wave velocities vs. pressure along solid ice Hugoniot. **A.** Release velocities data with Ice Ih longitudinal (c_l) and bulk (c_b) sound velocities. **B.** Release velocity data and sound velocities in ice VI and VII. **C.** Release velocity data in liquid region and previous release velocities on liquid water Hugoniot [+ *Al'tshuler et al.*, 1960] [× *Bakanova et al.*, 1976].

Hugoniot is compared to the longitudinal (c_l) and bulk (c_b) sound speeds along the solid ice isotherm in Figure 2.21A. The $T_0 = 100$ K data appear to retain strength on the Hugoniot, in good agreement with c_l, up to the ice Ih shock cusp at 1.16 GPa when the sound speed drops to the bulk value. We note that the release wave profile near 0.5 GPa, published by *Larson* [1984], is unreliable because a steady shock wave did not develop. The release wave velocity reported by Larson is consistent with c_b. In comparison, decaying waves with $T_0 = 100$ K at the same pressure have sound speeds more consistent with c_l.

In the ice VI region of the Hugoniot (Figure 2.21)B, the release velocities are quite scattered. The $T_0 = 263$ K data should be an ice VI-liquid water mixture, which would be consistent with sound speeds below the ice VI c_b. The release paths in the ice VI region are the least understood.

The release information from the ice VII region (all $T_0 = 263$ K) are consistent with an ice VII-liquid water mixture. The sound velocities lie below the pure ice VII c_b. The release paths in the ice VI and VII regions are consistent with the idea of "frozen release" where the mixed composition in the shock remains constant over most of the release path, reverting to equilibrium states near full release [c.f., *Sekine et al.*, 1995]. Notably, *Larson* [1984] reports release paths to zero pressure which are consistent with a metastable high-pressure phase, although from this pressure region, at or just before full release to ambient pressure, the ice will partially or completely melt.

Above 6 GPa, liquid water forms on the solid ice Hugoniot, and the release paths, which lie above the Hugoniot, are consistent with release in the liquid state. In addition, the inferred sound velocity along this region of the Hugoniot is consistent with measurements of the sound velocity along the liquid water Hugoniot (Figure 2.21C) [*Bakanova et al.*, 1976; *Al'tshuler et al.*, 1960].

2.7 Discussion

2.7.1 Impact-induced Melting of Ice on Planetary Surfaces

Unlike silicates, where shock-induced melting occurs upon release from shock pressures of 10's-100's GPa [c.f., *Ahrens and O'Keefe*, 1972; *Pierazzo et al.*, 1997], shock-induced melting of ice begins at extremely low pressures, at only a few GPa. Shock-induced melting and metamorphism during impact cratering events are important surface-modification processes

in the solar system. In the next chapter, we will address the problem of shock-induced melting of subsurface ice on Mars and the formation of fluidized ejecta blankets.

The criteria for shock-induced melting is derived from the entropy of melting under ambient conditions. The release paths and velocities indicate that ice unloads approximately isentropically after shock compression to regions of phase transformation (regions 3-5) on the Hugoniot. Thus, the shock pressure required for melting upon release may be determined from examination of the Hugoniots in the $P - S$ phase diagram (Figure 2.15).

Along the 263 K Hugoniot, the entropy is larger than the critical value for incipient melting (vertical grey line labeled IM in Figure 2.15) at pressures greater than 0.6 GPa. Therefore, shocks to the ice VI region on the Hugoniot will partially melt upon release to pressures at or below 6 mb. The entropy along the ice VII region of the 263 K Hugoniot is larger than the critical entropy for complete melting (CM) above about 3.7 GPa.

At pressures less than 2.2 GPa on the 100 K Hugoniot, the entropy is less than the critical entropy for incipient melting. Upon shock-transformation to ice VII, however, incipient melting will occur on release from about 4.5 GPa. From 100 K, the ice will melt completely upon release from 5-6 GPa, the region of shock-transformation to liquid water on the Hugoniot.

Previous estimates of the critical pressures for melting have been much higher. *Kieffer and Simonds* [1980] derived critical values of 3 GPa for incipient melting and 10 GPa for complete melting under terrestrial conditions, based on sparse H_2O shock data. *Ahrens and O'Keefe* [1985] report 7.6 and 10.8 GPa for IM and CM, respectively, at 70 K and 1 bar, and 6.2 and 9.6 GPa, at 263 K and 1 bar.

We find that shock-induced melting of ice should be widespread in planetary impact processes and mutual collisions between icy bodies (also, see Chapter 3). The critical pressures for IM and CM may be interpolated between the 100 and 263 K Hugoniots.

2.7.2 Formation of Metastable High-pressure Ice Polymorphs from Impact Events

Our analysis of the solid ice Hugoniot motivates a critical re-examination of the hypothesis by *Gaffney and Matson* [1980] that high-pressure ice polymorphs created by shock-processes may remain metastable upon release.

The likelihood of stability upon release may be inferred from the release wave profiles

and the entropy along the Hugoniot. In static recovery experiments, the ice is maintained at low temperatures (e.g., lN_2 at 77 K) to slow the temperature-dependent kinetics of the reverse transformation to ice Ih.

For the average surface temperatures in the solar system (Figure 2.1), the 100 K Hugoniot is an appropriate reference for shock-induced phase changes from impact events in the icy outer solar system. We have shown that shocks to pressures below 2.2 GPa along the 100 K Hugoniot are approximately isentropic. Therefore, the temperature increase from the shock is small (10's K, Figure 2.19). It is plausible that ice in the cold outer solar system, subject to shocks with amplitudes between 1-2.2 GPa may form ice VI, which could remain metastable upon release. Ice II is probably not formed during impact events because the dynamic strength of ice Ih and ice Ih transformation shocks have amplitudes which lie in the ice II stability field.

For shocks above 2.2 GPa, on the other hand, the increase in entropy, and corresponding increase in temperature, is probably too large for ice VII to be recovered under ambient conditions. Under shocks greater than 6 GPa, ice will completely melt upon release and slowly freeze and sublimate from conductive and radiative processes.

At the lowest temperatures in the outer solar system, e.g., at Pluto and the Kuiper Belt, other phases of ice may be important in shock processes, e.g., the amorphous phases. These should be examined in future studies with temperatures below 100 K. We note that the increase in entropy from shock compression of porous ice will be larger than sold ice because of the larger initial volume.

The region of pressure and temperature space where ice VI may remain metastable after a shock is small, limited to temperatures $\leq$ 100 K and pressures of about 1-2.2 GPa. Shock-induced transformation to ice VI is probably not an important process on planetary surfaces. Shock-induced melting, however, will be a widespread surface modification process.

2.8 Conclusions

1. We have conducted the first experimental investigation of the solid ice Hugoniot at initial temperatures of 100 K. Analysis of the combined data, from this study and previous work at 263 K, shows that shock-induced phase transformations to ice VI and VII are the dominant features along the Hugoniot at pressures below 6 GPa,

which results in the generation of multiple-wave shock fronts. The pressure at which ice begins to melt along the Hugoniot varies with initial temperature, and at pressures above about 20 GPa melting is complete along the Hugoniot.

2. We have identified five regions on the solid ice Hugoniot: (1) elastic shock waves, (2) ice Ih deformation shocks, transformation shocks to (3) ice VI, (4) ice VII, and (5) liquid water. In each region, data obtained at different initial temperatures are described by a single $U_S - \Delta u_p$ shock equation of state. Comparison of Δu_p between data sets removes the effects of the temperature dependence on the elastic precursor and ice Ih deformation shock.

3. The dynamic strength of ice Ih is strongly dependent on temperature. The Hugoniot Elastic Limit varies from 0.05 to 0.62 GPa, as a function of temperature and peak shock stress.

4. Ice Ih deformation shocks do not propagate as steady shock waves except at low temperatures as an intermediate shock wave in a three-wave shock front, consisting of the elastic precursor, ice Ih deformation shock, and transformation shock to ice VI. Under temperate conditions, or when subject to peak stress less than 0.6 GPa, the ice Ih shock decays with propagation. Along the ice Ih region of the Hugoniot, a cusp at 1.16 GPa defines the maximum stress attainable by an ice Ih deformation shock.

5. We estimate the entropy and temperature along the 100 and 263 K Hugoniots and derive the critical pressures for shock-induced incipient (IM) and complete (CM) melting upon release. At 100 K, the critical pressures are about 4.5 and between 5-6 GPa for IM and CM, respectively. At 263 K, the critical pressures are 0.6 and 3.7 GPa for IM and CM, lower than previously suggested.

6. Ice VI may remain metastable upon release from shock pressures between $1-2.2$ GPa, if under temperatures which would inhibit reverse transformation to ice Ih (e.g., lN_2 temperatures). The increase in entropy and temperature upon shock transformation to ice VII prevents recovery of the high-pressure phase upon release. Thus, shock-induced formation of high-pressure solid ice polymorphs should be relatively rare. Shock-induced melting of ice, however, will be widespread in impact events.

Bibliography

Ahrens, T. J., Shock wave techniques for geophysics and planetary physics, in *Methods of Experimental Physics*, edited by C. Sammis and T. Henyey, vol. 24A, chap. 6, pp. 185–235, Academic Press, Inc., 1987.

Ahrens, T. J., and J. D. O'Keefe, Shock melting and vaporization of lunar rocks and minerals, *Moon*, *4*, 214–249, 1972.

Ahrens, T. J., and J. D. O'Keefe, Shock vaporization and the accretion of the icy satellites of Jupiter and Saturn, in *Ices in the Solar System*, edited by J. Klinger, D. Benest, A. Dollfus, and R. Smoluchowski, NATO ASI Series, pp. 631–654, D. Reidel, Nice, France, 1985.

Ahrens, T. J., C. F. Peterson, and J. T. Rosenberg, Shock compression of feldspars, *J. Geophys. Res.*, *74*, 2727–2746, 1969.

Al'tshuler, L. V., S. B. Kormer, M. I. Brazhnik, L. A. Vladimirov, M. P. Speranskaya, and A. I. Funtikov, The isentropic compressibility of aluminum, copper, lead, and iron at high pressures, *Soviet Physics JETP*, *11*, 766–775, 1960, (originally published J. Exptl. Theoret. Phys. (USSR) 38, 1061-1073, April, 1960.).

Anderson, G. D., The equation of state of ice and composite frozen soil material, CRREL Research Report 257, Cold Regions Research & Engineering Laboratory, Hanover, New Hampshire, 1968.

Arakawa, M., K. Shirai, and M. Kato, Shock wave and fracture propagation in water ice by high velocity impact, *Geophys. Res. Lett.*, *27*, 305–308, 2000.

Bakanova, A. A., V. N. Zubarev, Y. N. Sutulov, and R. F. Trunin, Thermodynamic properties of water at high pressures and temperatures, *Sov. Phys.-JETP*, *41*, 544–548, 1976, (originally published Zh. Eksp. Teor. Fiz. 68, 1099-1107, 1975.).

Bancroft, D., E. L. Peterson, and S. Minshall, Polymorphism of iron at high pressure, *Journal of Applied Physics*, *27*, 291–298, 1956.

Bevington, P. R., *Data Reduction and Error Analysis for the Physical Sciences*, chap. Propagation of Errors, McGraw Hill, 1969.

Cowperthwaite, M., and R. F. Williams, Determination of constitutive relationships with multiple gauges in nondivergent waves, *Journal of Applied Physics*, *42*, 456–462, 1971.

Davies, F. W., and E. A. Smith, High pressure equation of state investigation of rocks, *Technical Report DNA-TR-94-1*, Defense Nuclear Agency, Ktech Corporation, 901 Pennsylvania Avenue, NE, Albuquerque, NM 87110-7491, 1994.

Dorsey, N. E. (Ed.), *Properties of Ordinary Water-Substance*, Reinhold Pub. Corp., New York, 1940.

Dremin, A. N., and G. A. Adadurov, The behavior of glass under dynamic loading, *Soviet Physics-Solid State*, *6*, 1379–1384, 1964, (Translated from Fizika Tverdogo Tela 6(6):1757-1764, 1964.).

Dremin, A. N., and K. K. Shvedov, Estimation of Chapman-Jouget pressure and time of reaction in detonation waves of powerful explosives, *J. Appl. Mech. Tech. Phys.*, *2*, 154–159, 1964, in Russian.

Duffy, T., and T. Ahrens, Dynamic-response of molybdenum shock-compressed at 1400-degrees-C, *Journal of Applied Physics*, *76*, 835–842, 1994.

Durham, W., and L. Stern, Rheological properties of water ice - applications to satellites of the outer planets, *Annual Review of Earth and Planetary Sciences*, *29*, 295–330, 2001.

Durham, W., H. Heard, and S. Kirby, Experimental deformation of polycrystalline H_2O ice at high-pressure and low-temperature - preliminary results, *J. Geophys. Res.*, *88*, B377–B392, 1983.

Durham, W., S. Kirby, and L. Stern, Rheology of planetary ices, in *Solar System Ices*, edited by B. Schmitt, C. de Bergh, and M. Festou, vol. 227 of *Astrophysics and Space Science Library*, pp. 63–78, Kluwer Academic Publishers, 1998.

Fei, Y., H.-K. Mao, and R. J. Hemley, Thermal expansivity, bulk modulus, and melting curve of H_2O-ice VII to 20 GPa, *Journal of Chemical Physics*, *99*, 5369–5373, 1993.

Fowles, R., Dynamic compression of quartz, *J. Geophys. Res.*, *72*, 5729–5742, 1967.

Fowles, R., and R. F. Williams, Plane stress wave propagation in solids, *J. Appl. Phys.*, *41*, 360–363, 1970.

Gaffney, E. S., Study of the nature of shock waves in frozen earth materials, *Report SSS-R-73-1557*, Systems Science and Software, P.O. Box 1620, La Jolla, California 92037, 1973, submitted to U.S. Army Cold Regions Research & Engineering Laboratory.

Gaffney, E. S., Hugoniot of water ice, in *Ices in the Solar System*, edited by J. Klinger, D. Benest, A. Dollfus, and R. Smoluchowski, NATO ASI Series, pp. 119–148, D. Reidel, Nice, France, 1985.

Gaffney, E. S., and T. J. Ahrens, Identification of ice VI on the Hugoniot of ice I_h, *Geophys. Res. Lett.*, *7*, 407–409, 1980.

Gaffney, E. S., and D. L. Matson, Water ice polymorphs and their significance on planetary surfaces, *Icarus*, *44*, 511–519, 1980.

Gaffney, E. S., and E. A. Smith, Hydroplus experimental study or dry, saturated, and frozen geological materials, *Technical Report DNA-TR-93-74*, Defense Nuclear Agency, Ktech Corporation, 901 Pennsylvania Avenue, NE, Albuquerque, NM 87110-7491, 1994.

Gagnon, R., H. Kiefte, M. Clouter, and E. Whalley, Pressure dependence of the elastic constants of ice Ih to 2.8 kbar by Brillouin spectroscopy, *J. Chem. Phys.*, *89*, 4522–4528, 1988.

Giauque, W. F., and J. W. Stout, The entropy of water and the third law of thermodynamics, *J. Am. Chem. Soc.*, *58*, 1144–1150, 1936.

Hawkes, I., and M. Mellor, Deformation and fracture of ice under uniaxial stress, *Journal of Gaciology*, *11*, 103–131, 1972.

Hobbs, P. V., *Ice Physics*, Clarendon Press, Oxford, 1974.

Jeanloz, R., Properties of iron at high pressures and the state of the core, *J. Geophys. Res.*, *84*, 6059–6069, 1979.

Jeanloz, R., Shock wave equation of state and finite strain theory, *J. Geophys. Res.*, *94*, 5873–5886, 1989.

Kieffer, S. W., and C. H. Simonds, The role of volatiles and lithology in the impact cratering process, *Reviews of Geophysics and Space Physics*, *18*, 143–181, 1980.

Kormer, S. B., Optical study of the characteristics of shock-compressed condensed dielectrics, *Soviet Physics USPEKHI*, *11*, 229–254, 1968, (originally published in Usp. Fiz. Nauk 94, 641-687, April 1964.).

Lange, M. A., and T. J. Ahrens, The dynamic tensile strength of ice and ice-silicate mixtures, *J. Geophys. Res.*, *88*, 1197–1208, 1983.

Larson, D., Shock-wave studies of ice under uniaxial strain conditions, *Journal of Glaciology*, *30*, 235–240, 1984.

Larson, D. B., G. D. Bearson, and J. R. Taylor, Shock-wave studies of ice and two frozen soils, in *Permafrost: The North American Contribution to the Second International Conference*, pp. 318–325, Nat. Acad. Sci., Washington, 1973.

Loree, T. R., F. S. Minshall, and D. Stirpe, The overdriving effect in dynamic polymorphism,

Tech. Rep. LA-3215, Los Alamos Laboratory, Los Alamos, New Mexico, 1965.

Lyzenga, G. A., T. J. Ahrens, W. J. Nellis, and A. C. Mitchell, The temperature of shock-compressed water, *J. Chem. Phys.*, *76*, 6282–6286, 1982.

Marsh, S. P. (Ed.), *LASL Shock Hugoniot Data*, University of California Press, 1980.

Mashimo, T., M. Uchino, A. Nakamura, T. Kobayashi, E. Takasawa, T. Sekine, Y. Noguchi, H. Hikosaka, K. Fukuoka, and Y. Syono, Yield properties, phase transition, and equation of state of aluminum nitride (AlN) under shock compression up to 150 GPa, *Journal of Applied Physics*, *86*, 6710–6716, 1999.

Miller, G., E. Stolper, and T. Ahrens, The equation of state of a molten Komatiite 1. shock-wave compression to 36 GPa, *J. Geophys. Res.*, *96*, 11,831–11,848, 1991.

Minshall, S., Investigation of a polymorphic transition in iron at 130 k.b., *Physical Review*, *98*, 271, 1955.

Mishima, O., N. Mori, and S. Endo, Thermal expansion anomaly of ice VI related to the order-disorder transition, *J. Chem. Phys.*, *70*, 2037–2038, 1979.

Murnaghan, F. D., The compressibility of media under extreme pressure, *Proc. Natl. Acad. Sci. U.S.A.*, *30*, 244–247, 1944.

Petersen, C. F., W. J. Murri, and M. Cowperthwaite, Hugoniot and release-adiabat measurements for selected geologic materials, *J. Geophys. Res.*, *75*, 2063–2072, 1970.

Petrenko, V. F., and R. W. Whitworth, *Physics of Ice*, chap. The Other Phases of Ice, pp. 253–286, Oxford University Press, New York, 1999.

Pierazzo, E., A. Vickery, and H. Melosh, A reevaluation of impact melt production, *Icarus*, *127*, 408–423, 1997.

Rice, M. H., and J. M. Walsh, Equation of state of water to 250 kilobars, *Journal of Chemical Physics*, *26*, 824–830, 1957.

Rosenberg, Z., On the relation between the Hugoniot elastic limit and the yield strength of brittle materials, *Journal of Applied Physics*, *74*, 752–753, 1993.

Rosenberg, Z., N. Brar, and S. Bless, Dynamic high-pressure properties of AlN ceramic as determined by flyer plate impact, *Journal of Applied Physics*, *70*, 167–169, 1991.

Röttger, K., A. Endriss, S. Ihringer, J.aAnd Doyle, and W. Kuhs, Lattice constants and thermal expansion of H_2O and D_2O ice Ih between 10 and 265 K, *Acta Cryst.*, pp. 644–648, 1994.

Ruoff, A. L., Linear shock-velocity-particle-velocity relationship, *J. of Applied Physics*, *38*,

4976–4980, 1967.

Sekine, T., T. Duffy, A. Rubin, W. Anderson, and T. Ahrens, Shock compression and isentropic release of granite, *Geophysical Journal International*, *120*, 247–261, 1995.

Simmons, G., and H. Wang, *Single Crystal Elastic Constants and Calculated Aggregate Properties: A Handbook*, MIT Press, 1971.

Sotin, C., O. Grasset, and S. Beauchesne, Thermodynamic properties of high pressure ices: Implications for the dynamics and internal structure of large icy satellites, in *Solar System Ices*, edited by B. Schmitt, C. de Bergh, and M. Festou, vol. 227 of *Astrophysics and Space Science Library*, pp. 79–96, Kluwer Academic Publishers, 1998.

Stewart, S. T., and T. J. Ahrens, Correction to the dynamic tensile strength of ice and ice-silicate mixtures (Lange & Ahrens 1983), in *Proc. Lunar Planet. Sci. Conf.*, vol. 30, Abs. 2037, 1999.

Swegle, J. W., and D. E. Grady, Shock viscosity and the prediction of shock wave rise times, *J. Applied Physics*, *58*, 692–701, 1985.

Tulk, C., H. Kiefte, M. Clouter, and R. Gagnon, Elastic constants of ice III, V, and VI by Brillouin spectroscopy, *Journal of Physical Chemistry B*, *101*, 6154–6157, 1997.

Voigt, W., *Lehrbuch der Krystallphysik*, B. G. Teubner, Leipzig, 1928.

Walsh, J. M., and M. H. Rice, Dynamic compression of liquids from measurements on strong shock waves, *Journal of Chemical Physics*, *26*, 815–823, 1957.

Zhugin, Y., K. Krupnikov, N. Ovechkin, E. Abakshin, M. Gorshkov, V. Zaikin, and V. Slobodenyukov, On some peculiarities of dynamic compressibility of quartz, *Physics of the Solid Earth*, *30*, 868–874, 1994.

Zhugin, Y. N., Behavior of α-quartz at high dynamical and static pressures: New results and concepts, *Chem. Phys. Repts.*, *14*, 78–85, 1995.

Chapter 3 Rampart Crater Formation on Mars

Sarah T. Stewart, John D. O'Keefe, and Thomas J. Ahrens

3.1 Introduction

The presence of large quantities of water on Mars has been inferred from geomorphic features, most notably valley networks and catastrophic outflow channels [*Carr*, 1996]. In addition, many Martian impact craters are surrounded by ejecta blankets with the appearance of fluidized ground-hugging flow and terminated by one or more continuous ramparts [*Barlow and Bradley*, 1990]. The prevalent hypothesis for the formation of rampart ejecta morphologies is excavation and entrainment of subsurface ice or water into the ejecta blanket and subsequent long runout fluidized flow, forming a distal scarp when loss of fluidization occurs [*Carr et al.*, 1977; *Mouginis-Mark*, 1981; *Wohletz and Sheridan*, 1983]. Alternatively, atmospheric entrainment of fine ejecta particles may be the dominant process controlling distal rampart morphologies, particularly ejecta blanket sinuosity [*Schultz and Gault*, 1979; *Schultz*, 1992; *Barnouin-Jha and Schultz*, 1998]. In the atmospheric entrainment model, subsurface volatiles may contribute to the variability in morphologies and near crater rim ejecta properties. If ejecta fluidization can be related to ground ice, the occurrence and morphology of rampart ejecta could be used to map the distribution and amount of subsurface water, and rampart craters would be a powerful probe of the history of H_2O on Mars.

Kuz'min et al. [1988a], in a major mapping study of single- and multiple-layer ejecta morphologies, found that the minimum diameter crater showing rampart features was correlated with latitude. The onset diameter of rampart craters was about 1 km at 60° latitude and 6 km near the equator. The excavation depths of craters in this size range correlates well with models of the equilibrium stability depth of ice in the Martian crust [*Fanale et al.*, 1986; *Clifford*, 1993; *Mellon et al.*, 1997]. They attempted to map the relative subsurface H_2O content implied by rampart craters by examining the spatial distribution of different rampart ejecta morphologies, but they could not quantify their results without a physical model of rampart crater formation.

Although several phenomenological models have been suggested to explain the formation of single vs. multiple-layered rampart ejecta blankets [e.g., *Mouginis-Mark*, 1981; *Barlow and Bradley*, 1990], no previous study has focused on a modeling effort to explain the ejecta fluidization by ground ice or water and the formation of different rampart morphologies. Without a formation model, rampart crater studies were focused on derivation of the rheological properties of the spreading ejecta blanket [*Ivanov*, 1996; *Ivanov and Pogoretsky*, 1996; *Ivanov et al.*, 1997; *Baratoux et al.*, 2001; *Baratoux*, 2001]. These studies relied upon initial conditions for the ejecta flow derived from scaling laws developed from experimental cratering in dry, particulate and solid, rock targets [e.g., *Holsapple*, 1993; *Holsapple and Schmidt*, 1982].

Experimental studies of cratering in viscous materials [*Gault and Greeley*, 1978; *Fink et al.*, 1981] and atmospheric entrainment of fine ejecta [*Schultz*, 1992; *Barnouin-Jha and Schultz*, 1996; *Barnouin-Jha et al.*, 1999] have both produced lobate morphologies and occasional distal ramparts. The difficulties related to scaling laboratory conditions which yield rampart morphologies to planetary-scale impact events has prevented derivation of physical properties of the Martian crust with the results from these studies.

Until recently the shock properties of H_2O ice were not understood well enough to be explicitly considered in models of cratering under Martian conditions. Previous studies of the ice shock Hugoniot have estimated the pressures required for shock-induced melting of ice at 6.2 and 10 GPa [*Ahrens and O'Keefe*, 1985; *Kieffer and Simonds*, 1980]. Consequently, *Boyce et al.* [1996] and *Boyce and Roddy* [1997] have suggested that the shock pressures imposed on Mars surface materials from an impact event were insufficient to melt ground ice within the volume of material ejected from the crater transient cavity. They conclude that rampart ejecta did not form as the result of shock-melting H_2O ice but were evidence for widespread near-surface liquid water aquifers. Since liquid aquifers are not expected to be present near the surface of the Martian crust in the present climate [e.g., *Clifford*, 1993], rampart ejecta formation models which require pre-existing liquid water, if correct, would provide an important clue about previous climate on Mars.

Recently, an experimental study of the shock properties of H_2O ice has shown that shock-induced melting begins at shock pressures of only 0.6 GPa under terrestrial conditions (Chapter 2), more than an order of magnitude lower than the 6.2-10 GPa previously inferred. Computer simulations of planetary-scale impacts onto an ice-rock mixture may

now explicitly take into account the effects of shock-induced melting of the ice component. In this work, we present simulations of impact events onto an ice-filled regolith, quantifying the differences in the excavation process compared to cratering on pure rock surfaces. From the simulation results and the criteria for shock-induced melting, we derive the physical properties of the ejected material. We present a model for the formation of different rampart crater morphologies and estimate the H_2O content of the Martian regolith. In this work, we adopt the rampart ejecta terminology presented in *Barlow et al.* [2000].

3.2 Simulations of Crater Formation on Mars

We modeled impact crater formation using the CTH code [*McGlaun et al.*, 1990], an Eulerian shock wave and material deformation code with some Lagrangian features. Normal impacts under Martian gravity were simulated using two-dimensional cylindrical symmetry, where z is the vertical dimension and x the horizontal. The cell size increased by a constant scaling factor, typically about 1.02, from the impact point to the edge of the Eulerian mesh, shown in Figure 3.1A. For most calculations, the projectile radius spanned more than 30 cells, which is sufficient to model the shock release profile [*Pierazzo et al.*, 1997]. Because long calculation times are required for crater excavation and ejecta emplacement, the mesh extent was large to minimize edge effects, although low-amplitude reflections were observed from the bottom of the mesh after crater excavation. A typical calculation mesh spanned $-500 < z < 150\ r_p$ and $0 < x < 250\ r_p$ where r_p is the projectile radius. Massless Lagrangian tracer particles are placed in the mesh (Figure 3.1B) to determine the shock pressure decay profile with depth, ejection angles and velocities, and the excavated zone. The simulations were stopped before all the ejecta landed, and the tracer particle information was used to determine the properties of the ejecta blanket.

The model Martian surface was 300-500 r_p thick, or some 200-300 mesh cells deep. Each cell was initialized in lithostatic equilibrium under Martian gravity, 3.7 m s^{-2}, as an isothermal layer with $T_0 = 200$ K, representative of Martian mid-latitudes [*Kieffer et al.*, 1992]. We considered a range of ice content using an exponential decay profile to simulate a theoretical Martian regolith with ice-filled cracks and pore spaces after the work by *Clifford*

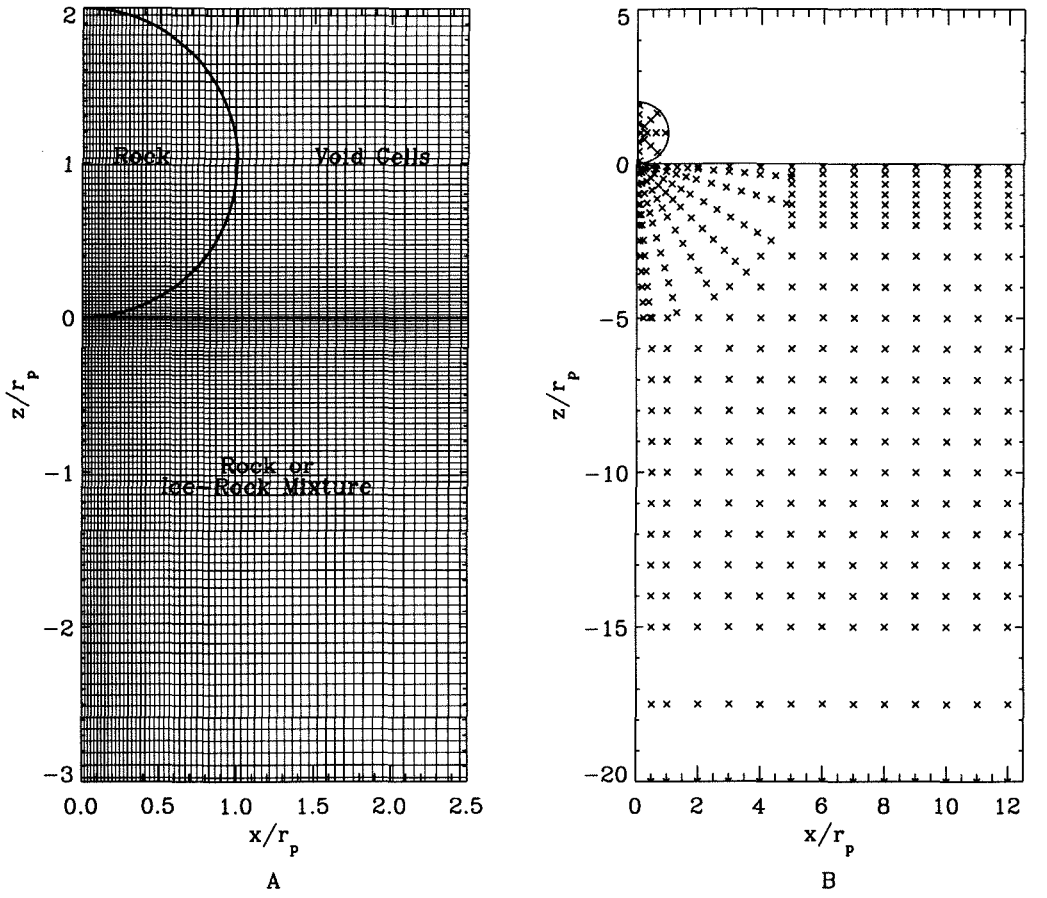

Figure 3.1: CTH Eulerian mesh and Lagrangian tracer particle distribution used in cratering simulations. **A.** Close view of mesh at the impact point. The cell size increases towards the edge of the calculation grid. Total mesh extent is about 100 times larger than shown. **B.** Massless tracer particles (×) provide time history information for the shock pressure decay, excavation process, and structural deformation.

[1993]. The ice volume fraction ϕ is given as a function of depth z by

$$\phi(z) = \phi_0 e^{z/K_z} \tag{3.1}$$

where ϕ_0 is the ice fraction at the surface and $K_z = 3$ km after *Clifford* [1993]. We considered cases where $\phi_0 = 0$, 0.1, and 0.2. Each cell was initialized with the specified ice and rock fractions under lithostatic pressure for the model run. We did not consider the effects of open porosity in this study. If there is significant H_2O in the Martian regolith, a near-surface cryosphere will form by vapor migration, filling the pore spaces with solid ice [e.g., *Clifford*, 1993; *Mellon et al.*, 1997]. The decaying ice content avoids the effects of pure layer interfaces in the model and reduces the number of mixed cells in the bottom of the

mesh, which also reduces overall computation time. In this study, we do not include the Martian atmosphere in the computation, as it does not effect the crater shape or excavation flow field in the transient cavity. Possible atmospheric effects during ejecta emplacement will be discussed below (section 3.6).

Because the focus of this work is on the effects of an ice-rock mixture, we employed simple material strength models for each component [c.f., *O'Keefe et al.*, 2001; *O'Keefe and Ahrens*, 1999]. We considered two different strength cases using a Mohr-Coulomb model: a strong surface (Y_{strong}) and a mean Martian regolith (Y_{std}). The strength model parameters are given in Table 3.1. The standard Mars model is constrained by the mean effective yield strength of the surface derived from the transition diameter from simple to complex craters; refer to Eq. 3.9 in section 3.3.2. In the Y_{strong} model, $dY/dP = 1$ and Poisson's ratio $\nu = 1$ are typical for competent rocks [*Melosh*, 1989]. In ice, $\nu = 0.33$, and the Y_{std} model reflects a decrease in the bulk effective ν from the ice component, porosity, or fractures. The net effect is the material behaves more hydrodynamically compared to the Y_{strong} model. We ran a few simulations with the Y^*_{std} model, which specified that the ice component behaves as a fluid under all conditions. The crater profiles were essentially identical to the Y_{std} runs because of the small volume fraction of ice; see discussion below.

The material strength is degraded as the temperature approaches melting and becomes hydrodynamic upon melting [see *O'Keefe and Ahrens*, 1999]. In mixed cells, the yield strength is the sum of the yield strength of each component, weighted by the volume fraction. These simulations do not take into account shock-weakening (e.g., mechanical damage or acoustic fluidization) which is important for predicting the final crater shape [e.g., *O'Keefe et al.*, 2001; *Melosh and Ivanov*, 1999], although we may estimate the final crater size.

We used the CTH HIGH_RESOLUTION material interface model to control the advection of each component through the mesh. All the advection models in the 1996 version of CTH (SLIC, HIGH_RESOLUTION, SMYRA) produced artifacts in the cratering simulations, and the ice component became slightly aligned radially from the impact point during the passage of the impact shock. Because the overall ratio of ice to rock in the excavated zone was not changed, the artifact did not have a significant effect on the focus of this study.

In all the simulations presented here, the projectile was a silicate sphere with an impact velocity of 10 km s^{-1}, the average asteroid encounter velocity with Mars [W. Bottke, pers. comm.]. The Martian surface was modeled as pure silicate or an ice-silicate mixture.

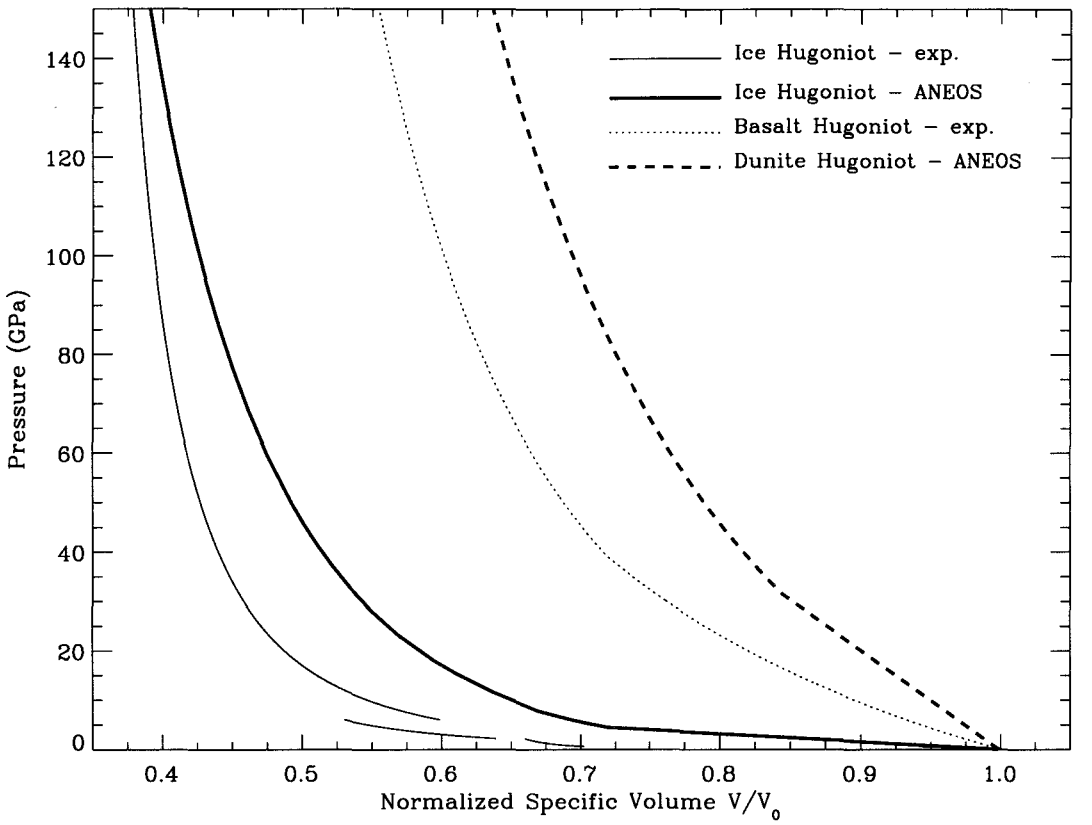

Figure 3.2: Shock Hugoniots for H_2O and dunite used in this study over the pressure range of interest for 10 km s^{-1} impacts. The experimental Hugoniots for H_2O ice and high-density basalt are more compressible than the ANEOS Hugoniots.

Dunite (ρ_0 = 3.32 g cm^{-3}) was chosen as that silicate component to be an analog for the primarily basaltic composition of the Martian surface [*Christensen et al.*, 2000] and because it has a well-defined equation of state. We used the analytic equation of state (ANEOS) [*Thompson and Lauson*, 1972] for H_2O and dunite. The ANEOS for H_2O have been revised by *Tonks et al.* [1997] to improve the vapor region. The ANEOS parameters are published in *Turtle and Pierazzo* [2001, supplemental information]. The ANEOS Hugoniots are shown in Figure 3.2 with experimental Hugoniots for ice (Chapter 2) and high-density basalt [*Ahrens and Johnson*, 1995]. The ice ANEOS Hugoniot is less compressible than the shock wave data at low pressures. The different segments on the experimental ice Hugoniot correspond to regions where different high-pressure ice polymorphs (ice VI and VII) form under planar shock waves. Above 6 GPa, ice shocks to liquid on the Hugoniot (Chapter 2). Although

there is a difference in compressibility, the H_2O ANEOS formulation is a good match for the critical pressures for shock-induced melting and vaporization.

To determine the region of shock-induced melting in an ice-rock mixture, the equation of state must agree with the critical pressures for shock melting and vaporization, and the *Tonks et al.* [1997] H_2O ANEOS is adequate for this study. The critical entropy and shock pressures for incipient and complete melting and vaporization are given in Table 3.2, where IM=incipient melting, CM=complete melting, IV=incipient vaporization, and CV=complete vaporization. Release from shock pressures is approximately isentropic [c.f. *Ahrens and O'Keefe*, 1972]. Thus, the critical pressures correspond to the point where the entropy on the Hugoniot is sufficient for incipient or complete phase change upon release to ambient pressure. The critical entropies for H_2O and dunite are given at 6 mb to be applicable to mean Martian surface pressures in the present climate (6-7 mb) [*Kieffer et al.*, 1992]. In Table 3.2, the range in critical pressures on the ice Hugoniot for IM and CM corresponds to variations in the initial temperature. At 263 K, the critical pressures are about 0.6 and 3.0 GPa, respectively (Chapter 2). Interpolating between 100 K and 263 K experimental ice datasets, the critical pressures at 200 K may be as high as 2 and 5 GPa.

Even though the average abundance of water vapor in the Martian atmosphere is about 0.03% [*Kieffer et al.*, 1992], the 6-7 mb CO_2 atmosphere inhibits rapid vaporization of water on the time scales of crater formation and ejecta emplacement (several minutes) [refer to *Hecht*, 2000]. Thus, the appropriate release pressure to specify the entropies required for shock-induced melting and vaporization of ice is the ambient atmospheric pressure. Shock-induced melt would remain liquid, perhaps forming an ice crust, during ballistic ejection (see section 3.6).

CTH includes several cell thermodynamics options to determine the state of a mixed cell, including (1) forcing the same pressure and temperature in each component (1PT), (2) fitting the same pressure but allowing each component to have different temperatures (MMT), and (3) allowing different pressures and temperatures in each component (MMP2). Normally, the more compressible material will have higher shock temperatures. Hence, the 1PT option is not realistic for an ice-rock mixture. The MMT option would simulate an ideal intimate mixture, corresponding, for example, to ice confined to pore spaces much smaller than the thickness of the shock front, which is of order the projectile radius for planetary impact events [*Melosh*, 1989]. This option, however, causes unrealistic heating of very low-

density materials. The MMP2 option equalizes the PdV work on each cell according to the compressibility of each material. Thus, the more compressible ice experiences lower peak shock pressures. This case would correspond to distinct layers or deposits of ice comparable in size to the thickness of the shock front.

Table 3.1. Mohr Coulomb strength parameters for Martian impact simulations.

Strength Model	Y_0 (Pa)	$Y_{\max}$ (Pa)	$\mathrm{d}Y/\mathrm{d}P$	ν
Y_{strong}–Dunite	10^7	2×10^8	1.0	0.25
Y_{strong}–Ice	10^6	5×10^7	1.0	0.33
Y_{std}–Dunite	10^7	10^7	···	0.33
Y_{std}–Ice	10^7	10^7	···	0.33
Y^*_{std}–Ice	0	0	···	0.5

Table 3.2. Critical shock pressures for phase change on release.

Release State	H_2O Ice (6 mb) S J kg^{-1} K^{-1}	H_2O Ice (6 mb) P GPa	Dunite (6 mb) S J kg^{-1} K^{-1}	Dunite (6 mb) P GPa
IM	2290	0.6-2.0	3000	159
CM	3510	3.7-5.0	3240	181
IV	3510	3.0-5.0	3375	185
CV	12800	90.	8875	4000

Critical entropies from Chapter 2 and *Pierazzo et al.* [1997] for H_2O and dunite, respectively.

3.3 Fluidization of Ejected Material

The central hypothesis that subsurface H_2O may fluidize an ejecta blanket requires that either liquid water is present near the surface or solid ice is melted in the impact process. Rampart craters are found everywhere except on the youngest volcanic terrains [*Barlow and Bradley*, 1990], and the Mars Orbiter Laser Altimeter (MOLA) topography data show that rampart crater morphologies may be ubiquitous in the northern plains. If rampart ejecta blankets form in the present epoch, the subsurface volatile entrainment-fluidization model must be viable with solid ice.

3.3.1 Shock Melting of Subsurface Ice

The zones of melting and vaporization are related to the peak impact pressure and the decay profile of the shock wave as it propagates into the ground. In an impact event, the decay of the hemispherical shock front is usually described by

$$P(r) = P_0(r/r_c)^{-n} \tag{3.2}$$

where r is the radial distance from the impact point and P_0 is the peak shock pressure, which occupies a nearly hemispherical zone with radius r_c, and n depends on the impact velocity and target material [*Ahrens and O'Keefe*, 1987]. The projectile and target materials will vaporize or melt upon release from critical shock pressures in approximately hemispherical zones beneath the impact point [e.g., *Ahrens and O'Keefe*, 1972; *Pierazzo et al.*, 1997; *Pierazzo and Melosh*, 2000]. For most planetary impact conditions, the isobaric core radius

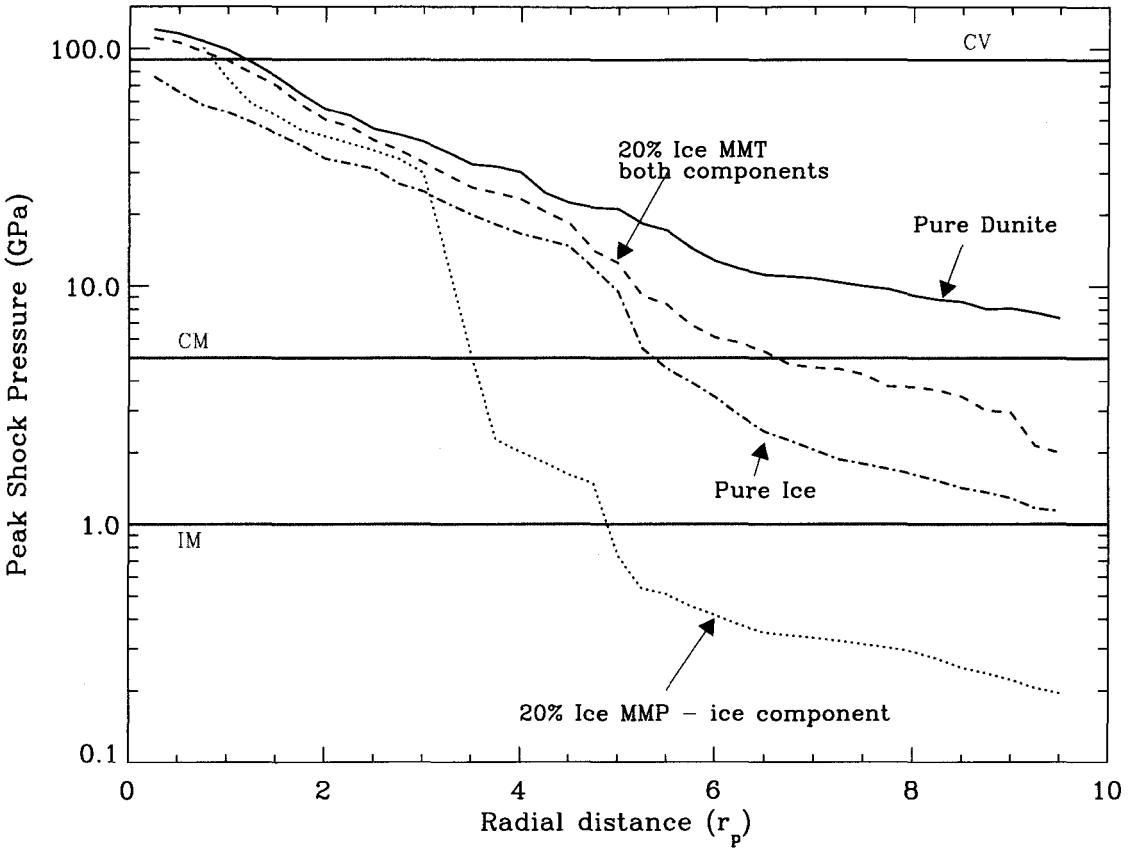

Figure 3.3: Shock pressure decay profiles for different target materials and cell thermodynamic options. The critical pressure for incipient (IM) and complete (CM) melting and (CV) complete vaporization of H_2O are noted with horizontal lines.

r_c is approximately the projectile radius [*Pierazzo et al.*, 1997].

Shock wave decay profiles from the Martian impact simulations are shown in Figure 3.3 for different target compositions and cell thermodynamics options. The profiles are derived from the peak pressure experienced by tracer particles located off the impact axis, between -40 and -70° from horizontal, to average over several mixed cells at a given r, away from any edge effects in the mesh. For a 10 km s^{-1} impact by a dunite projectile, the peak shock pressure is 120, 119, and 76 GPa in a pure dunite target, $20\%_{vol}$ ice-rock mixture, and pure ice target, respectively.

Table 3.3. Far field shock profile decay exponent n ($r > 6\ r_p$), where $P(r) = P_0(r/r_p)^{-n}$, and radial location of critical pressures for incipient melting (IM), 0.6 GPa, and complete melting (CM), 5.5 GPa.

Simulation	n	r_{crit}-CM (r_p)	r_{crit}-IM (r_p)
Pure dunite	1.1	[14]	[59]
Pure ice	2.0	(5.5)	10
$20\%_{\text{vol}}$ ice-mixture MMT	2.3	6.8	13.7
$20\%_{\text{vol}}$ ice-mixture MMP2-ice component	1.6	(3.7)	(4.7)
$20\%_{\text{vol}}$ ice-mixture MMP2-dunite component	1.9	[9.7]	[22]

Parentheses emphasizes r_{crit} is not on the $> 6\ r_p$ portion of the decay profile corresponding to tabulated n; see Figure 3.3. Brackets denote radius where pressure decay in pure rock crosses critical pressures for ice.

The shock decay profiles in Figure 3.3 correspond to a pure dunite target (solid line), a $20\%_{\text{vol}}$ ice-rock mixture with the MMT cell thermodynamic model (dashed line), a pure ice target (dash-dot line), and the ice component in a $20\%_{\text{vol}}$ ice-rock mixture using the MMP2 model (dotted line). The rock component decay profile in the MMP2 case (not plotted) is essentially identical to the pure dunite profile within 6 r_p and a little steeper beyond 6 r_p. The decay exponent, n, in the region beyond 6 r_p, is given in Table 3.3. In the region between 3-5 r_p, the ice and ice-rock mixture decay profiles show markedly steeper decay ($n = 5 - 6$) associated with the zone of shock melting.

The shock pressures required for incipient melting, complete melting and complete vaporization upon release to 6 mb is noted in Figure 3.3 by the horizontal lines, shown at average values of 1 and 5 GPa (Table 3.2). Note that about 50% of the ice is vaporized upon release from about 30 GPa. The critical radii of the zones of IM and CM are given in Table 3.3. Because ice in the Martian regolith is likely to be contained within pore spaces or fractures of size less than the projectile size, which is comparable to the thickness of the shock front, the shock pressure experienced by both the rock and ice should be approximately equal. Therefore, the MMT simulation is probably the most realistic model for the Martian regolith, indicating that ice may be melted in a hemispherical zone of about 6.8 r_p. The MMP2 simulation probably underestimates the amount of melt, even if the ice were distributed in thick layers, because it falls below the amount of melt in a pure ice target. Thus, we consider the zone of complete melting to be bracketed by the critical radius for the pure ice and MMT simulations, 5.5-6.8 r_p. The range of partial melting is extensive in

these simulations, between 10-13.7 r_p.

In reality, the zone of melting is likely to be slightly smaller because the shock impedance of basalt on the Martian surface is probably lower than the dunite in the simulation (Figure 3.2) and the peak pressure in the impact will be slightly less. Also, oblique impacts, most commonly at $\Omega = 45°$ angles, decrease the peak shock amplitude by a factor of about $\sin(\Omega)$ [*Pierazzo and Melosh*, 2000]. Natural dissipative mechanisms not included in the simulations, such as pore spaces, heterogeneities, and partial melting of the rock component, will cause the shock to decay more rapidly. Nevertheless, these calculations show that it is possible to completely melt a large zone around the impact point. The entropy for vaporization is considerably larger than melting (Table 3.2), and the peak shock pressures for 10 km s^{-1} impacts is just above the critical pressure for complete vaporization. Hence, within 6 r_p, only $0.5\%_{\text{vol}}$ (1 r_p, Figure 3.3) is completely vaporized and about $13\%_{\text{vol}}$ (3 r_p) is within the critical radius for 50% vaporization (about 30 GPa). Thus, if any ice is present within 6 r_p, most of the mass will be completely melted rather than vaporized.

Previous estimates of the critical pressures for melting have been much higher. *Kieffer and Simonds* [1980] derived critical values of 3 GPa for incipient melting and 10 GPa for complete melting under terrestrial conditions, based on sparse H_2O shock data. *Ahrens and O'Keefe* [1985] report 7.6 and 10.8 GPa for IM and CM, respectively, at 70 K and 1 bar, and 6.2 and 9.6 GPa, at 263 K and 1 bar. These high values led *Boyce et al.* [1996] and *Boyce and Roddy* [1997] to conclude that shock-induced melting was not a feasible process for fluidization of ejecta on Mars. More recent theoretical H_2O equation of state developments by *Tonks et al.* [1997] derive much lower critical pressures, 0.4 and 3 GPa for IM and CM under terrestrial conditions [also refer to *Pierazzo et al.*, 1997]. Recent experimental work on the H_2O Hugoniot have proven that shock-induced melting occurs at very low pressures, about 0.6 and 3.0 GPa for IM and CM, under terrestrial conditions (Chapter 2). The *Tonks et al.* [1997] ANEOS formulation is in good agreement with the entropy on the Hugoniot, but the ANEOS Hugoniot is less compressible than the experimental data and future work will involve improving the low-pressure region of the H_2O ANEOS.

Therefore, if there is ice present in the Martian crust, it may be melted by an impact shock in a zone between 10-20 r_p (Figure 3.3). We use nominal critical values of 5 and 15 r_p for the zones of complete and partial melting to calculate the properties of ejecta blankets for 10 km s^{-1} impacts.

3.3.2 Projectile-crater Size Scaling

Successful fluidization of an ejecta blanket by entrainment of subsurface H_2O will depend on the relative volume of shock-induced melting to the excavated volume in the crater. Because the volume of the critical melting zones depends on the projectile size, we must establish the scaling relationships between the projectile size and final crater diameter. First, we consider the effect of target strength on the transient crater cavity. Figure 3.4 illustrates the excavated zone in relation to the projectile size for the two strength models listed in Table 3.1, Y_{strong} on the left and Y_{std} on the right. The tracer particles ($\times$) are shown at the noted dimensionless times, Ut/r_p, where U is the impact velocity and t is time. The excavation paths for tracers which are ejected from the transient cavity are shown with lines. The lines terminate at either the location of the mass element at the specified time or the location at the time when the density of the flow was small enough that the material was removed from the computation. Ideally, all the solid ejecta would continue to travel along approximately ballistic trajectories.

The target and projectile are pure dunite, with projectile sizes of r_p =250 m (top) and 500 m (bottom), spanning simple to complex final crater morphologies. The projectile is shown at the impact point for reference. The radii of hemispherical zones of complete and incipient melting of ice are shown, neglecting near surface effects, to stress that both strength models produce transient crater cavities smaller than the zone of partial melting. Ice-rock mixture effects on crater size and excavation will be discussed below. In Figure 3.4, the maximum depth of penetration corresponds to the bottom of the crater cavity shown in A-C, but the crater floor has begun to rebound from a maximum depth of 11 r_p, forming a final complex crater shape, in D.

The Y_{strong} simulations have shallower, paraboloid shaped, transient cavities compared to the deeper, nearly hemispherical, cavities for Y_{std}. The depth of excavation is deeper for Y_{std} by about 0.6 r_p, and the ejection angles are steeper by an average of almost 10°. Because the excavation flow is steeper, the uplifted rim of the transient cavity is higher in the weaker target. For the simulations in Figure 3.4A-C, the overturned flap of the uplifted rim is the location of the final crater diameter. The strength models used here are not optimized to investigate complex crater collapse, although with the Y_{std} model, the uplifted rim in Figure 3.4D will collapse to a final complex crater with radius 15-16 r_p.

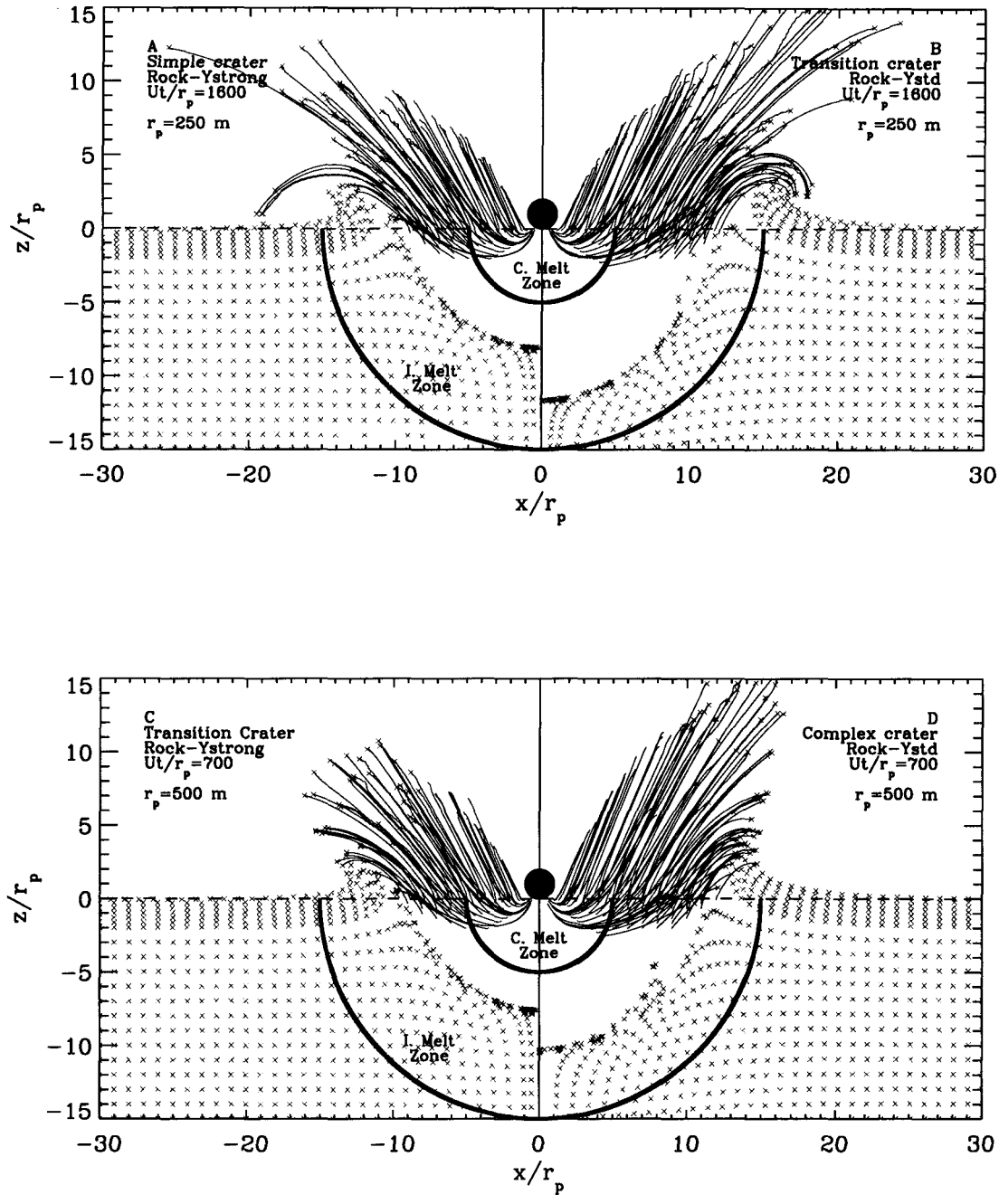

Figure 3.4: Crater excavation zones showing effect of target strength model. $r_p = 250$ m with Y_{strong} strength model (A) and Y_{std} model (B). $r_p = 500$ m with Y_{strong} strength model (C) and Y_{std} model (D). The transient cavity is deeper and the excavation flow field is steeper in the weaker material (Table 3.1).

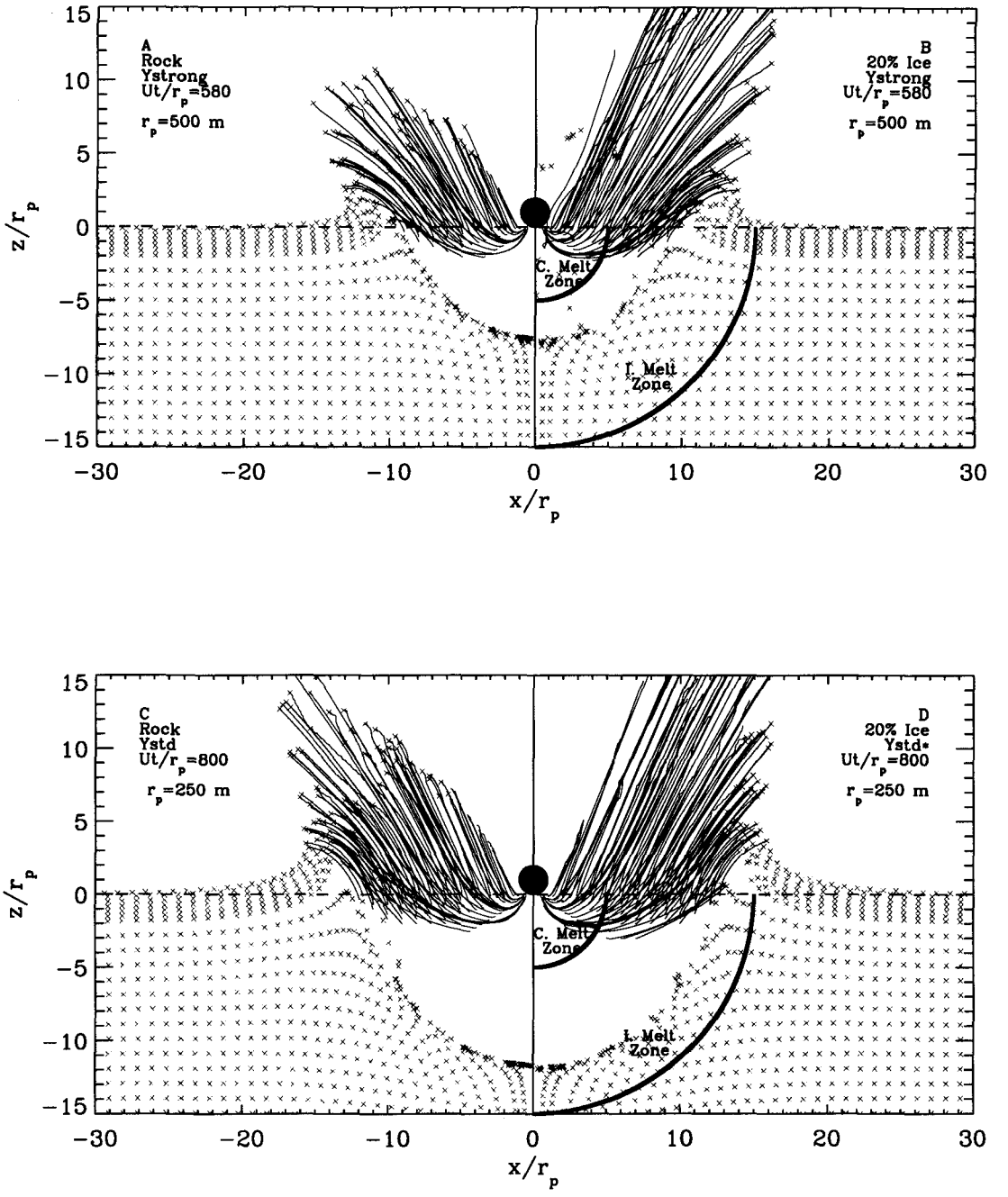

Figure 3.5: Crater excavation zones showing effect of ice-mixtures. Y_{strong} and $r_p = 500$ m simulations with pure rock target (A) and $20\%_{vol}$ ice-rock mixture (B). Y_{std} and $r_p = 250$ m with pure rock target (C) and $20\%_{vol}$ice-rock mixture (D). For transition and complex craters, the depth of penetration, depth of excavation, and diameter of the transient cavity differs by only a few tenths r_p between pure rock and a $20\%_{vol}$ mixture.

The excavation cavities for a $20\%_{\text{vol}}$ ice-rock mixture and pure rock target are shown in Figure 3.5. For both the Y_{strong} (top) and Y_{std} (bottom), the transient cavity and depth of excavation are very slightly larger when ice is present, by a few tenths of a projectile radii. The effect of the mixture is more significant in the Y_{strong} simulations than the Y_{std} runs. In strength-dominated simple craters ($D < 8$ km, see below), the depth of the transient cavity is deeper because the ice is more compressible. For the gravity-dominated craters shown in Figure 3.5 ($D > 8$ km), the difference in transient crater depth is negligible, but the excavation flow near the edge of the cavity is steeper by a few degrees in the ice-rock mixture, producing higher rim uplift (see section 3.4).

We find that the final crater diameter is much more sensitive to the strength model than the thermodynamic effects of an ice-rock mixture [also see, *O'Keefe et al.*, 2001]. In Figures 3.6 and 3.7, we present crater profiles, at the time of maximum depth of penetration and during transient crater collapse for $r_p = 500$ m and Y_{std} simulations, to show that the effects of a mixture and the thermodynamic model are second order effects on the final crater size. Figure 3.6 compares a pure rock case (left) with an ice-rock mixture using the favored MMT model (right). The excavation angles and rim uplift is only slightly steeper in the ice mixture. Figure 3.7 compares two simulations in an ice-rock mixture, with the MMP2 model (left) and MMT model (right).

We find that the size of the final crater as a function of projectile size is nearly the same in both pure rock and ice-rock mixtures for the average Martian surface strength. To discuss the ejecta properties for a range of crater sizes, we fit the Y_{std} simulations with π-group crater scaling laws [*Housen et al.*, 1983; *Melosh*, 1989]. The diameter of the transient crater is defined as the width of the excavated cavity at the pre-existing surface level. The final crater diameter is the distance between the uplifted rims for simple craters and across the final crater cavity for complex craters. Three simulations with Y_{std} were run to long times sufficient to determine the final crater size with r_p =50, 250, and 500 m, shown in Figure 3.8.

The diameter of the transient crater, D_{Tr}, is described by

$$D_{\text{Tr}} = \pi_D \left(\frac{m_p}{\rho_t} \right)^{1/3} \tag{3.3}$$

where m_p is the mass of the projectile and ρ_t is the density of the target surface. In the

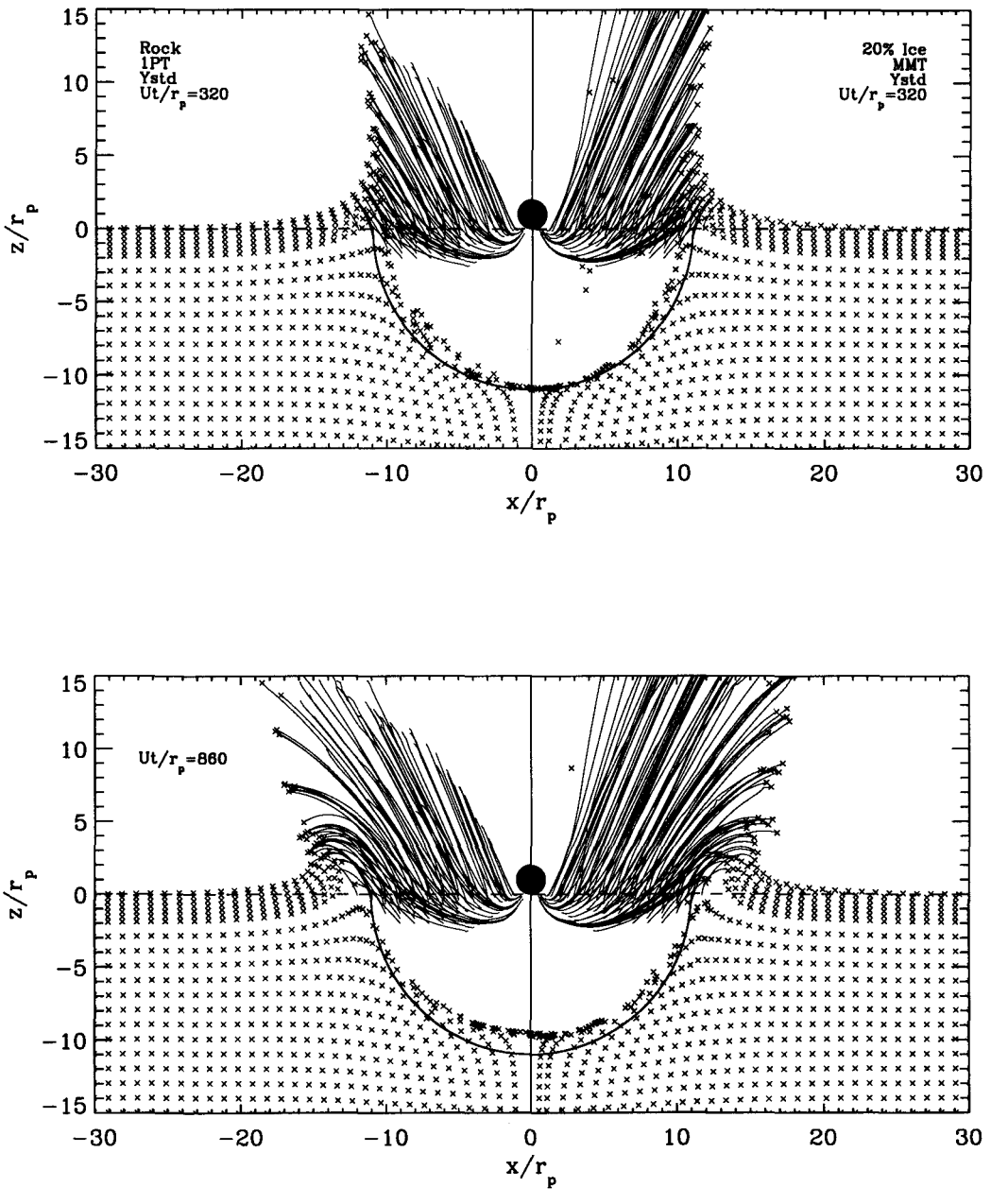

Figure 3.6: Crater excavation zones in rock (left) and 20%$_{\text{vol}}$ ice-rock mixture with MMT model (right) at time of maximum penetration (top) and during crater floor rebound (bottom). Hemisphere corresponds to maximum depth of transient crater (11 r_p, r_p=500 m).

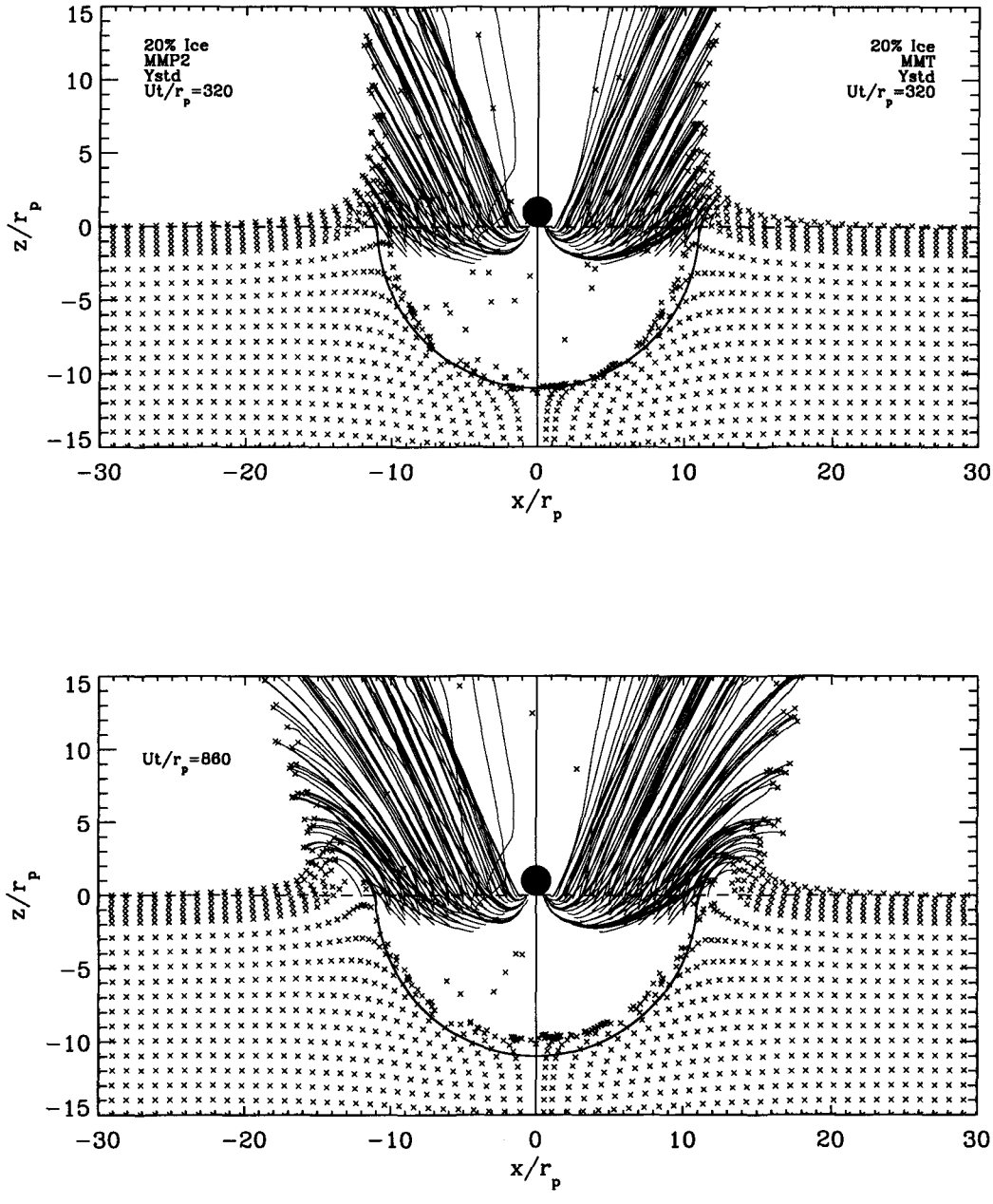

Figure 3.7: Crater excavation zones in a $20\%_{\text{vol}}$ ice-rock mixture, MMP2 model (left) and MMT model (right), at time of maximum penetration (top) and during crater floor rebound (bottom). Hemisphere corresponds to maximum depth of transient crater (11 r_p, r_p=500 m).

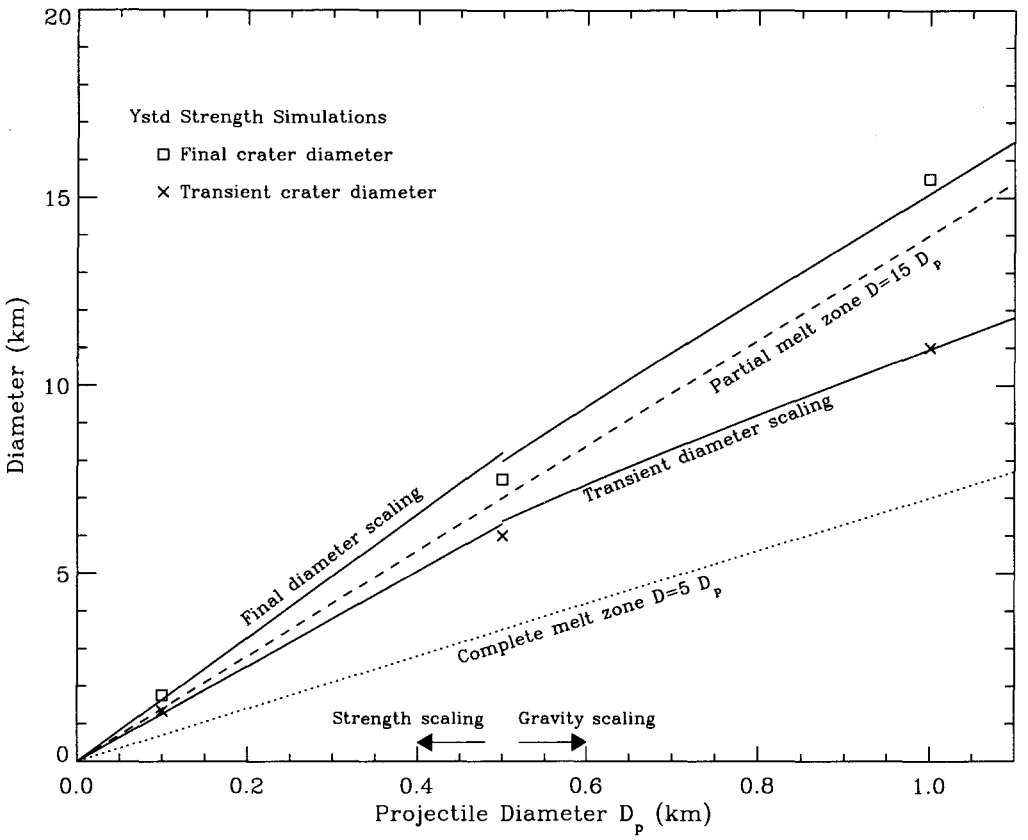

Figure 3.8: Transient (Eq. 3.3) and final crater diameters (Eqs. 3.10 and 3.12) as a function of projectile diameter for 10 km s^{-1} impacts and Y_{std} strength model (solid lines). Critial diameter of IM and CM zones (dotted lines) are about half and one crater diameter, respectively.

gravity regime, the dimensionless scaling variables are

$$\pi_D = C_D \pi_2^{-\beta} \tag{3.4}$$

$$\pi_2 = \frac{1.61 g D_p}{U^2} \tag{3.5}$$

where D_p is the diameter of the projectile, g is gravity, and U is the impact velocity. The π_D scaling coefficients for competent rock are $C_D = 1.6$ and $\beta = 0.22$ [*Melosh*, 1989; *Schmidt and Housen*, 1987]. In the strength regime, the dimensionless scaling parameters are

$$\pi_D = C_D' \pi_3^{-\beta'} \tag{3.6}$$

$$\beta' = \beta/(\beta - 1) \tag{3.7}$$

$$\pi_3 = \frac{Y}{\rho_p U^2} \tag{3.8}$$

where Y is the effective strength of the surface, ρ_p is the density of the projectile, and $C'_D = 280$ is fit to the simulations with r_p =50 and 250 m.

The transition between strength-dominated crater scaling, forming simple crater profiles, and gravity-controlled crater scaling, forming complex crater shapes, is a function of the effective strength of the surface and gravity. *O'Keefe and Ahrens* [1993] found that the transition diameter scales as

$$D^* = 9.0\frac{Y_{\text{eff}}}{\rho_t g}, \tag{3.9}$$

where Y_{eff} is the effective strength of the surface, ρ is the target density, and g is gravity. *Garvin and Frawley* [1998] determined the mean global transition diameter from simple to complex craters as $D^* = 8 \pm 0.5$ km using the MOLA dataset of depth to diameter profiles for 98 fresh craters. Using $g = 3.7$ m s^{-2}, $\rho_t = 2750$ kg m^{-3}, the effective strength of the surface is $Y_0 \sim 9$ MPa, corresponding to the Y_{std} case (Table 3.1).

From the simulations with r_p =50 and 250 m, the final crater diameter is given by

$$D_F^S = (1.25 \pm 0.05) D_{\text{Tr}}, \tag{3.10}$$

where the final crater has a simple bowl shape. Therefore, craters with $D < 8$ km are in the strength-dominated regime and Eq. 3.10 is used to determine the final crater diameter.

Following *Melosh* [1989] and his crater scaling program [copyright 1998, H. J. Melosh], gravity-dominated final crater diameters are calculated from the transient diameter, scaled to the Moon, where the transition to gravity scaling occurs at

$$D^*_{Mars} = \frac{(\rho g)_{Moon}}{(\rho g)_{Mars}} D^*_{Moon} \tag{3.11}$$

where $g = 1.67$ m s^{-2}, $\rho = 2700$ kg m^{-3}, and $D^* = 18$ km for the Moon. D^*_{Mars} is 8 km when the average surface density is 2750 kg m^{-3}.

Under impact conditions where the simple crater final diameter given by Eq. 3.10 is greater than the transition diameter, $D_F^S > D^*$, the final crater diameter is instead given by

$$D_F^C = \frac{(D_F^S)^{1.18}}{(D^*)^{0.18}}, \tag{3.12}$$

where the final crater shape will be complex.

The transient and final crater diameter scaling laws are shown in Figure 3.8 (solid lines) with the results from the cratering simulations with the Y_{std} model ($\times$, $\square$). The diameter of the zones for complete (dotted line) and partial melting (dashed line) are shown for comparison. Note that over the size range of interest for rampart craters ($D_F \lesssim 30$ km), the diameter of the zone of complete melting is about half the transient cavity and the diameter of the zone of partial melting is about equal to the final crater diameter.

If the effective surface strength were weaker, the transient cavity will be slightly larger, but gravity would limit the size of the cavity. We considered a target an order of magnitude weaker than the Y_{std} model. Figure 3.9 compares the crater size at the time of maximum depth of penetration and during transient crater collapse from a simulation with $r_p = 250$ m and the Y_{std} model (left) and Y_{weak}, where $Y_0 = Y_{max} = 10^6$ Pa. In the weaker target, the final diameter is about 9-10 km, and gravity inhibits growth of the transient crater cavity. Like the Y_{std} model, the excavated zone also lies within the range of partial melting of ice. Note that the excavation flow is steeper in the weaker material.

We find that, for average impact conditions on Mars, the zone of complete melting is about half the diameter of the transient cavity (excavated zone) and the zone of partial melting ($D \sim 15\ D_p$) is similar to the final crater diameter over the range of interest for rampart craters ($D < 30$ km). The excavated crater cavity will lie within the zone of partial melting for surface strengths within an order of magnitude of the mean effective strength on Mars.

3.4 Excavation and Rim Uplift

We have established that most of the ejected material will contain partial melt if any ice is present in the subsurface. To determine the distribution of water in ejecta blanket and the flow velocities, we need to characterize the excavation flow and ejection velocities.

To describe the excavated zone in the transient crater cavity, we use the Z-model [*Maxwell*, 1977], which has a simple analytic formulation for the excavation flow path, given by

$$r = r_e(1 - \cos\theta)^{1/(Z-2)} \tag{3.13}$$

where r and θ are polar coordinates, the $\theta = 0$ axis points vertically down and each r_e

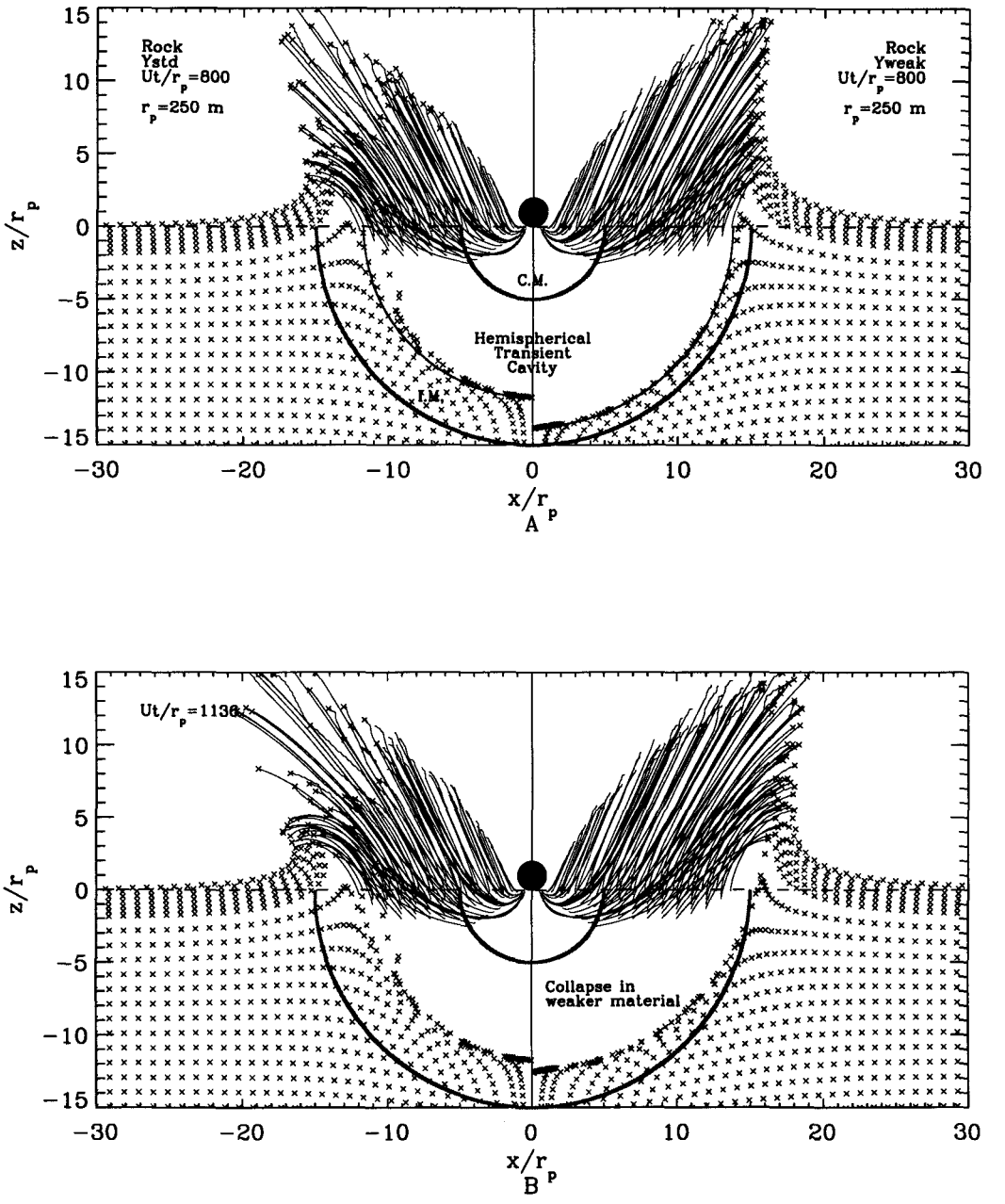

Figure 3.9: Crater excavation zone in pure rock with Y_{std} model (left) and Y_{weak} model (right) at time of maximum penetration (top) and during crater floor rebound (bottom), with $r_p = 250\ m$.

corresponds to a separate ejection streamtube. When the streamtubes are centered at the surface impact point, r_e is the ejection location at the original surface level with an ejection angle, α, given by

$$\alpha = \arctan(Z - 2). \tag{3.14}$$

$Z = 3$ is a previously used value that yields crater excavation flows that match detailed finite difference calculations similar to those presented above [*Maxwell*, 1977; *Croft*, 1980; *Melosh*, 1989]. The $Z = 3$ streamtubes are shown with CTH tracer particle flow histories in Figure 3.10A for the simulation with Y_{std} and $r_p = 250$ m (from Figure 3.5D).

While the limits of the excavated zone are well described by a $Z = 3$ streamtube centered at the surface, the paths within the flow are not. The ejection angles are much steeper, on average 57°, corresponding to $Z = 3.54$, shown in Figure 3.10B. With the larger value of Z, the depth of excavation is too deep, including mass which is displaced onto the transient crater wall.

The ejection angles decrease slightly from the impact point to the transient crater edge, which may be described by allowing Z to vary as a function of angle (θ) in the flow. Alternatively, *Croft* [1980] notes that constant Z streamtubes centered at an effective depth of Z-model flow, the EDOZ model, also gives a realistic description of the ejection process, especially in the outer region of the excavation cavity, which is of interest for the continuous ejecta blanket. The formulation of the EDOZ model is the same as the standard Z model (Eq. 3.13), but the flow field is offset in the vertical (z) direction.

We place the effective depth of flow at the center of the isobaric core of the shock wave, shown in Figure 3.10C. The center of the isobaric core from our simulations and *Pierazzo et al.* [1997] is about 0.5 r_p for 10 km s^{-1} impacts. The value of $Z = 3.3$ for the streamtube is fit to the ejection angles from the Y_{std} simulations (see below). The limit on the excavated zone is well matched by a bounding streamtube with $Z = 3$ for pure rock simulations and $Z = 3.1$ for 20%$_{vol}$ ice-rock mixtures. In this work, to calculate the ejecta distribution, we use the EDOZ model but truncate the streamtubes at the depth where excavation is observed in the simulations, shown in Figure 3.10C. Analytic formulations for flow volumes in the Z and EDOZ-models are presented in *Croft* [1980].

The ejection angles and velocities are shown in Figure 3.11 for Y_{strong} and Y_{std} runs with $r_p = 250$ m (Figure 3.4A, 3.5C,D). The ejection location, x_e, is scaled by the transient

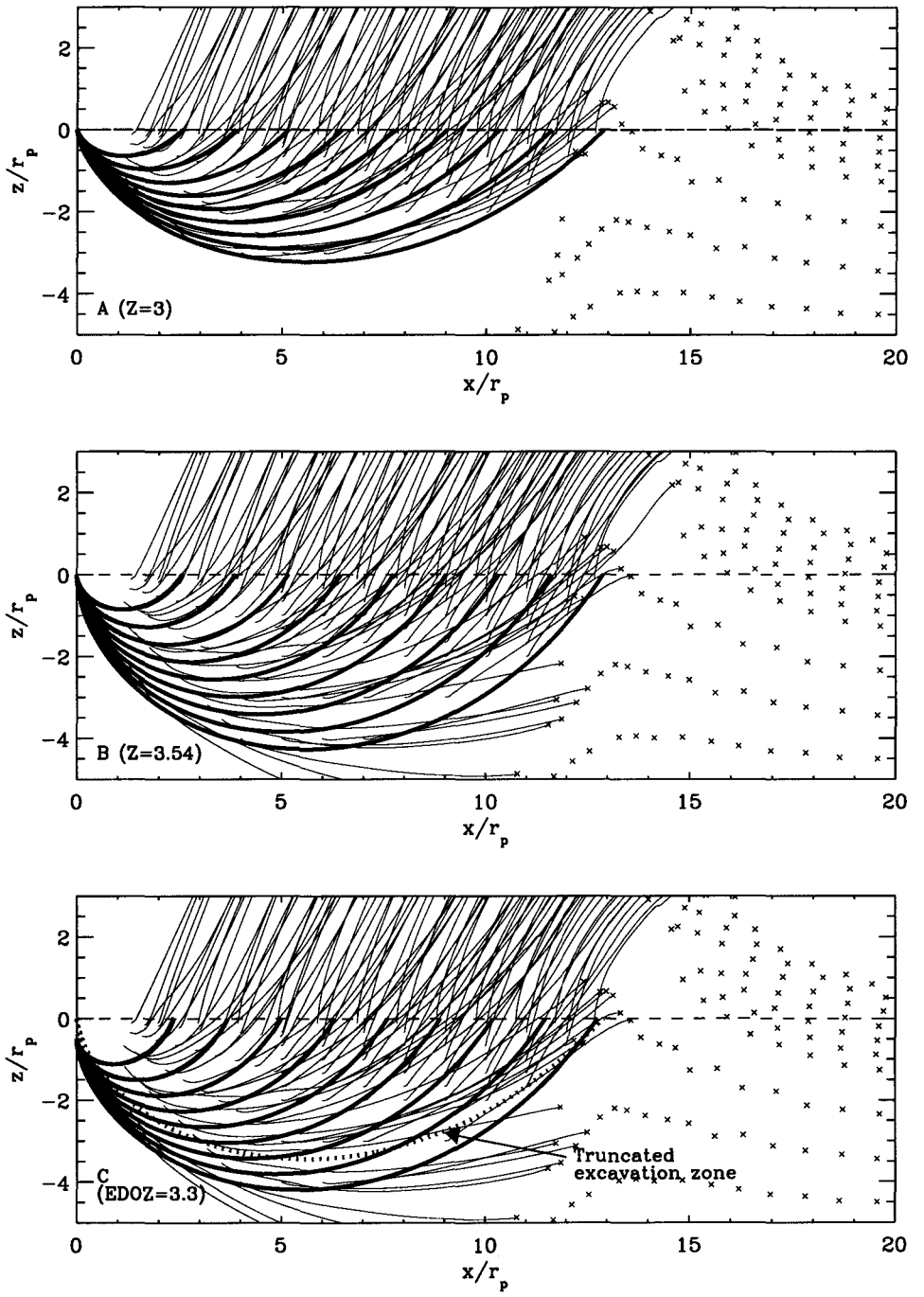

Figure 3.10: Excavation streamtubes for Y_{std} simulations. **A.** Standard Z-model, Z=3, flow is in good agreement with depth of excavation but underestimates ejection angles. **B.** Z=3.54 is a better match to ejection angles but overestimates excavation depth. **C.** EDOZ model centered at $d_{exc} = 0.5\ r_p$ with Z=3.3 is a good model for decrease in ejection angle from impact point to edge of transient cavity.

cavity in the pure rock case. Note that in the weaker strength model, the ejection velocities are slower. For a fixed impact velocity, a larger transient crater cavity forms in a weaker material, but the peak shock pressure decay scales with the projectile size. Thus, the peak shock pressure is smaller at the edge of the excavated cavity in a weaker material and the corresponding ejection velocities (U_x) are lower.

The ejection velocities, U_e (m s^{-1}), at the surface level follow a log-linear curve in the outer portion of the transient cavity, $x_e > 0.4\ R_{Tr}$, where

$$U_e = 10^{[c_1 + c_2(x_e/R_{Tr})]}. \tag{3.15}$$

For r_p = 250 m, c_1 = 3.246 and c_2 = −1.447 for Y_{std} (Figure 3.11A, solid line) and c_1 = 3.369 and c_2 = −1.402 for Y_{strong} (Figure 3.11E, solid line). The average ejection angles in all four simulations is about 55°, with a large scatter between 35-80°, although the peak ejection angles are larger in the weaker target. In the outer excavation zone, $x_e > 0.66\ R_{Tr}$, the median ejection angles are 48, 55, 57, and 57° for the Y_{strong} rock, Y_{strong} 20%$_{vol}$ ice, Y_{std} rock, and Y_{std} 20%$_{vol}$ ice cases, respectively (Figure 3.11B and F). The effect of the ice-rock mixture on the ejection angles is more pronounced in the Y_{strong} model. The ejection angles and velocities are similar in the r_p = 50 and 500 m runs, where c_1 = 3.168 and c_2 = −1.407 and c_1 = 3.275 and c_2 = −1.463, respectively.

The ejection angles are fit with an EDOZ model, solid lines in Figure 3.11B and F, where Z = 3.1 and 3.3 for the Y_{strong} and Y_{std} models, respectively, and the depth of flow is 0.5 r_p. The ejecta range and horizontal velocity component at the time of emplacement, U_x, is calculated from $U_e(x_e)$ and $\alpha(x_e)$ assuming ballistic trajectories. The corresponding U_x is shown in the near and far ejecta field in Figure 3.11C,D,G,H.

For comparison, the surface Z = 3 case with constant $\alpha(x_e) = 45°$ is shown with dashed lines in Figure 3.11B-D, F-H. Note that the 45° ejection angle overestimates the ejecta blanket flow velocities.

The effect of an ice-rock mixture on the ejection angles and velocities is relatively small for 20%$_{vol}$ ice and negligible for 10%$_{vol}$ ice. The decrease in effective strength is small in the strength mixing model, scaling linearly with ice volume fraction. The ejection velocities and angles are sensitive to the order of magnitude of the total strength (Y_{std} vs. Y_{strong}), which, in turn, should be related to the ice content in a more sophisticated geologic yield

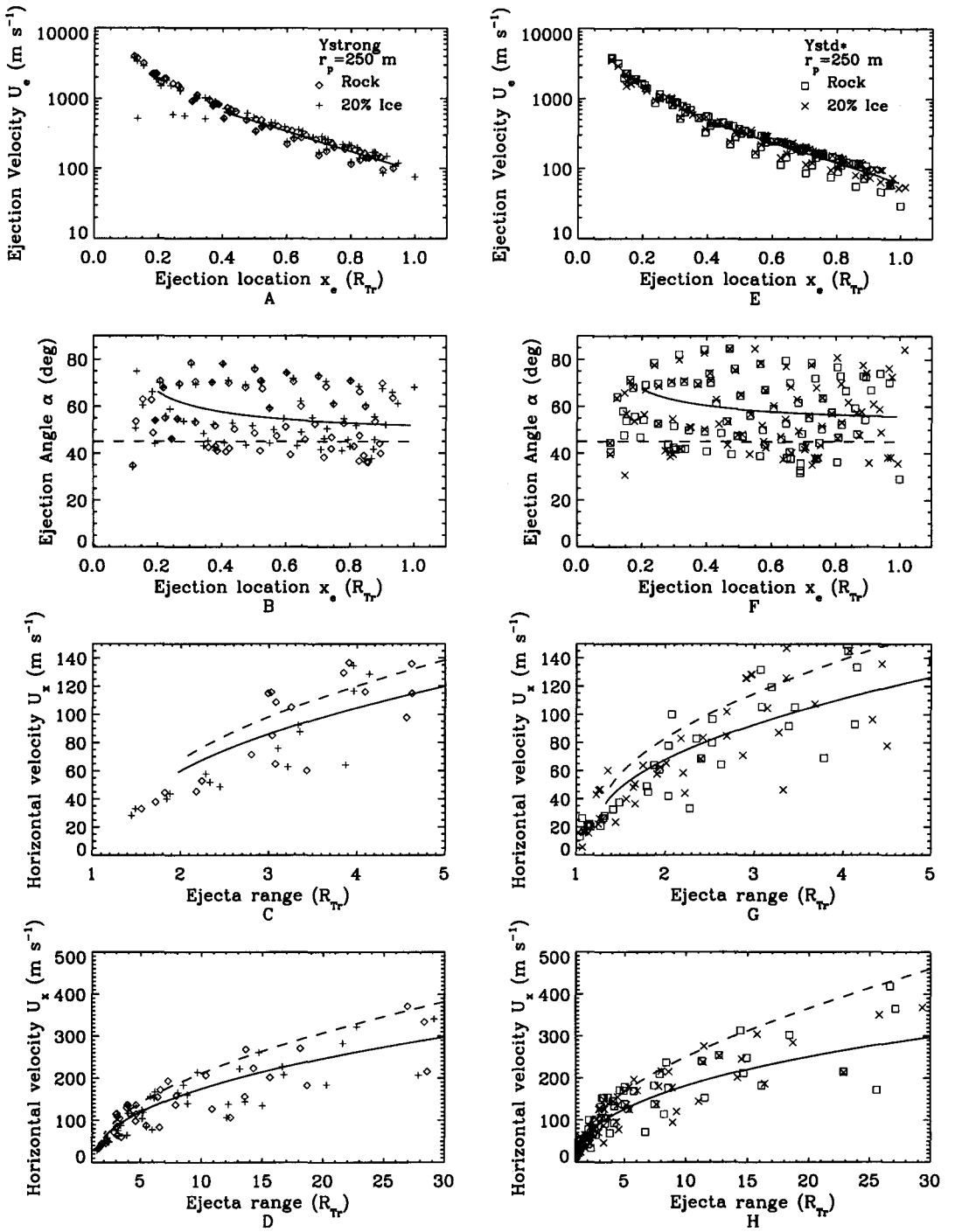

Figure 3.11: Ejection velocities and angles with r_p = 250 m and Y_{strong} (left) and Y_{std} (right) strength models scaled to transient crater radius. In weaker targets, ejection velocities are lower at transient cavity edge and ejection angles are higher. Ejection angles and emplacement velocities are fit with EDOZ model (see text and Fig. 3.10C), solid line. Previous Z=3 model, dashed line, underestimates ejection angles and overestimates horizontal ejecta flow velocities.

model than included here.

Because the excavation flow angles are slightly steeper, the uplifted rim of the transient crater is larger in weaker materials. In addition, the rim uplift is sensitive to ice content. Figure 3.12 compares the uplifted rim for four simulations: r_p = 250 and 500 m with Y_{std} and Y_{strong} models. The rim uplift and horizontal distance are scaled by the transient crater radius, R_{Tr}, of the pure rock case. In the strength regime, the uplifted rim and overturned flap define the final crater diameter. In the simulations, the ratio of the radius of the excavated zone to the final crater radius is larger in the Y_{std} case compared to the Y_{strong} runs. The final location of the overturned flap in the Y_{std} runs is between 1.3-1.4 R_{Tr} (Figure 3.12A,C). The overturned flap is displaced farther in the Y_{strong} runs, located between 1.4-1.5 R_{Tr} (Figure 3.12B,D).

The mean ejection radius is 0.74 vs. 0.69 R_F for the Y_{std} and Y_{strong} cases, respectively. The corresponding total volume of ejecta is 23% larger in the weaker surface. Therefore, the ejecta blanket volume is very sensitive to the radius of the ejection zone, which is dependent on the effective strength of the surface. In general, for a given crater diameter, the ejecta blanket volume will be larger for weaker surface lithologies because of the steeper excavation flow.

For a given strength model, the presence of ice raises the rim uplift by a few percent, resulting in steeper rim profiles and moving the location of the overturned flap further away from the crater center (as much as 0.1 R_{Tr} in Figure 3.12D). The transient rim uplift with Y_{std} is up to 0.1 R_{Tr} larger compared to the Y_{strong} simulations. Also, because the uplift angles are steeper, the original location of the material at the rotation point of the overturned flap is closer to R_{Tr}. Note the location of the rotation of the overturned flap does not change at late times for Y_{std}(Figure 3.12A,C). In the stronger surface, however, the location of flap rotation moves about 0.1 R_{Tr} farther from the crater center at late times.

The uplifted ground surrounding the crater may not have a stable slope. In Figure 3.12A, the uplifted rim around the crater in an ice-rock mixture has a slope of 50-70°measured from the horizontal, beyond the angle of repose of heavily fractured material (e.g., about 45° for angular pebbles). In this case, the rim may partially collapse, contributing to the volume of the ejecta blanket. In comparison, under the same impact conditions, the crater formed in a pure rock target has uplift angles of 37-65° near the rim. The rock Y_{strong} simulations in

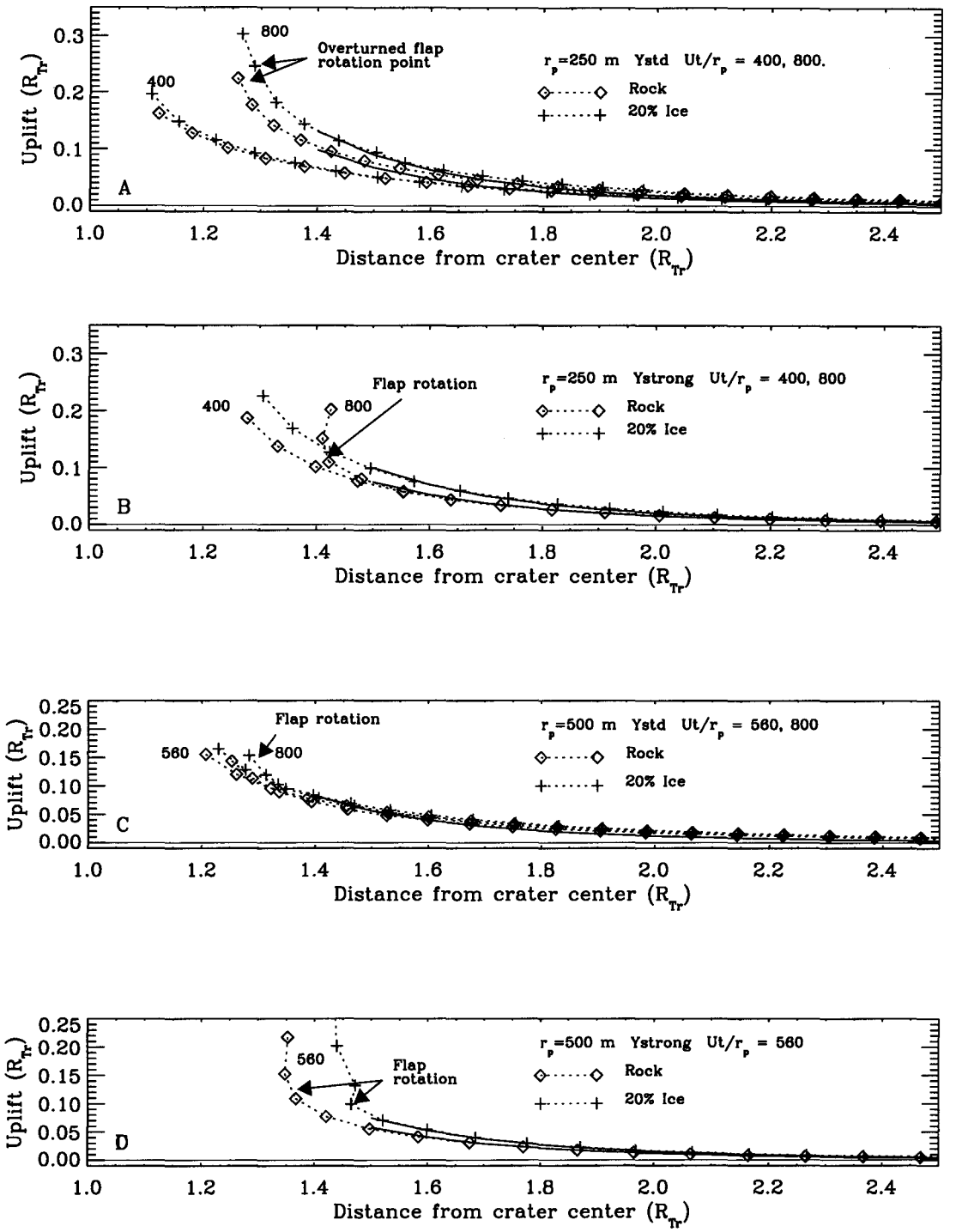

Figure 3.12: Transient crater rim uplift for $r_p = 250$ m, with Y_{std} (A) and Y_{strong} (B), and $r_p = 500$ m with Y_{std} (C) and Y_{strong} (D) strength models. Horizontal location is scaled to transient crater radius of rock simulation. Uplifted rims are fit with Eq. 3.16, solid lines.

Figure 3.12B has an uplift angle of about 22° just beyond the overturned flap. We conclude that ejected material deposited on the uplifted rims of craters in an ice-rock mixture is likely to be unstable.

The overall uplifted zone is well fit with a power law decay of the form

$$z = A_z R_{Tr} (x/R_F)^{-5.5} \tag{3.16}$$

where z is the magnitude of the uplift at the range x, R_{Tr} is the transient crater radius, and R_F is the radius of the final crater. The uplifted rim fits are shown as solid lines in Figure 3.12, and the value of A_z varies from .16-.07 in Figure 3.12A-D. There is noticeable uplift of the surrounding terrain to about 2.5 R_{Tr}. Until more realistic strength models are investigated, a working value of $A_z = 0.1$ is a good match to the simulations.

For complex craters, the properties of the ejecta blanket depends critically on the specifics of the crater collapse, which are still poorly understood [*Melosh and Ivanov*, 1999; *O'Keefe and Ahrens*, 1999]. The Y_{std} case with r_p = 500 m (Figure 3.12C) produces an uplifted rim with diameter about 15 km, but the rim collapses to a final crater diameter of about 19 km, shown in Figure 3.13. When the crater rim collapses, some of the ejected material from the transient cavity collapses back into the final crater cavity, although some of the ejecta may flow to the surrounding terrain before the transient rim collapse occurs. Note that the first ejecta lands before the rim collapses in Figure 3.13. Although the strength of each component is initially identical and the MMP2 model produces little shock melting (Figure 3.3), the collapsed crater profiles are different in the rock vs. the mixture, implying that the difference in compressibility is important for final crater shape, in addition to strength and phase change effects. In a Y_{strong} simulation, however, a r_p = 1000 m impact produces a final crater diameter of 24 km which does not collapse.

3.5 Ejecta Properties and Topography

We are interested in the quantity and distribution of liquid water in the ejecta blanket for a given crater diameter. We use the scaling law developed from the simulations for the mean effective surface strength (Figure 3.8), the EDOZ excavation model, and the ejection velocities from the simulations (Figure 3.11). The fraction of melted ice in each excavation streamtube is calculated from the volume of material within the completely melted and

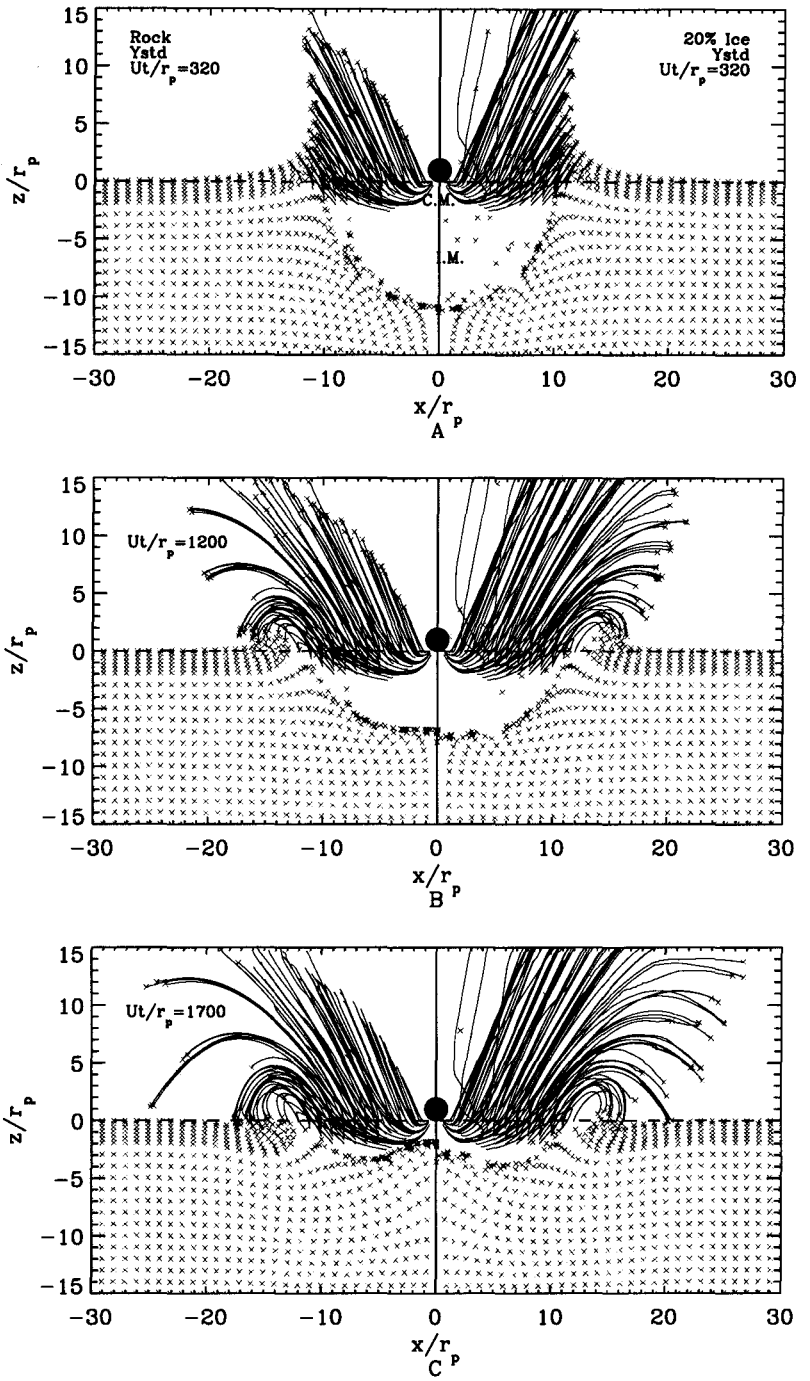

Figure 3.13: Complex crater profiles showing excavation zones in pure rock (left) and $20\%_{\text{vol}}$ ice-rock mixture (right) at time of maximum penetration (A) and during crater collapse (B, C). Simulation parameters were $r_p = 500$ m, Y_{std}, and MMP2.

partially melted zones. The volume fraction of liquid in the partially melted zone as a function of distance from the impact point is extrapolated linearly between the critical radii for complete melting and incipient melting (refer to Chapter 2).

Figure 3.14 shows the results for ejecta emplaced around craters with 2.5 and 5 km diameters, corresponding to the ejecta properties for the Y_{std} simulations. The excavation streamtubes are solid in the zone of complete melting and dotted in the region of partial melting. The rim uplift is given by Eq. 3.16 with $A_z = 0.1$, which is appropriate for the strength-dominated regime.

The rim uplift and ejecta blanket thickness, at the location of ejecta emplacement, are shown in Figure 3.14B,F. The horizontal component of the ejection velocities are shown in the near field (within 5 R_F) and the fraction of melted ice, f_m, is given as a function of emplacement range. The excavation model is consistent with simulations run with near-surface ice in the range $\phi_0 = 0 - 20\%_{vol}$, thus the volume fraction of liquid water in the ejecta blanket is $f_m \phi_0$.

The ejecta blanket thickness (solid line in B, F) does not take into account any increase in porosity from the comminution of the material, so it may be considered a lower limit. If the rim uplift produces slopes which are unstable (up to 70° in Figure 3.12), the ejected material just beyond the uplifted rim may slide and collect on the flatter surface. The dashed line shows the thickness of the ejected material if the total volume emplaced within 3 R_F is collected in an annulus between 1.5-3.0 R_F. Most distal ramparts are located at about 3 R_F [*Mouginis-Mark*, 1978] and the recent MOLA data indicate that the near-rim material collects at about 1.5 R_F (see below). The thickness of the ejecta annulus is about 4 and 13 m for the 2.5 and 5 km diameter craters, respectively.

Figure 3.15 shows the same ejecta blanket properties for 10 and 20 km diameter craters. Here, Eq. 3.16 overestimates the uplifted rim around a 20 km complex crater, where the transient crater rim is expected to collapse. In gravity-dominated case, the ballistic range of some of the material ejected from the transient cavity lies within the final crater cavity. Exclusion of this material results in a thinner ejecta blanket annulus around the 20 km diameter crater, with a thickness comparable to the 10 km crater. The thickness of the ejecta annuli are 25 and 22 m for 10 and 20 km craters, respectively.

If the transient crater does not collapse during the formation of 10-20 km diameter craters, we may estimate the ejecta blanket thickness using the strength scaling law ex-

trapolated to larger craters. Figure 3.16 presents the ejecta blanket properties for 10 and 20 km diameter craters assuming strength-dominated scaling between the transient cavity and final crater diameters (Eq. 3.10). In these figures, the plotted uplift of the surrounding terrain corresponds to the transient crater rim uplift (Eq. 3.16). The 10 km crater is near the simple to complex transition diameter so there is very little difference in the ejecta annulus thickness, now at 28 m. The 20 km crater ejecta annulus thickness, however, is almost double under the strength-scaling regime, at 42 m, because most of the excavated material is ejected outside the final crater rim. The difference between the ejecta thickness using strength vs. gravity-controlled crater scaling illustrates the sensitivity of ejecta blanket properties to the scaling model and, hence, to the strength model of the surface.

Figures 3.17 and 3.18 present the MOLA topography for two fresh rampart craters, $D_F = 9$ and 20 km, craters labeled I and J by *Garvin et al.* [2000]. The inner region of the ejecta blanket has a thickness of > 100 m over the surrounding topography compared to 10's m in the outer ejecta blanket. The step in the thickness of the ejecta blanket occurs at about 2.5-3.0 R_F from the center of the crater.

Garvin et al. [2000] note that the rim height is higher and crater cavity deeper than expected compared to Martian craters with normal ejecta facies. *Garvin and Frawley* [1998] find that rampart crater ejecta blankets appear to have volumes in excess of the excavated crater cavity estimates for impacts into pure rock surfaces. With our model, the volume of the ejecta blanket is consistent with the crater formation process. The larger ejecta blanket volume may be related to larger transient cavity size in weaker materials. In addition, the steep ejection angles place more mass of ejecta closer to the crater rim. The higher rim uplift (and ejecta fluidization) encourages ejecta to collect on the flatter terrain around the crater rim. In dry ejecta blankets, this process would produce hummocky terrain, but in fluidized ejecta blankets, the ejecta may continue to flow, forming the rampart features.

The model ejecta blanket volumes are comparable to the MOLA ejecta topography. For the 9 km diameter crater in Figure 3.17, the rim uplift model (solid lines, Eq. 3.16) is in good agreement with the MOLA data, where the individual measurements are shown with + and the profile is repeated, and offset, using a solid line. The dashed line is the thickness of the ejected material at the location of emplacement, with no additional porosity. Arrows note the edge of the rampart ejecta layers identified by *Garvin et al.* [2000].

The volume of ejecta emplaced between 1-3 R_F, collected in an annulus between 2-3 R_F,

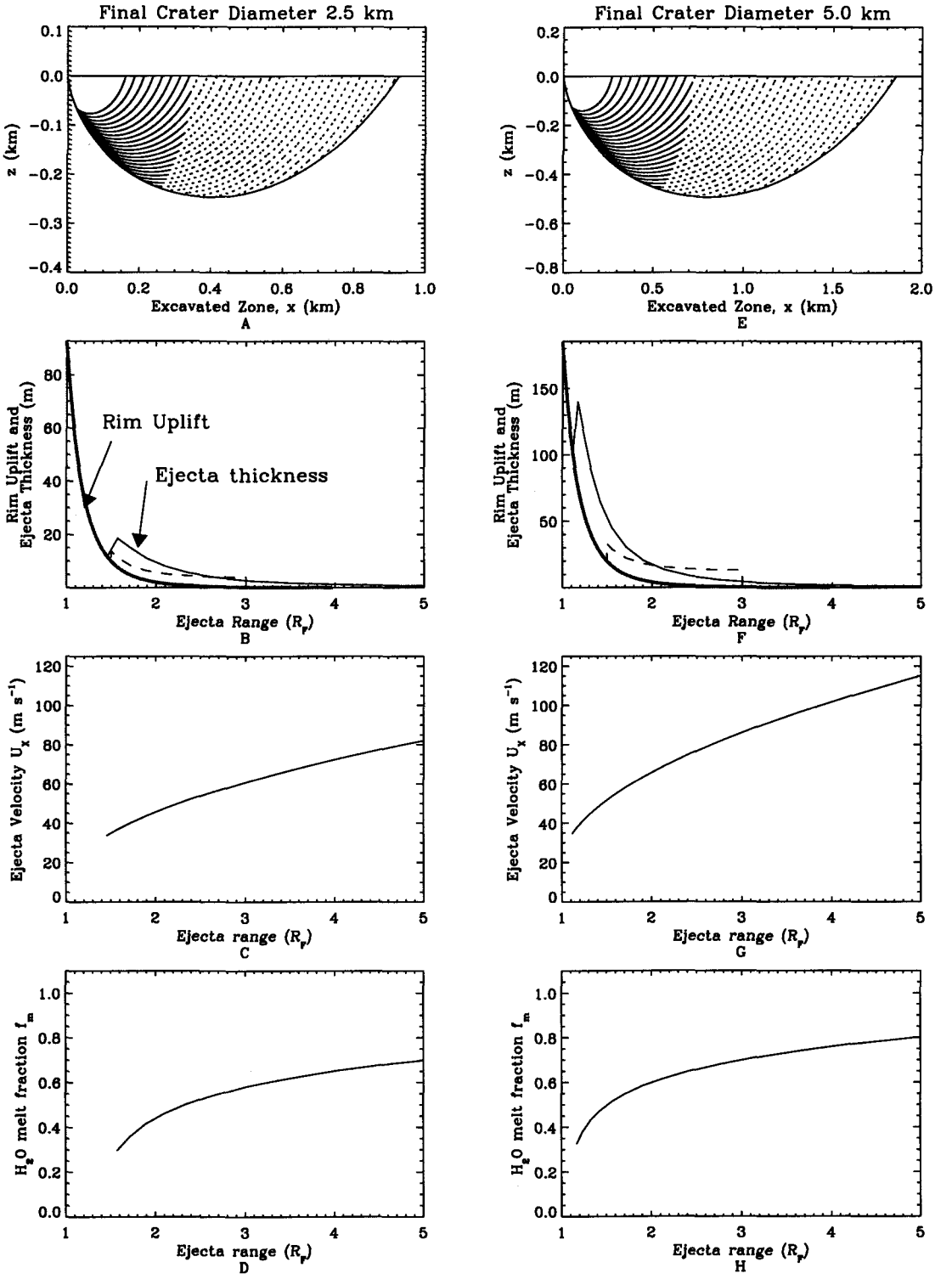

Figure 3.14: 2.5 and 5 km diameter crater excavation model. **A, E**: EDOZ model streamtubes showing cross section of excavated zone. Solid and dashed lines denote volume of material within CM and IM zones, respectively. **B, F**: Cross section of crater rim uplift (thick solid line), initial ejecta thickness (thin solid line), and ejecta thickness in 1.5-3.0 R_F annulus (dashed line). **C, G**: Horizontal velocity of ejecta at time of emplacement. **D, H**: Fraction of shock-induced melt.

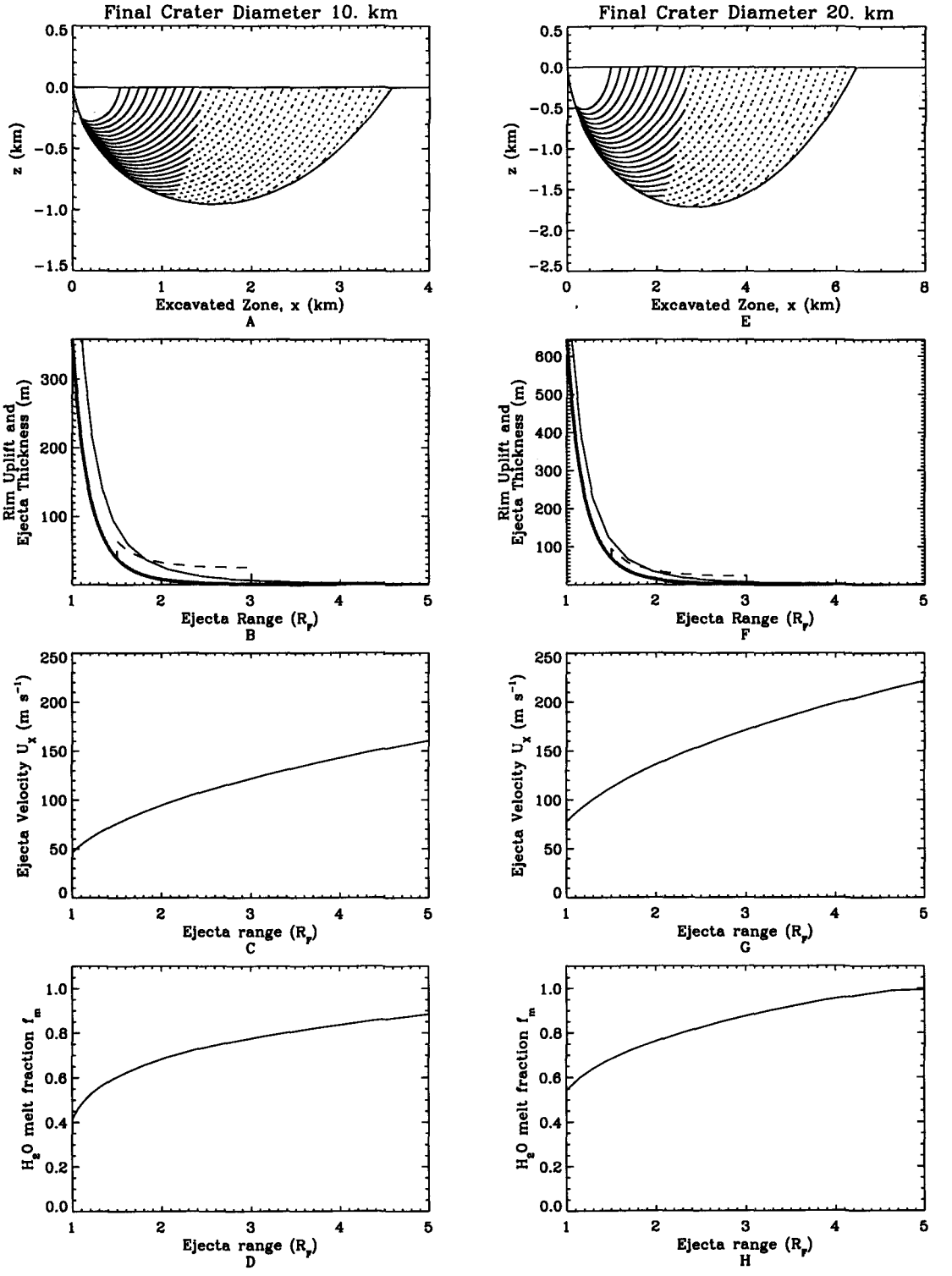

Figure 3.15: 10 and 20 km diameter crater excavation model using gravity scaling (Eq. 3.12). **A-H**: see Fig. 3.14 caption.

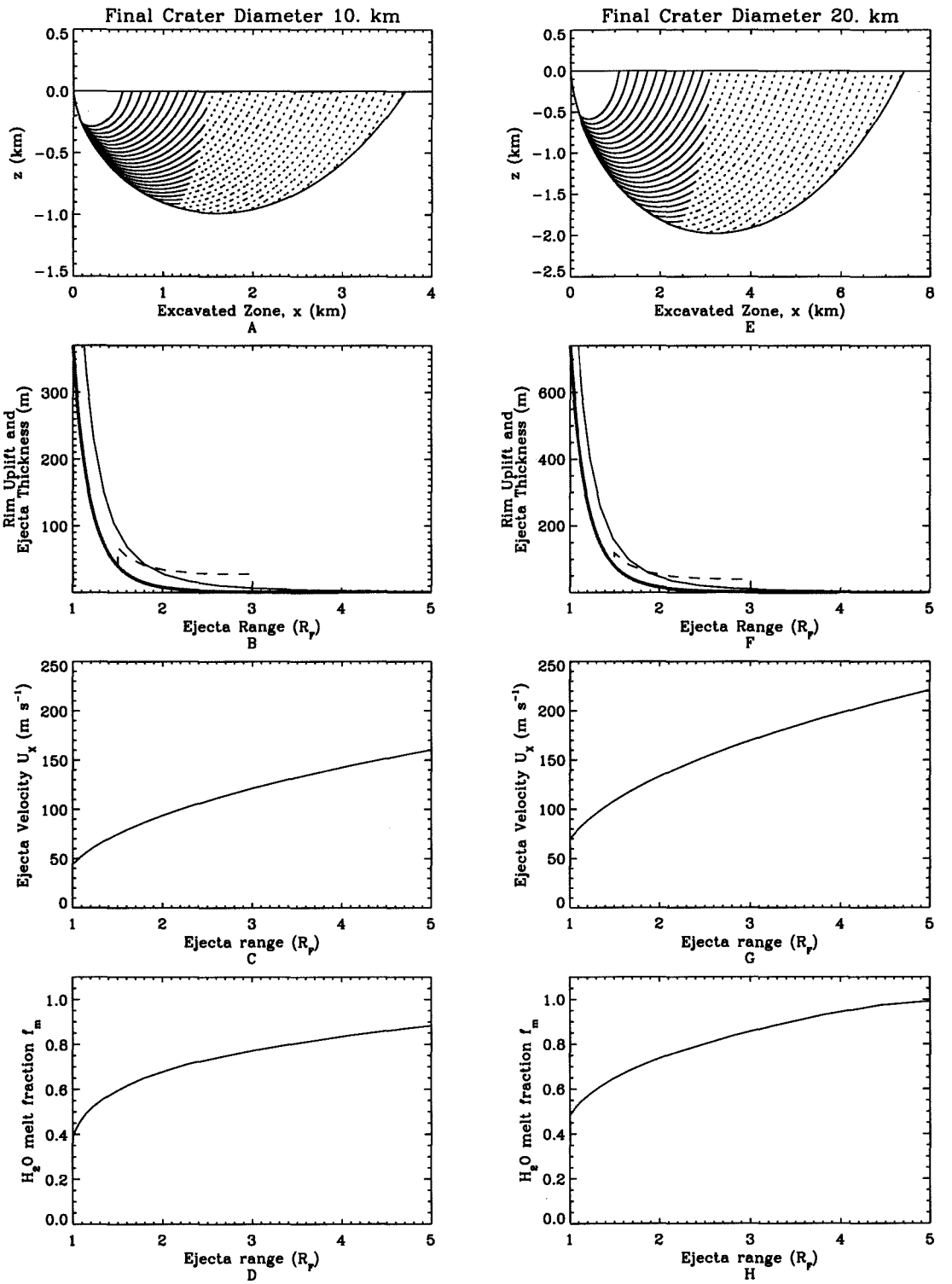

Figure 3.16: 10 and 20 km diameter crater excavation model using strength scaling (Eq. 3.10). **A-H**: see Fig. 3.14 caption.

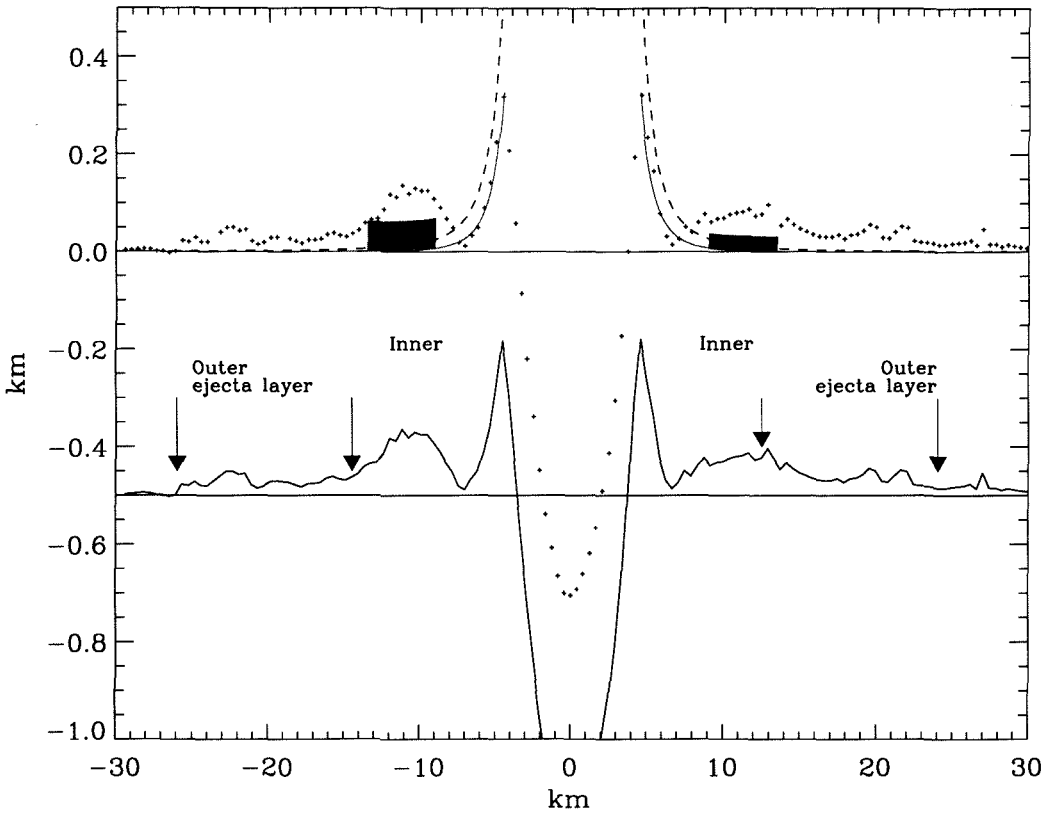

Figure 3.17: Comparison between ejecta model and MOLA topography (+) of fresh multiple-layer rampart crater with $D_F = 9$ km. Uplifted rim (Eq. 3.16) model (solid line) is a good match. Model ejecta thickness at location of emplacement (dashed line) likely flows to the flatter terrain. Boxes show equivalent thickness of ejecta in annulus 2-3 R_F with 50% (left) and 0% porosity (right). MOLA profile repeated in offset with arrows marking inner and outer edges of ejecta layers.

is shown as filled boxes with 50% porosity on the left and 0% porosity on the right. The amount of liquid water in the ejecta blanket within 3 R_F corresponds to about half the total ice content in the crust and the horizontal flow velocity ranges from 50-125 m s^{-1}, for typical impact conditions (Figures 3.15D and 3.16D). We interpret the dip in topography at the base of the rim to be pile-up of ejecta which slid down the uplifted rim (see below).

The 20 km diameter crater in Figure 3.18 has lower rim uplift compared to the transient crater uplift model (Eq. 3.16) as would be expected in gravity-dominated craters with collapsed rims. Using gravity-scaling for a 20 km crater (Figure 3.15) the ejecta blanket thickness at the emplacement location (dashed lines) and equivalent thickness in two annuli

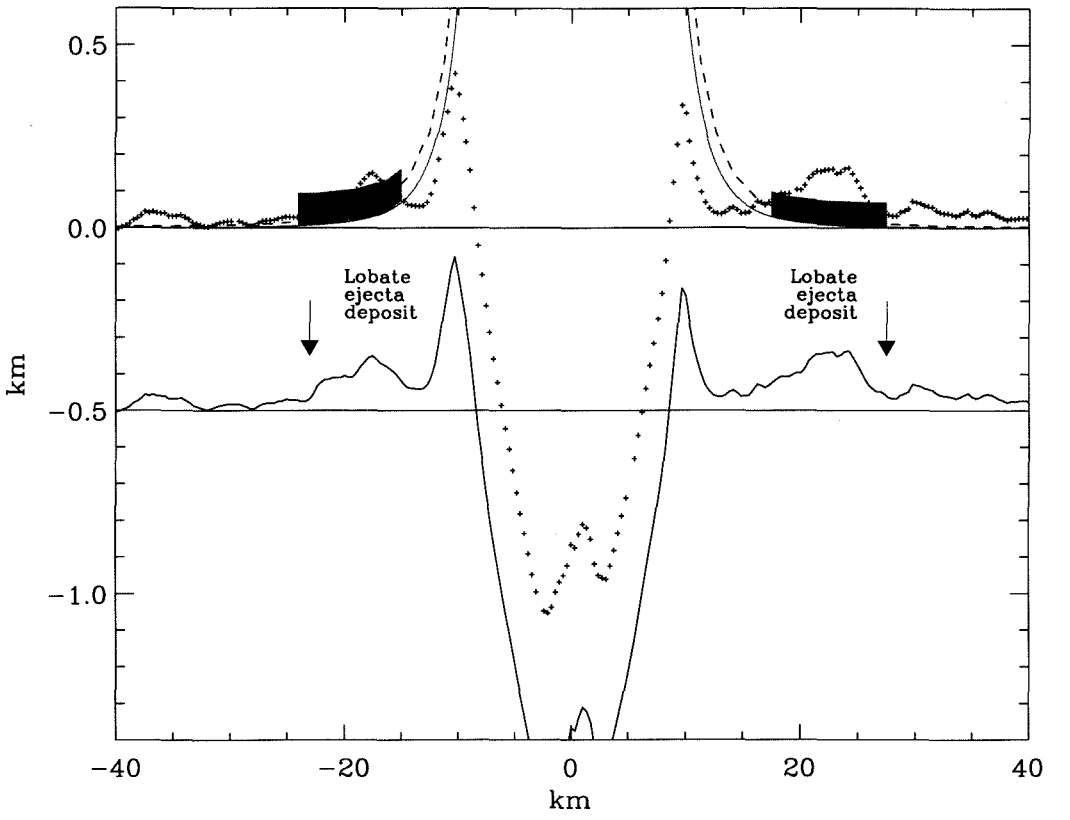

Figure 3.18: Comparison between ejecta model and MOLA topography (+) of fresh rampart crater with $D_F = 20$ km. Mismatch from model uplifted rim (Eq. 3.16) (solid line) implies partial crater collapse. Model ejecta thickness at location of emplacement (dashed line) likely flows to the flatter terrain. Boxes show equivalent thickness of ejecta in 1.5-2.4 R_F annulus with 0% porosity (left) and 1.75-2.75 R_F annulus with 0% porosity (right). MOLA profile repeated in offset with arrows noting edge of lobate ejecta blanket.

are shown in Figure 3.18. The mass of ejected material, with no additional porosity, is comparable to the observed volumes of the lobate deposits.

3.6 Discussion

3.6.1 Interpretation of Rampart Crater Morphologies

The ice-rock mixture excavation model presented here, where ice in the excavated crater cavity will partially melt and weaker targets produce higher ejection angles and lower ejection velocities, explains the major features in rampart ejecta morphologies. We note that

Barlow et al. [2000] identify type examples for each feature.

We consider the progression from strong, dry craters to fully fluidized, multiple-layer rampart craters under similar impact conditions (silicate projectiles in the absence of abundant melting of the surface rock). Cratering onto a surface stronger than the mean effective yield strength on Mars (e.g., Y_{strong}) will result in smaller transient craters, $D_{Tr} \sim 8\ r_p$, compared to the average of about 11 r_p (Figure 3.4). In the stronger material, the near rim ejection angles are shallower and the ejection velocities are higher compared to average strength targets (Figure 3.11). Thus the ejection range is farther and the ejecta is spread more thinly. In progressively weaker materials, the transient cavity is larger, the ejection angles higher, and the ejection velocities lower. Thus, the ejection range is smaller and the flow velocities slower, depositing proportionally more mass near the crater rim.

When interstitial ice is present, where the bulk mass is still rock, the cratering process is essentially identical to a pure rock of equivalent strength. The impact shock will melt any ice in the transient crater cavity. Relatively large quantities of ice, e.g., $20\%_{vol}$, mixed with the rock on scales less than the projectile size, may decrease the shock pressures in the transient cavity by a factor of few (Figure 3.3). The crater shape is largely controlled by the effective strength of the target, which should be correlated with ice content.

Pancake Ejecta

The single-layer pancake ejecta morphology is characterized by a single concave lobate deposit, as shown in Figure 3.19A. In an analysis of 1558 craters, *Mouginis-Mark* [1979] found that the 226 craters with pancake ejecta morphology are preferentially found at high latitudes, poleward of 40°, and correlated with permafrost and channel materials. This morphology is restricted to small craters, $D < 8$ km, where 95.6% are smaller than 5 km in diameter [*Mouginis-Mark*, 1979]. We note that *Barlow and Bradley* [1990] did not find a latitude or terrain correlation with only 17 craters classified with pancake morphology. As seen in Figure 3.14, small strength-dominated craters have systematically less shock-melted ice emplaced in the near-rim ejecta blanket compared to larger craters (Figure 3.15). In this category, the ejecta blanket would contain a liquid water content of less than half the bulk ice content of the subsurface. In addition, for lower initial temperatures than the global mean ($T < 200$ K), the shock pressure required to melt ice will be slightly higher (c.f. Chapter 2), decreasing the amount of melt production.

Pancake craters are correlated with terrain which is inferred to be weaker than average,

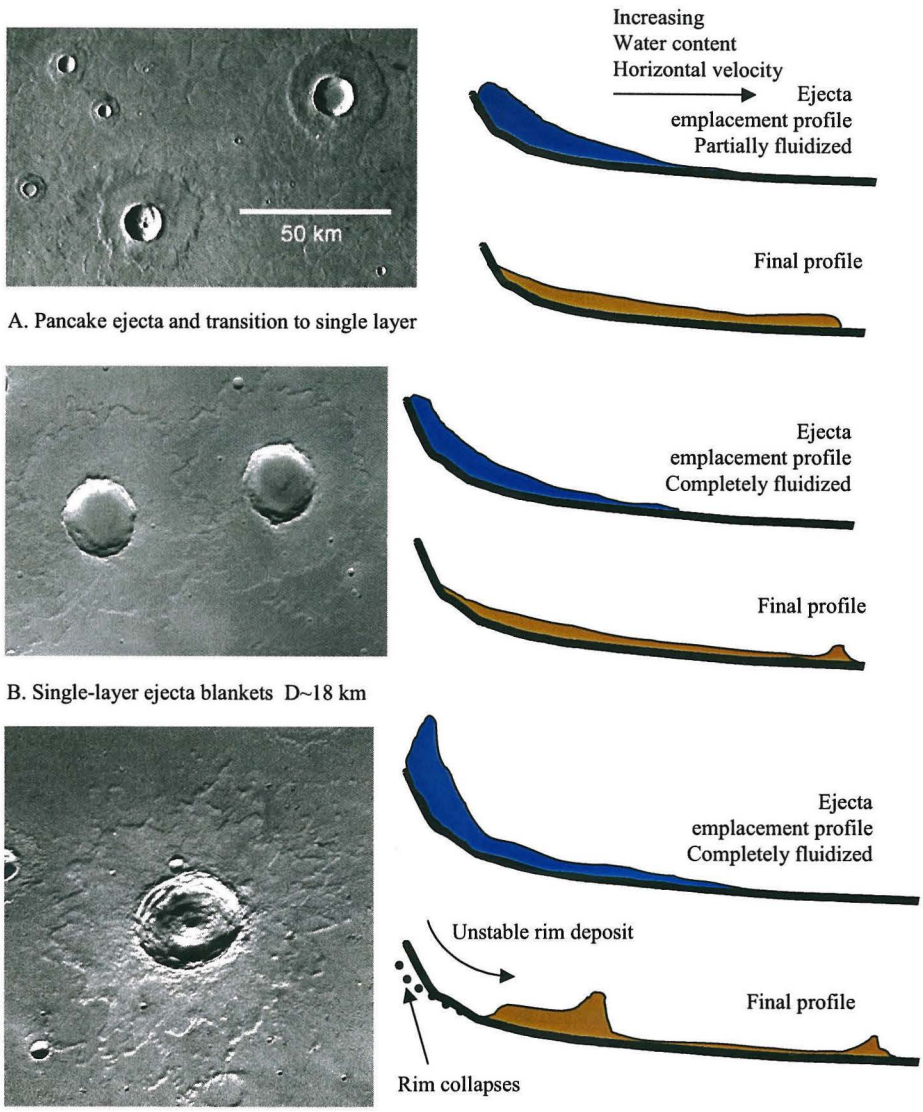

Figure 3.19: Schematic of formation models for rampart ejecta morphologies. Images from Viking orbiter mission: A-538A03, B-858A56, C-827A01.

e.g., in permafrost. Therefore, the excavation flow should have high ejection angles ($\geq 55°$) and relatively slow ejection velocities, depositing the ejected material closer to the crater rim. The horizontal flow velocities are in the range of large terrestrial landslides which may flow up to several km in distance starting with peak horizontal velocities in the range 10-100 m s^{-1} [*Shaller*, 1991]. Hence, pancake ejecta may be interpreted as partially fluidized flow associated with weaker target material around small craters where small amounts of melt are incorporated into the continuous ejecta blanket. The near-rim concentration of ejected material produces a thicker continuous ejecta blanket compared to dry craters, and the partial fluidization and low flow velocities of the material produces ground-hugging debris flow conditions. The concave terminus of the ejecta blanket implies that the amount of liquid contained in pancake ejecta morphologies is less than the single-layer ejecta with distal ramparts. Ground ice content may be inferred by the shock melting model presented here and debris flow modeling constraining the liquid water content to amounts which do not produce rampart features.

Single-layer Ejecta

Single-layer rampart ejecta blankets are characterized by a single continuous, convex distal scarp, shown in Figure 3.19B. Single-layer ejecta are found around systematically larger craters, but generally with $D < 20$ km, compared to pancake ejecta [*Mouginis-Mark*, 1979; *Barlow and Bradley*, 1990]. These craters are found on varied terrains at all latitudes, although there appears to be an onset diameter dependence with latitude [*Kuz'min et al.*, 1988b, a]. For craters with $D > 5$ km, more than half the H_2O in the ejecta blanket is melted from the impact shock (Figure 3.14), and the flow velocities are in the range of large terrestrial landslides.

Ivanov [1996] modeled the ejecta blanket flow as a Bingham fluid and found that rampart features may form for rheologies between highly fluidized dry flows and water-saturated flows. Ivanov found that the ejecta flow properties could match the runout distances observed in rampart ejecta for Bingham viscosities in the range $\nu_B = 0.5 - 30$ m^2 s^{-1} and Bingham yield stresses of $\tau_B/\rho = 2 - 50$ m^2 s^{-2} [see *Ivanov*, 1996, Figure 6]. On Earth, most water-saturated debris flows have $0.01 < \nu_B < 0.3$ m^2 s^{-1} and corresponding liquid water volume fraction in the range $30 - 60\%_{vol}$ (.15-.25 mass fraction) [e.g., *Whipple and Dunne*, 1992; *Major and Pierson*, 1992; *Phillips and Davies*, 1991]. Extrapolating between dry flows and water-saturated debris flows implies a volume fraction of liquid water in the

flowing ejecta blanket of about 10-30%$_{vol}$, corresponding to a subsurface ice content within a factor of 2 larger.

Therefore, single-layer rampart ejecta may be interpreted as a flow fluidized by liquid water, with an estimated concentration of 10-30%$_{vol}$. Since rampart ejecta features are found on all terrains, ground ice is probably pervasive on Mars. The correlation between the depth of excavation h_{exc} corresponding to the onset diameter of rampart features ($h_{exc} \sim D$) with the depth of ground ice stability as a function of latitude is an excellent confirmation of the model of entrainment of shock-melted ice in the ejecta blanket [*Kuz'min et al.*, 1988b, a]. Ground ice content may be inferred by the shock melting model presented here and debris flow modeling constraining the liquid water content to amounts which produce rampart features at the observed flow distances [e.g., *Ivanov*, 1996].

Double and Multiple-layer Ejecta

Previous work on double- and multiple-layer rampart ejecta, Figure 3.19C, have had different interpretations of the order of emplacement of each layer, consisting basically of either (a) superposition of the inner, thicker layer over the outer, thinner layer or (b) emplacement of the outer layer over the inner layer. These crater morphologies are found around systematically larger craters, up to about $D = 60$ km, but generally $D < 30$ km [*Barlow and Bradley*, 1990]. The MOLA topography of double and multiple-layer ejecta show that the inner layer is considerably thicker, 10's-100 m thick (Figures 3.17, 3.18), than the outer layers which the MOLA data indicate have negligible thickness over the surrounding terrain except for the terminating rampart. *Garvin and Frawley* [1998] found that rampart ejecta features have apparent volumes greater than 1.25 the estimated excavated cavity, based on the Z model with $Z = 3$. One of the most perplexing questions has been the mechanism that emplaces such a large volume of material near the crater rim. An example of the topography of the 10-100 m thick inner ejecta layers is shown in Figure 3.17.

From the cratering simulations, we found that the presence of interstitial ice increases the rim uplift and the excavation angles are steeper, resulting in more mass emplaced just beyond the crater rim. For crater rims uplifted beyond a stable angle of repose ($\gtrsim 45°$), some of the rim and excavated material will likely yield and flow to the flatter surrounding terrain. Since volume of ejected material and the rim uplift both scale with transient crater diameter, an unstable angle of repose is more likely around larger craters.

We propose that the thick, inner layer(s) observed in double and multiple-layer mor-

phologies are a result of partial collapse and flow of the crater rim and near-rim ejecta. In the crater diameter range 10-30 km, any ice in the material ejected just over the rim is nearly completely melted and emplaced on a steep slope, encouraging flow to the flatter surrounding terrain. The volume of material in our standard excavation model is consistent with the MOLA observations, although larger volumes for a given crater size could be excavated in weaker materials. The material ejected just beyond the crater rim may begin to flow to the surrounding terrain before rim collapse (see Figure 3.13), thus some of the material that might normally collapse into the final crater cavity could flow onto the surrounding terrain. The thick, inner ejecta blanket region may flow in a manner similar to single layer long runout fluidized flows, although the velocities are considerably larger.

Maps of ejecta striations and flow around surrounding obstacles imply that the inner portion of the ejecta blanket was emplaced first, followed by the thinner outer ejecta [*Mouginis-Mark*, 1981]. The faster ballistic ejecta, from the inner region of the transient cavity, forms the thinner outer ejecta blanket. The material forming the outer ejecta blanket experiences higher shock pressures and are disrupted into smaller fragments. These ejecta would be more sensitive to atmospheric drag than the larger fragments emplaced in the inner ejecta blanket. The outer ejecta blanket material may partially flow over the interior ejecta blanket deposit, as a result of atmospheric drag effects reducing the ballistic range and/or fast ground-hugging flow of the interior deposit reaching the range of the outer ejecta blanket material before the time of emplacement. The thin, outer ejecta blanket would be completely fluidized with large horizontal flow velocities at the time of emplacement (Figure 3.15), encouraging development of a long runout flow, forming the thin outer ejecta layers terminated by ramparts, extending to as much as $6R_F$.

We find that double and multiple-layered ejecta are not consistent with an abrupt change in the middle of excavation in the transient cavity, as suggested by *Mouginis-Mark* [1981], from penetration through layers with different ice content in the Martian crust. The streamlines of the excavation flow average over any near-surface layers with different composition. In addition, the mechanics of crater excavation cannot produce an inner ballistic ejecta deposit which flows over a thinner outer ballistic ejecta deposit at a later time. The material in the ejecta blanket layers must be emplaced from the crater rim on outward. The details of the post-emplacement flow, however, should be investigated to determine the timing of the ejecta emplacement, transient crater collapse, and possible yielding and flow of uplifted

rim material. Multiple-layered ejecta blankets often have an inner layer very close to the crater rim, indicating that rim collapse may be related to formation of layered features. The details of rampart ejecta layer formation must be investigated with a combined crater collapse and debris flow model to constrain ground ice content.

Because of the efficiency of shock-induced melting of ice, the presence of pre-existing liquid water in the Martian crust is not required for multiple layered features as suggested by *Barlow and Bradley* [1990]. Therefore, at this time, we cannot discern the presence of subsurface liquid water vs. solid ice from rampart ejecta morphologies, although investigations of interior morphologies should be pursued. We stress, however, that rampart crater morphologies are found on all but the youngest volcanic terrain, and most near-surface H_2O should be in the solid phase in the present climate, implying that shock-melting of subsurface ice is the dominant formation mechanism of rampart features.

Diverse Ejecta

As the crater size increases, the ejection velocities become much faster than the range of terrestrial landslides and debris flows. Rather than by lack of water content, the formation of rampart features around very large craters (> 30 km) is probably inhibited by the ejection velocities, which may not allow development of a cohesive debris flow (see Figure 3.15). If the ice content in the crust decreases rapidly with depth, perhaps concentrated in thin, near-surface layers, the vertical distribution of ice may be inferred by comparing the ejecta morphologies around craters over a range of sizes within a given geographic region. Future work will examine the relative effects of excavation depth and flow velocities in the transition to diverse ejecta blankets.

Current limitations and future work

Our model for formation of rampart ejecta morphologies is the first physical model that relates the major ejecta features to the excavation process. We have made the first quantitative estimates on the amount of interstitial ice which may be melted in an impact, showing that significant amounts of melt may be incorporated into the ejecta blanket. Future investigation of the double and multiple layer morphologies should focus on the effects of strength, with a model coupled to ice content and open porosity, on the final crater shape and collapse of the transient rim, including the timing of ejecta emplacement and complex crater rim collapse. There remain many intriguing secondary features to be examined more closely within the framework of this model, including radial straiations,

rampart sinuosity, and the transition to diverse ejecta blankets around the largest craters.

Impact-generated atmospheric ring vortices [*Barnouin-Jha and Schultz*, 1996] or viscous gravity currents [*Baratoux et al.*, 2001; *Baratoux*, 2001] are two proposed physical models for the formation of sinuous ramparts. While the near crater rim deposits are undoubtedly related directly to excavation and crater collapse processes, the outer ejecta deposits are expected to be influenced by the Martian atmosphere. The role of atmospheric drag in forming the sinuosity, and possibly the ramparts, should be reconsidered including the effects of the water vapor plume, the temperature and spatial distribution of liquid water and flow velocities in the modeled ejecta blanket. Also, impacts into an ice-rock mixture produces an H_2O vapor plume. Completely shock-vaporized (CV) ice is restricted to a zone of radius about 1 r_p (Figure 3.3), and its interaction with the projectile-disturbed atmosphere should be considered in future work to address the atmospheric drag effects on the fine ejecta.

The effect of variations in impact velocity should also be included in future analyses, as the final crater size scales with impact energy but the shock pressure decay profile is more sensitive to the projectile size. Higher impact velocities, found on the other terrestrial planets and satellites in the outer solar system ($\geq$ 20km s^{-1}), produce larger peak impact shock pressures, but also steeper pressure-decay curves related to shock-induced vaporization and melting [refer to *Pierazzo et al.*, 1997]. There should be an optimal projectile size-impact velocity range for the most efficient shock melting and excavation of subsurface ice.

3.6.2 Implications for the H_2O Budget on Mars

Using our crater excavation model, we calculate the average volume fraction of melted ice as a function of crater size for typical impact conditions on Mars. Thus, we may place a first-order estimate on the crustal ice content assuming an average critical liquid water fraction required for fluidized flow. Ivanov's study suggests a conservative liquid water volume fraction of about $20\%_{vol}$, corresponding to a near-surface ice volume fraction of about $\phi_0 = 20 - 40\%_{vol}$. Using the *Barlow and Bradley* [1990] rampart crater database, we may estimate the cumulative amount of H_2O in the ejecta blankets of observed rampart ejecta at the time of emplacement. The amount of water required for each crater size is, to first order, the volume of the excavated zone times the ice fraction, ϕ_0. The number density of rampart craters is shown in Figure 3.20A, from the compilation by *Barlow and Bradley*

[1990]. The large crater ($D > 8$ km) number distribution suggests a mean population age of about 3 Ga. The 1 Ga crater production function, for the rampart crater size range, is given by

$$\log N_{\text{Mars,1 Ga}}(\text{craters/km}^2) = -1.80 \log D_{\text{km}} - 3.28, \tag{3.17}$$

where the production function is assumed to scale linearly with time back to 3 Ga [see *Hartmann*, 1999]. The smallest craters in the database, solid line in Figure 3.20A, fall below the production function because of the difficulty in identifying small craters with the km-scale image resolution of the Viking dataset. Therefore, we use the size distribution along the 3 Ga isochron to estimate the total number of rampart craters with $D < 8$ km (dashed lines), which assumes that there is no size dependence in the fraction of all craters showing rampart features.

From the EDOZ excavation model and transient cavity scaling law (Eq. 3.3), we calculate the excavated volume as a function of crater diameter, shown in Figure 3.20B. The excavated volume V_E is well described by the power law (dotted line),

$$\log V_E = \begin{cases} -1.79 \log D_F + 3.24 & \text{if } D_F < 8 \text{ km} \\ -1.22 \log D_F + 2.59 & \text{if } D_F > 8 \text{ km} \end{cases} \tag{3.18}$$

In section 3.5, we showed that the volume of H_2O melt in the ejecta blanket is within a factor of 2 of the near-surface ice content ϕ_0. Assuming $\phi_0 = 0.2$ after Ivanov's work, we use the 3 Ga production function and the excavation volumes to estimate the cumulative volume of H_2O implied by the observed number of rampart craters, given by $NV_E\phi_0$, shown in Figure 3.20C, where the corresponding equivalent thickness of a global layer of water is given on the right vertical axis. The largest craters sample the largest volume of H_2O; therefore, for this calculation, errors in the number of small craters are negligible. Although we are most confident in the number of observable large rampart craters, it is likely that some of the rampart ejecta in this size range have been eroded.

Summing over the entire size range from $D = 1-32$ km, the volume of ice implied by the observed Martian rampart crater number distribution and $\phi = 0.2$ is equivalent to a global layer of water about 0.6 m deep. This value corresponds to the amount of ice excavated by impact craters over about 3 Ga. Since rampart craters stochastically sample a fraction of the surface, limited to excavation depths within the upper 2 km for the observed size range,

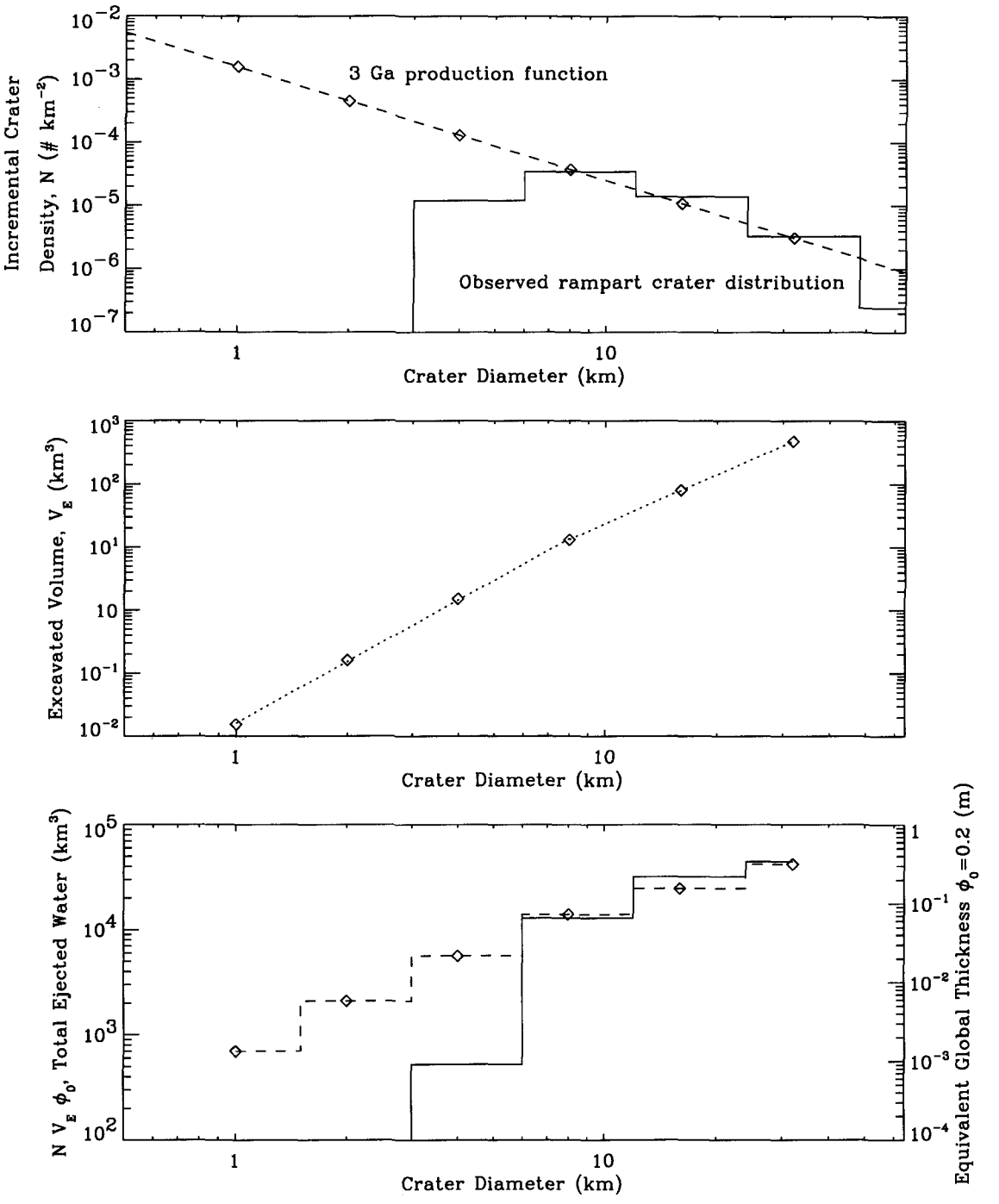

Figure 3.20: Inferred crustal water content from rampart crater database. **A.** Rampart crater number distribution [solid line, *Barlow and Bradley*, 1990] and 3 Ga crater production function [*Hartmann*, 1999]. **B.** Excavated volume as a function of final crater diameter. **C.** Volume of water in ejecta blankets in observed craters (solid lines) and inferred from crater production function (dashed line) for ice content $\phi_0 = 0.2$.

the actual regolith ice content must be considerably larger.

Only 0.5% of the Martian surface area was sampled by the observed rampart craters (cumulative area of the transient crater cavities). Correcting for the sampling area, the implied total ice content, within 2 km of the surface, is equivalent to a global layer of water about 120 m thick. Not all craters are rampart craters, however, implying a heterogeneous distribution of subsurface ice and less total ice content. From the Viking database, about 20% [*Barlow and Bradley*, 1990] of the craters with $D > 8$ km have rampart ejecta. Thus, the global ice content may be a factor of 5 smaller. A new crater database (in progress), derived from the MOLA topography dataset, implies that the fraction of rampart craters is larger than inferred from the Viking images, especially in the northern plains (M. Zuber, pers. comm.). Future work will include an analysis of the spatial distribution of ground ice with the MOLA dataset.

The implied 120 m global layer reservoir, although an order of magnitude estimate, is the first independent estimate of regolith water budget from rampart craters. For comparison, estimates of the amounts of water discharged in the catastrophic outflow channels is greater than a global layer 40 m thick [*Carr*, 1996]. The crustal water content estimate may be improved with the new MOLA crater database and stronger constraints on the actual liquid water content implied by rampart ejecta flow features. The value of $\phi_0 = 0.2$ used here could easily vary by a factor of 2.

Because rampart ejecta features may form by entrainment of liquid water, derived from shock-induced melting of subsurface ice, rampart craters do not imply a significantly different climate than exists today on Mars. Liquid water may remain metastable over the several-minute time scales of crater formation and ejecta emplacement [*Hecht*, 2000]. Craters are found on all but the youngest volcanic terrain, implying subsurface ice presence over all time on Mars. The total crustal ice content could be larger than implied here because the ejecta properties are only sensitive to the crustal ice content near the surface, within about 2 km for the observed rampart crater size range. Mapping the rampart ejecta morphologies on different age units to study the time-variability of ice content would be a useful constraint on the history of the Martian climate.

3.7 Conclusions

1. We have presented the first simulations of impacts into an ice-rich regolith which explicitly accounts for the equations of state and criteria for melting both the rock and ice components. We find that the shock wave from typical impact conditions (V_i = 10 km s^{-1}) on Mars partially melts subsurface ice in a zone up to about 15 R_p, larger than most final crater cavities, and completely melts ice within about 5 R_p. We have developed a model which relates the major rampart morphologies to the crater formation and excavation process. Pre-existing liquid water is not necessary for rampart ejecta blanket features.

2. The center of the ejection flow field is below the impact surface producing higher ejection angles near the impact point, decreasing slightly toward the crater rim. Standard Maxwell Z-models have difficulty reproducing both the depth of excavation and ejection angles. A truncated EDOZ model may be used to approximate the ejection angles and volume of ejecta by centering the flow at the depth of the isobaric core of the shock wave and ejecting materials above a standard Z=3 streamtube.

3. Weaker target materials have deeper transient craters, higher ejection angles near the crater rim and larger excavated zones. The higher angle of motion produces larger rim uplift. The magnitude of these effects is very sensitive to the strength model. Because the ejection angles are steeper, the volume of the continuous ejecta blanket is larger and the horizontal velocity of the flow at the time of emplacement is lower in weaker materials.

4. For the mean effective yield strength of the Martian surface (Y_{eff} = 10 MPa), most ice within the excavated zone is melted over the size range of observed rampart craters (most $D \leq 30$ km). The largest contribution of melt in the continuous ejecta blanket is from the partially melted zone. In the ejecta blanket, the fraction of melted ice increases away from the crater rim, where completely melted ice is ballistically ejected to distances of 34-0.5 R_F for 2.5-20 km diameter craters, respectively. Small craters will be a more sensitive measure of near surface ice content.

5. The volume and radial distribution of ejecta is consistent with MOLA observations of rampart craters for simulations with a simple Mohr-Coulomb target strength model

with $Y_{\text{eff}} = 10$ MPa and $20\%_{\text{vol}}$ ice. More realistic strength models coupled with a debris flow model are required to place finer constraints on the quantity of ground ice and correlate ice content with different ejecta morphologies.

6. For typical impacts at 10 km s^{-1}, the amount of liquid water in the ejecta blanket is representative of the near-surface H_2O content in the crust, within a factor of 2. Previous work suggests that the post-emplacement flow of rampart ejecta have water content between highly fluidized dry flows and water-saturated debris flows, implying ejecta blanket water contents in the range $10\text{-}30\%_{\text{vol}}$ [*Ivanov*, 1996], corresponding to a near-surface ice content of about $20\text{-}40\%_{\text{vol}}$. Based on the Viking rampart crater database and the impact production rate, the implied near-surface regolith H_2O content is equivalent to a global water layer of order 100 m deep.

3.8 Acknowledgements

We thank M. Lainhart, S. Byrne and A. Ivanov for their assistance. This work was supported under NASA grants NAG5-8915 and NAG5-10208. Contribution #8847 Division of Geological and Planetary Sciences, California Institute of Technology.

Bibliography

Ahrens, T. J., and M. L. Johnson, Shock wave data for rocks, in *Rock Physics and Phase Relations*, edited by T. J. Ahrens, no. 3 in A Handbook of Physical Constants, pp. 35–44, American Geophysical Union, 1995.

Ahrens, T. J., and J. D. O'Keefe, Shock melting and vaporization of lunar rocks and minerals, *Moon*, *4*, 214–249, 1972.

Ahrens, T. J., and J. D. O'Keefe, Shock vaporization and the accretion of the icy satellites of Jupiter and Saturn, in *Ices in the Solar System*, edited by J. Klinger, D. Benest, A. Dollfus, and R. Smoluchowski, NATO ASI Series, pp. 631–654, D. Reidel, Nice, France, 1985.

Ahrens, T. J., and J. D. O'Keefe, Impact on the Earth, ocean and atmosphere, *Int. J. Impact Engng.*, *5*, 13–32, 1987.

Baratoux, D., High-resolution Martian topography and dynamics of lobate craters: Inferences on the distribution of water on Mars, Ph.D. thesis, Laboratoire des Sciences de la Terre, Lyon, France, 2001.

Baratoux, D., C. Delacourt, and P. Allemand, Rheology of megaregolith from wave-length of Martian lobate ejecta deposits, in *Lunar Planet. Sci.*, vol. XXXII, Lunar and Planetary Institute, Houston (CD-ROM), 2001, abstract #1312.

Barlow, N. G., and T. L. Bradley, Martian impact craters: Correlations of the ejecta and interior morphologies with diameter, attitude, and terrain, *Icarus*, *87*, 156–179, 1990.

Barlow, N. G., J. M. Boyce, F. M. Costard, R. A. Craddock, J. B. Garvin, S. Sakimoto, R. O. Kuzmin, D. J. Roddy, and L. A. Soderblom, Standardizing the nomenclature of Martian impact crater ejecta morphologies, *J. Geophys. Res.*, *105*, 26,733–26,738, 2000.

Barnouin-Jha, O., and P. Schultz, Ejecta entrainment by impact-generated ring vortices: Theory and experiments, *J. Geophys. Res.*, *101*, 21,099–21,115, 1996.

Barnouin-Jha, O., and P. Schultz, Lobateness of impact ejecta deposits from atmospheric interactions, *J. Geophys. Res.*, *103*, 25,739–25,756, 1998.

Barnouin-Jha, O., P. Schultz, and J. Lever, Investigating the interactions between an atmosphere and an ejecta curtain 1. Wind tunnel tests, *J. Geophys. Res.*, *104*, 27,105–27,115, 1999.

Boyce, J. M., and D. J. Roddy, Martian crater ejecta, emplacement and implications for water in the subsurface, in *Proc. Lunar Planet. Sci. Conf.*, vol. 28, pp. 145–146, Houston, TX, 1997.

Boyce, J. M., D. J. Roddy, and R. Craddock, The origin of Martian fluidized ejecta: The requirement for water in the subsurface, in *Bulletin of the American Astronomical Society*, vol. 28, p. 1059, 1996.

Carr, M. H., *Water on Mars*, Oxford UP, 1996.

Carr, M. H., L. S. Crumpler, J. A. Cutts, R. Greeley, J. E. Guest, and H. Masursky, Martian impact craters and emplacement of the ejecta by surface flow, *J. Geophys. Res.*, *82*, 4055–4065, 1977.

Christensen, P., J. Bandfield, M. Smith, V. Hamilton, and R. Clark, Identification of a basaltic component on the Martian surface from Thermal Emission Spectrometer data, *J. Geophys. Res.*, *105*, 9609–9621, 2000.

Clifford, S. M., A model for the hydrologic and climatic behavior of water on Mars, *J. Geophys. Res.*, *98*, 10,973–11,016, 1993.

Croft, S. K., Cratering flow fields: Implications for the excavation and transient expansion stages of crater formation, in *Proc. 11th Lunar Planet. Sci. Conf.*, pp. 2347–2378, Houston, TX, 1980.

Fanale, F., J. Salvail, A. Zent, and S. Postawko, Global distribution and migration of subsurface ice on Mars, *Icarus*, *67*, 1–18, 1986.

Fink, J. H., R. Greeley, and D. E. Gault, Impact cratering experiments in Bingham materials and the morphology of craters on Mars and Ganymede, in *Proc. Lunar Planet. Sci. Conf.*, vol. 12B, pp. 1649–1666, 1981.

Garvin, J., and J. Frawley, Geometric properties of Martian impact craters: Preliminary results from the Mars Orbiter Laser Altimeter, *Geophys. Res. Lett.*, *25*, 4405–4408, 1998.

Garvin, J., S. Sakimoto, J. Frawley, and C. Schnetzler, North polar region craterforms on Mars: Geometric characteristics from the Mars Orbiter Laser Altimeter, *Icarus*, *144*, 329–352, 2000.

Gault, D. E., and R. Greeley, Exploratory experiments of impact craters formed in viscous-liquid targets: Analogs for Martian rampart craters?, *Icarus*, *34*, 486–495, 1978.

Hartmann, W., Martian cratering VI: Crater count isochrons and evidence for recent volcanism from Mars Global Surveyor, *Meteoritics Planet. Sci.*, *34*, 167–177, 1999.

Hecht, M. H., Short-term stability of surface water on Mars, *Eos Trans. AGU*, *81*, Fall Meet. Suppl. Abstract P61B–03, 2000.

Holsapple, K. A., The sclaing of impact processes in planetary sciences, *Annual Review of Earth and Planetary Sciences*, *21*, 333–373, 1993.

Holsapple, K. A., and R. M. Schmidt, On the scaling of crater dimensions 2. impact processes, *J. Geophys. Res.*, *87*, 1849–1870, 1982.

Housen, K. R., R. M. Schmidt, and K. A. Holsapple, Crater ejecta scaling laws: Fundamental forms based on dimensional analysis, *J. Geophys. Res.*, *89*, 2485–2499, 1983.

Ivanov, B. A., Spread of ejecta from impact craters and the possibility of estimating the volatile content of the Martian crust, *Solar System Research*, *30*, 43–58, 1996.

Ivanov, B. A., and A. V. Pogoretsky, Bingham parameters for fluidized ejecta spreading on Mars and Martian volatiles, in *Proc. Lunar Planet. Sci. Conf.*, vol. 27, pp. 587–588, 1996.

Ivanov, B. A., A. V. Pogoretsky, and B. Murray, Fluidized ejecta blankets on Mars: Estimate of material properties, in *Proc. Lunar Planet. Sci. Conf.*, vol. 28, Abs. 1470, 1997.

Kieffer, H. H., B. M. Jakosky, C. W. Snyder, and M. S. Matthews (Eds.), *Mars*, U. Arizona Press, Tucson, 1992.

Kieffer, S. W., and C. H. Simonds, The role of volatiles and lithology in the impact cratering process, *Reviews of Geophysics and Space Physics*, *18*, 143–181, 1980.

Kuz'min, R. O., N. N. Bobina, E. V. Zabalueva, and V. P. Shashkina, The structure of the Martian cryolithosphere upper levels, in *Workshop on Mars Sample Return Science*, p. 108, LPI Technical Report 88-07, 1988b.

Kuz'min, R. O., N. N. Bobina, E. V. Zabalueva, and V. P. Shashkina, Structural inhomogeneities of the Martian cryolithosphere, *Solar System Research*, *22*, 121–133, 1988a, translated from Astronomicheskii Vestnik Vol. 22 No. 3 pp.195-212 1988.

Major, J., and T. Pierson, Debris flow rheology - experimental-analysis of fine-grained slurries, *Water Resources Research*, *28*, 841–857, 1992.

Maxwell, D. E., Simple Z model of cratering, ejection and the overturned flap, in *Impact and Explosion Cratering*, edited by D. J. Roddy, R. O. Pepin, and R. B. Merrill, pp. 983–1022, Pergamon, Elmsford, New York, 1977.

McGlaun, J. M., S. L. Thompson, and M. G. Elrick, CTH: A 3-dimensional shock-wave physics code, *Int. J. Impact Engng.*, *10*, 351–360, 1990.

Mellon, M., B. Jakosky, and S. Postawko, The persistence of equatorial ground ice on Mars, *J. Geophys. Res.*, *102*, 19,357–19,369, 1997.

Melosh, H. J., *Impact Cratering: A Geologic Process*, Oxford UP, 1989.

Melosh, H. J., and B. A. Ivanov, Impact crater collapse, *Annu. Rev. Earth Planet. Sci.*, *27*, 385–415, 1999.

Mouginis-Mark, P., Martian fluidized crater morphology: Variations with crater size, latitude, altitude, and target material, *J. Geophys. Res.*, *84*, 8011–8022, 1979.

Mouginis-Mark, P., Ejecta emplacement and modes of formation of Martian fluidized ejecta craters, *Icarus*, *45*, 60–76, 1981.

Mouginis-Mark, P. J., Morphology of Martian rampart craters, *Nature*, *272*, 691–694, 1978.

O'Keefe, J., and T. Ahrens, Complex craters: Relationship of stratigraphy and rings to impact conditions, *J. Geophys. Res.*, *104*, 27,091–27,104, 1999.

O'Keefe, J. D., and T. J. Ahrens, Planetary cratering mechanics, *J. Geophys. Res.*, *98*, 17,011–17,028, 1993.

O'Keefe, J. D., S. T. Stewart, M. E. Lainhart, and T. J. Ahrens, Damage and rock-volatile mixture effects on impact crater formation, *Int. J. Impact Engng.*, *in press*, 2001.

Phillips, C. J., and R. H. Davies, Determining rheological parameters of debris flow material, *Geomorphology*, *4*, 101–110, 1991.

Pierazzo, E., and H. Melosh, Melt production in oblique impacts, *Icarus*, *145*, 252–261, 2000.

Pierazzo, E., A. Vickery, and H. Melosh, A reevaluation of impact melt production, *Icarus*, *127*, 408–423, 1997.

Schmidt, R. M., and K. R. Housen, Some recent advances in the scaling of impact and explosion cratering, *Int. J. Impact Engng.*, *5*, 543–560, 1987.

Schultz, P., Atmospheric effects on ejecta emplacement, *J. Geophys. Res.*, *97*, 11,623–11,662, 1992.

Schultz, P. H., and D. E. Gault, Atmospheric effects on martian ejecta emplacement, *J. Geophys. Res.*, *84*, 7669–7687, 1979.

Shaller, P. J., Analysis and implications of large Martian and terrestial landslides, Ph.D. thesis, California Institute of Technology, Pasadena, CA, 1991.

Thompson, S. L., and H. S. Lauson, Improvements in the Chart D radiation-hydrodynamic CODE III: Revised analytic equations of state, *Tech. Rep. SC-RR-71 0714*, Sandia Lab-

oratories, Albuquerque, NM, 1972.

Tonks, W. B., E. Pierazzo, and H. J. Melosh, Impact-induced differentiation in icy bodies, 1997, submitted to Icarus.

Turtle, E. P., and E. Pierazzo, Thickness of a Europan ice shell from impact crater simulations, *Science*, *294*, 1326–1328, 2001.

Whipple, K., and T. Dunne, The influence of debris-flow rheology on fan morphology, Owens Valley, California, *Geological Society of America Bulletin*, *104*, 887–900, 1992.

Wohletz, K. H., and M. F. Sheridan, Martian rampart craters ejecta: Experiments and analysis of melt-water interaction, *Icarus*, *56*, 15–37, 1983.

Appendix A: Details of Shock-Wave Experiments in Ice

This appendix includes the calibrated particle velocity data traces from each impact experiment. The data records are presented for the time period up until the gauge breaks. Gauge locations are specified as distances from the front of the first ice disc in the target assembly. The primary error on the measurement of the gauge location is the measurement of the thickness of the ice discs and are estimated to be about 0.025 mm.

Thick targets (> 10 mm) are designed to measure the primary shock wave profile. Thin targets (≤ 10 mm) are designed to measure both the shock wave and release wave, reflected from the rear of the target. In this geometry, the release wave produces an increase in particle velocity.

All experiments have a 0.7 mm polycarbonate buffer disc at the front of the target, which preserved contact between the first gauge and the first ice disc. All shots used solid polycarbonate projectiles. The buffer disc thickness was comparable to the width of the shock front, and the particle velocity at the first ice disc was determined by the impedances of the polycarbonate and ice rather than a symmetric polycarbonate impact. This is confirmed with shots #1037 and #1038 (in preparation), with and without a polycarbonate buffer, where the same peak particle velocity was recorded in each experiment.

Experiments with impact velocities < 350 m s^{-1} (I44-I45) are compressed gas (He) shots. Experiments with higher impact velocities (#1043-1047) are driven by propellant (IMR4350). The uncertainties shown in the loading path figures are 1σ.

Shot #I44 - Solid Ice

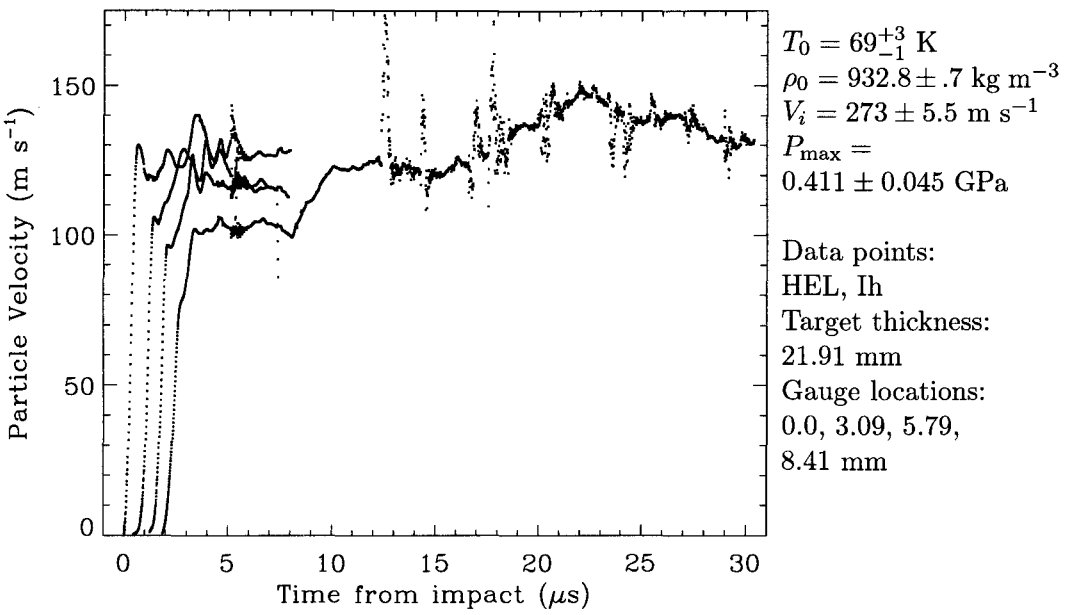

Figure A.1: Data record.

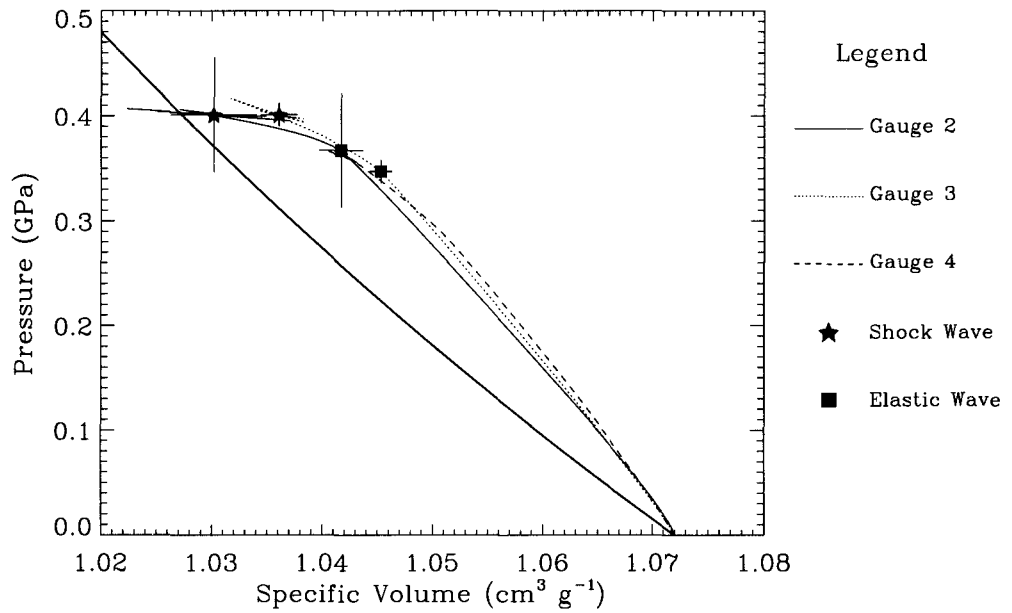

Figure A.2: Loading path.

Notes: Peak pressures just above HEL achieved. Propagating shock wave was not steady and decays to an elastic wave by arrival at 4th gauge. 4th gauge also displays a release profile which may be a combination of release from sides and rear of target. Velocity resolution of oscilloscope is ~ 1.7 m s^{-1}.

Shot #I45 - Solid Ice

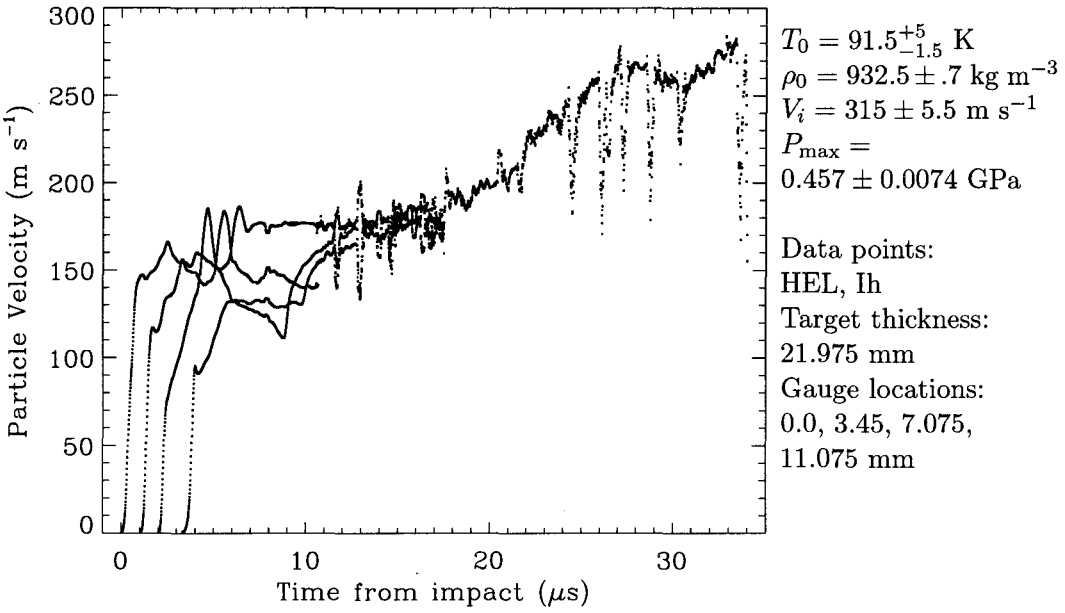

Figure A.3: Data record.

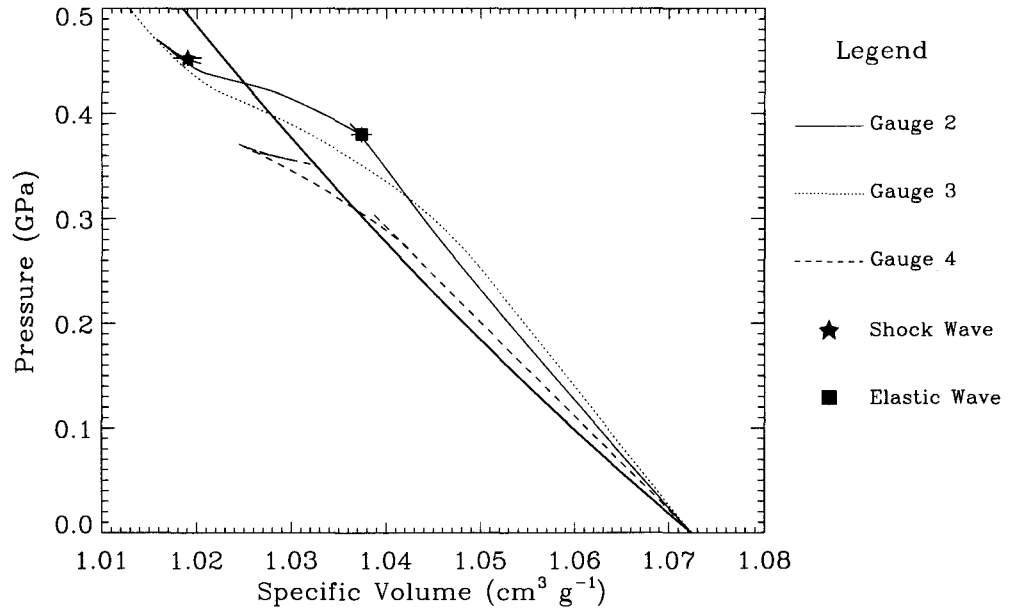

Figure A.4: Loading path.

Notes: Peak pressures just above HEL achieved. Final shock wave is not steady. There was a space between the 2nd and 3rd ice discs in the target assembly. Motion of the free surface between discs #2 and 3 produced a $\sim$ 30 m s^{-1} peak to peak oscillation of gauge 3. The space partially releases the shock wave, so the wave arrival at the 4th gauge has decayed to the Hugoniot Elastic Limit. The spike wave feature appears to reflect from the gap boundary back to the 2nd and 1st gauges, propagating at the sound speed in the shocked state. Only the shock propagation time from the 1st to 2nd gauge is used for Hugoniot data points. Release from the rear of the target is recorded in gauges 4 and 3. Velocity resolution of oscilloscope is about 1.3 m s^{-1}.

Shot #1046 - Solid Ice

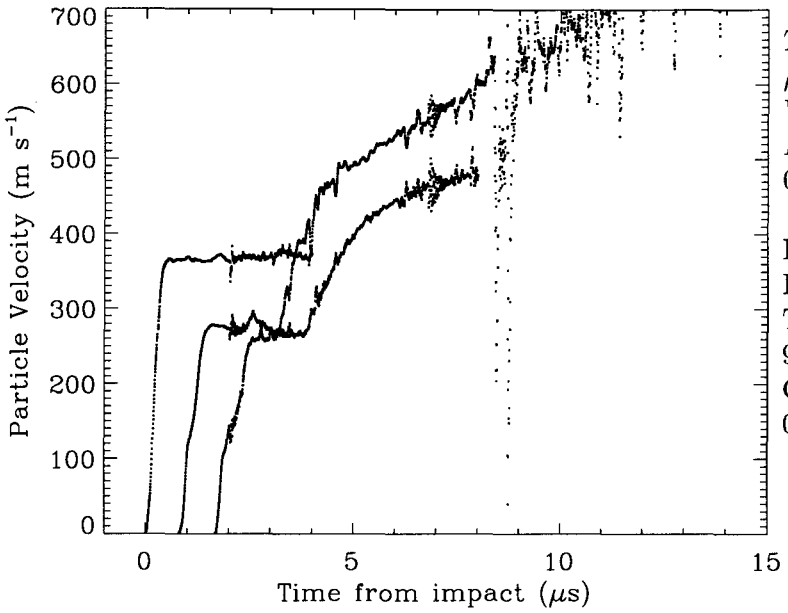

Figure A.5: Data record.

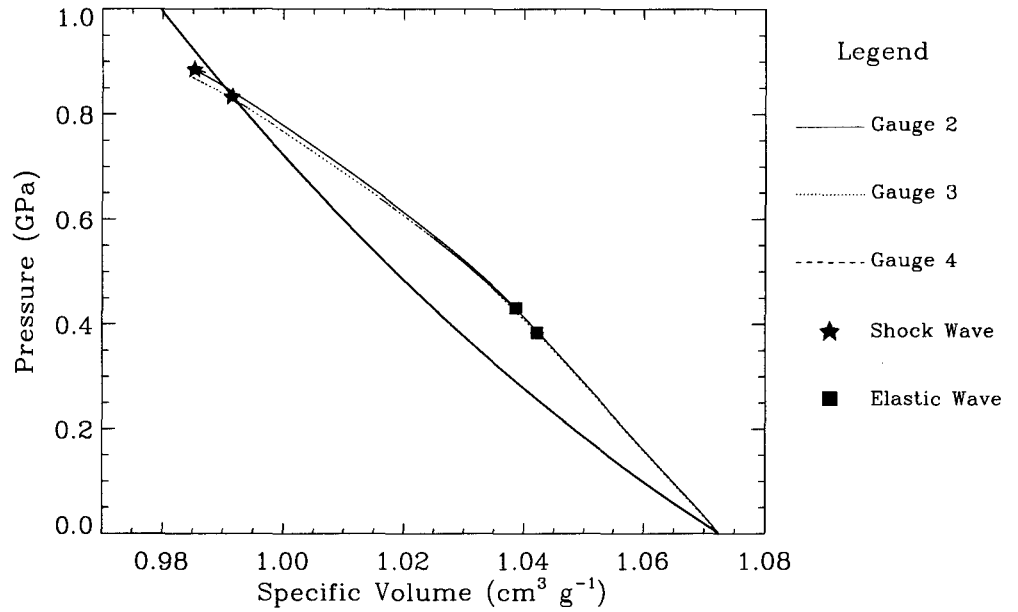

Figure A.6: Loading path.

Notes: This impact initiated a wave with peak pressures above the ice Ih shock pressure which propagates to gauges 2 and 3. But the wave velocity for a transformation to a higher pressure phase was too slow to propagate to the 2nd gauge during the time frame of the experiment. The release from the rear arrives before the transformation wave. Thus, only a HEL and Ih shock wave are detected in gauges 2 and 3 before release from the rear of the target. Ideal release curves are recorded in the 2nd and 3rd gauges. Velocity resolution of the oscilloscope is about 1.9 m s^{-1}.

Shot #1047 - Solid Ice

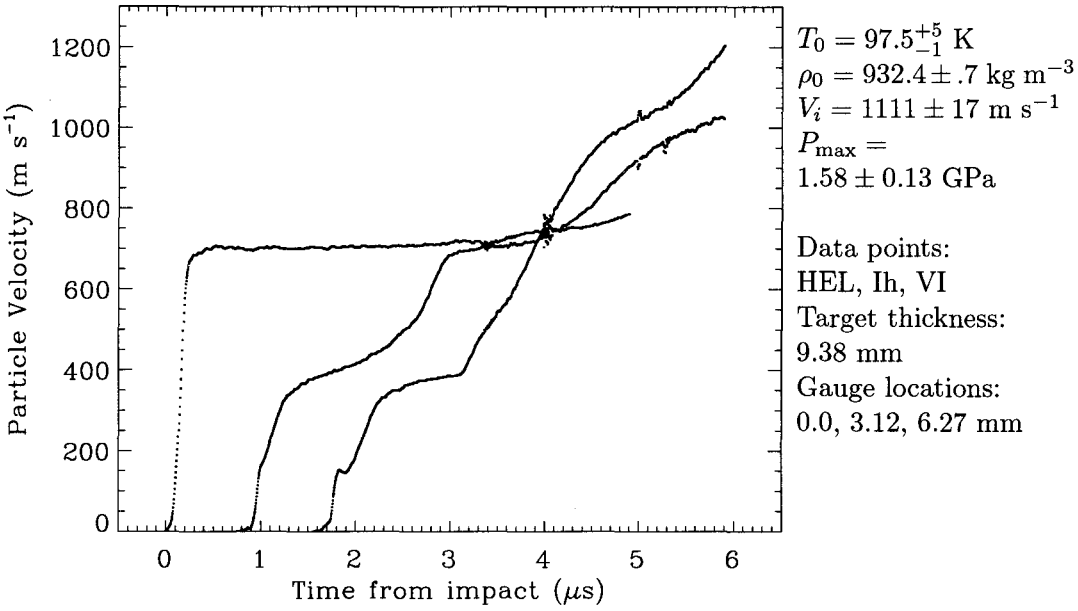

Figure A.7: Data record.

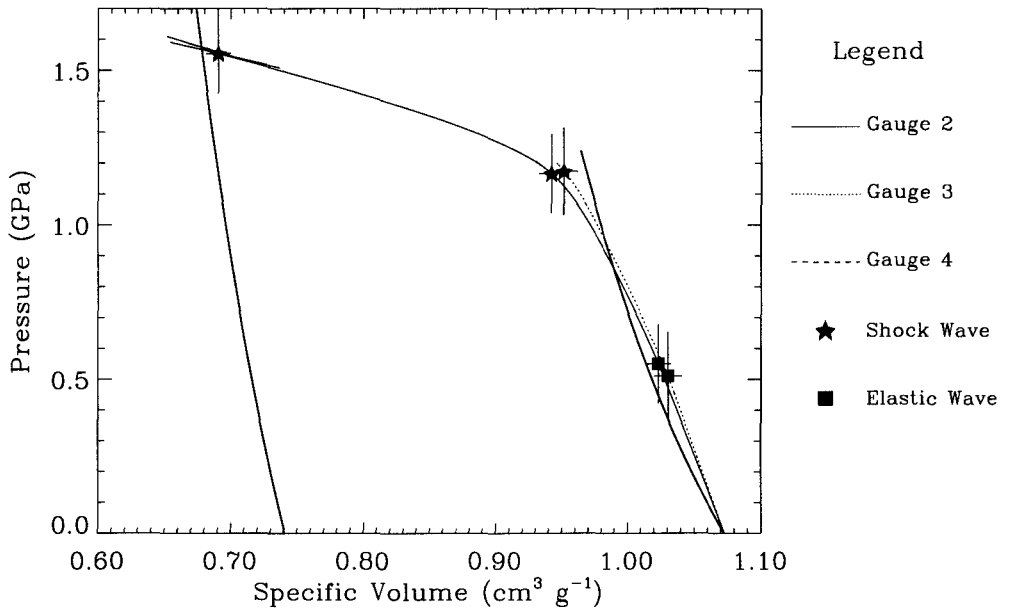

Figure A.8: Loading path.

Notes: This shot produced a transformation shock to the ice VI structure. The three-wave structure is clear in the 2nd gauge. The release wave from the rear of the target reaches gauge 3 before the ice VI transformation wave arrives. Velocity resolution of the oscilloscope is about 5.4 m s^{-1}.

Shot #1043 - Solid Ice

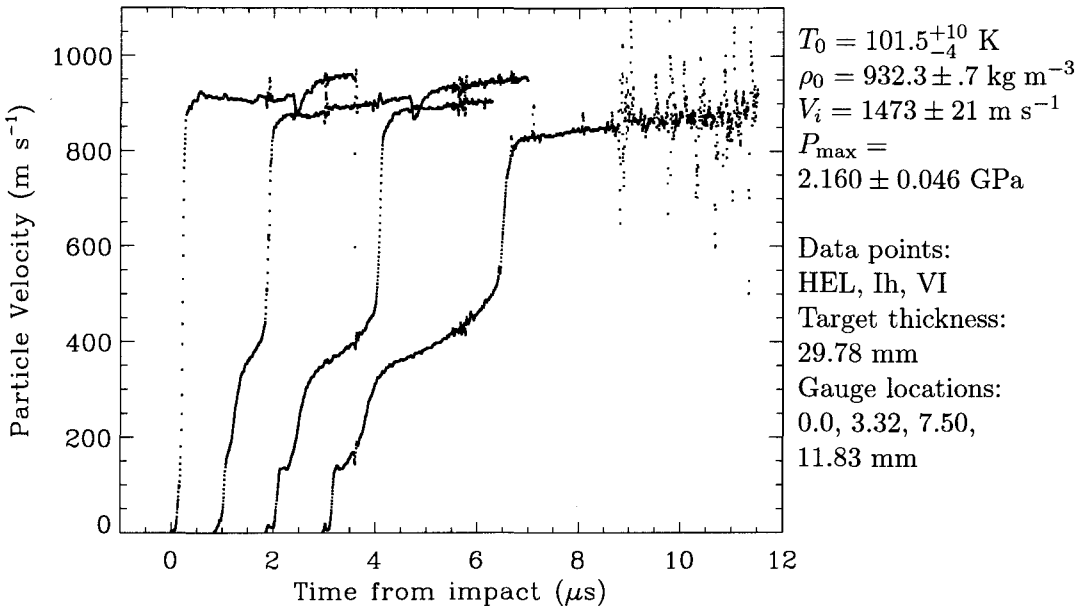

Figure A.9: Data record.

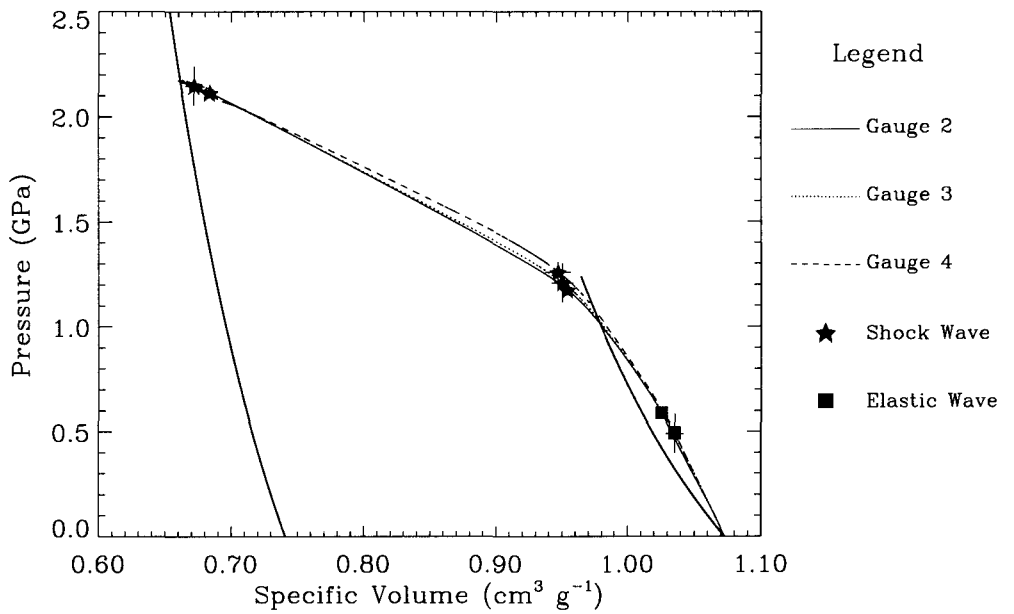

Figure A.10: Loading path.

Notes: This shot produced a transformation shock to the ice VI structure. The three-wave structure is clear in the 2nd gauge. The three-wave structure is clear in the 2nd , 3rd and 4th gauges. The wave has decayed a little by the arrival at the fourth gauge and this peak shock state is not part of the ice shock Hugoniot dataset. Velocity resolution of the oscilloscope is about 6.6 m s^{-1}.

Shot #1045 - Solid Ice

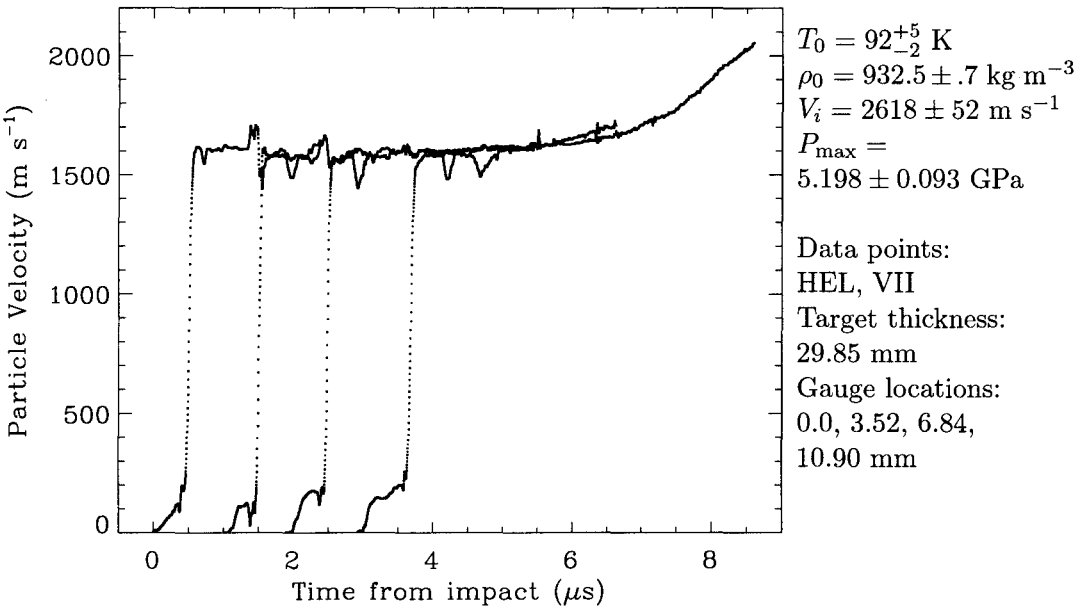

Figure A.11: Data record.

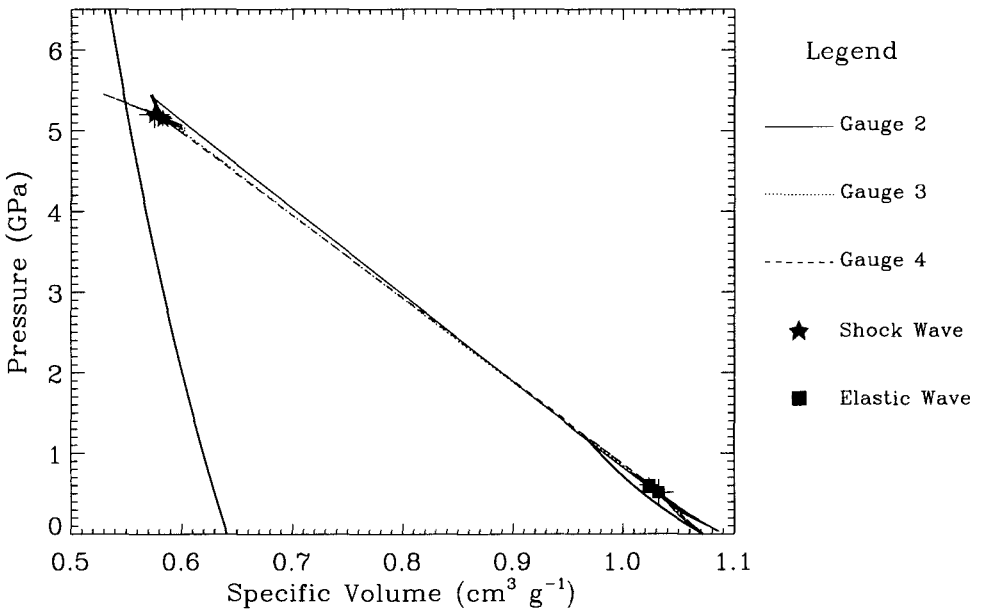

Figure A.12: Loading path.

Notes: This impact drove a transformation to the ice VII structure. The shock wave split into a two-wave structure: the HEL wave and ice VII transformation shock. The loading profile is close to the ideal shape: a straight line from the initial to the final P,V state. Since the ice VII transformation shock velocity (3.4-3.5 km s^{-1}) is nearly the HEL wave speed, stronger shocks will over drive the HEL. The knee in the 1st gauge implies that the impact was not perfectly normal to the target. This probably resulted in a slightly higher than ideal peak pressure, since the shock wave propagated on top of this initial wave arrival. The imperfect impact also influenced the shape of the HEL wave, but did not affect the wave speed calculations. Velocity resolution of oscilloscope is about 13.8 m s^{-1}.